SEARCHLIGHT CT: A NEW REGULARIZED RECONSTRUCTION METHOD FOR HIGHLY COLLIMATED X-RAY TOMOGRAPHY

A Dissertation

Presented to

the Faculty of the Department of Mathematics

University of Houston

In Partial Fulfillment

of the Requirements for the Degree

Doctor of Philosophy

By

Anando Sen

May 2012

SEARCHLIGHT CT: A NEW REGULARIZED RECONSTRUCTION METHOD FOR HIGHLY COLLIMATED X-RAY TOMOGRAPHY

Anando Sen

APPROVED:

Prof. Robert Azencott, Advisor

Dr. Demetrio Labate, Advisor

Dr. Bernhard Bodmann

Dr. Xiaobo Zhou

Dean, College of Natural Sciences and Mathematics

Acknowledgements

On a regular afternoon of the summer of 2008 I created a folder on my computer and named it 'summer project'. Today after almost four years the folder contains over 2000 files and forms the core of this thesis. This journey, though challenging at times, has been immensely enjoyable. There was no way I could have gone through this alone, so I'd like to thank several people who guided me through this.

Firstly I would like to thank my advisors Dr. Robert Azencott and Dr. Demetrio Labate, both of whom financially supported me during my graduate student life. As I entered this project Dr. Azencott took total charge and with a balanced combination of motivation, encouragement, and firmness made sure I was never out of my depth. His enormous experience in mathematics was crucial to the success of this project. Despite his busy schedule he was always ready for discussions and approachable for any problem I had. He gave me the freedom to work independently while at the same time kept track that I didn't lose focus. Dr. Labate joined our project in 2009 and with his expertise in electrical engineering gave it a new outlook. It was due to his efforts and patience that I was able to improve upon my fuzzy knowledge of wavelets. He provided us with several references which we weren't aware of, especially the work of Katsevich, which forms a major part of this thesis. He was very supportive when I hit a road block in the project.

My committee members Dr. Bernhard Bodmann and Dr. Xiaobo Zhou provided crucial suggestions during the project. Dr. Bodmann was the first person who introduced me to research at University of Houston. He was instrumental in getting

me into this project. During my first year as a graduate student, he was very helpful when I was struggling to get myself acquainted with Matlab. I have taken four courses with him which were very informative and added to my mathematical intellect. Dr. Zhou, along with Dr. King Li at the Methodist Hospital, were the ones to come up with this problem which went on to become my thesis. They supported this project with a two-year grant. Their experience with industrial situations was very useful. I hope to continue this collaboration with them in the future. All four of my committee members went through the thesis in great detail and made some very important suggestions.

Dr. Igor Patrikeev and Dr. Massoud Motamedi at University of Texas Medical Branch provided us a set of biological data and collaborated with us on a publication. Dr. Vijay Bhagia at Houston Orthodontics provided another set of biological data. Dr. Adam Wunderlich, whose Master's thesis I used extensively, was very kind to send me the latest version of his code for the implementation of the Katsevich inversion formula. Dr. Amir Averbuch at Tel Aviv University referred me to his paper on X-ray Transforms which was the underlying model for the problem.

I am eternally grateful to the University of Houston Mathematics Department for financial support during my Ph.D. It also gave me an opportunity to teach for the past five years. I would like to especially thank Dr. Jeff Morgan, Dr. Shanyu Ji, Dr. Matt O'Malley, and Ms. Pamela Draughn. During my years at the university I got to learn a lot from the faculty members in various courses and other interactions. Dr. Auchmuty, Dr. Nicol, Dr. Paulsen, Dr. Hausen, Dr. Gorb, and Dr. Papadakis were all very kind and informative during the time I interacted with them.

For a guy in his twenties a life without friends is not imaginable. My friends have always been a source of support, happiness, and of course, 'way too much of fun'. Being mathematicians we couldn't help being nerdy at times and had very interesting discussions as well. My batch-mates who started this graduate journey with me in India almost six years back deserve a special mention. Ankita Jain has been a reassuring presence and been there to listen to all my rants - good or bad. I have had several intellectual discussions with Natasha Shilla and she has been an inspiration with her exceptional work ethics. Pankaj Singh, my apartment mate with his superb grasp of analysis was always available whenever I needed any help in theoretical problems. With a calm head on her shoulders, Aanchal Aggarwal made sure that I always toed the line - academically and otherwise.

I had several friends and colleagues at the university who I'd like to acknowledge for their roles in my success - Aarti, Vasudha, Harbir, Akshay, Nandini, Negi, Kidist, Manisha, Ajit, Justin, Arjun, Angelynn, Joseph, Anushaya, Nick, Ricky, Chinmaya, Yao, Illija, Cheng, Filiz, Ananya, Satish, Yutheeka, Tassaduk, Mei, Becky, Rahul, and Mauricio. All of us being in the same position, we could associate very well with each other.

The opportunity to pursue a career in mathematics came to me through the Mathematical Sciences Foundation in New Delhi. For me it was especially important as at that time, I lacked the ability to excel in the examination system present in India. Dr. Dinesh Singh with his motivational words of wisdom challenged us to test the limits of academic excellence. Dr. Sanjeev Agrawal and Dr. Amber Habib through their innovative teaching techniques prepared us thoroughly for an academic

career.

It was at Sri Venkateswara College that I chose my specialization as mathematics. Mr. Pradeep Narain, whose coaching classes I attended, was instrumental in building up the required thought process in mathematics. Mr. K.C. Malik was the first teacher who saw research potential in me. My friends - Sumita, Hitesh, Gaurav, Charu, Pallavi, Prince, and Rohit made my time at college very memorable. I attended all fourteen years of my schooling at Sardar Patel Vidyalaya. I would like to especially mention Mr. Sanjay Sinha, who taught me mathematics for three years, Ms. Susheela Mohandas, to whom I attribute my programming skills and my friends Satyaki, Adarsh, and Abeer.

The role of a family is essential for the development of an individual. My family has always been there for me and taken a keen interest in my work. I wish all my grandparents had been with us today to witness the completion of my Ph.D. but I'm glad that at least my grandfather, Sanjit Sen is with us. He has always encouraged me to aim for the best and never give up. Though they are no more, my grandparents Uma Sen, Sabitry Sengupta, and Bimal Jyoti Sengupta guided me through my childhood as well as always keeping a close tab on my work.

My uncles and aunts Bhaskar Sengupta, June Hampson, Siddhartha Sen, and Chandan Sen have all been in close touch with me about work and other matters, offering very useful advice at important times. Being the only mathematician in the family, my uncle Bhaskar was the only one who was able to partly associate with my research, and I had several related discussions with him. I am glad to have timed the completion of my thesis in a way that it almost coincided with my cousin Gautam

Sen becoming a medical doctor. We grew up together and are now entering the next stages of our lives at the same time.

Last but certainly not the least, I would like to thank my parents and sister. My parents Sambudha Sen and Nivedita Sen took great care of my academics during my primary and middle school. In high school and college they gave me the freedom to choose my specialization even though it was totally different from theirs. They were supportive when I had to leave home to start graduate school and have followed each and every aspect of my life thoroughly. Courtesy of my sister Madhobi Sen, I discovered the joys of teaching mathematics. Being the elder brother I had a great time in sharing my experiences with her, when it was her turn to choose a specialization in college.

Despite my best efforts, it is impossible to thank everyone who has been involved in my academic success. I have attempted to make the list exhaustive but in case I have forgotten some one, it is not deliberate. Once again a very warm heartfelt thank you to everyone.

SEARCHLIGHT CT: A NEW REGULARIZED RECONSTRUCTION METHOD FOR HIGHLY COLLIMATED X-RAY TOMOGRAPHY

An Abstract of a Dissertation

Presented to

the Faculty of the Department of Mathematics

University of Houston

In Partial Fulfillment

of the Requirements for the Degree

Doctor of Philosophy

By

Anando Sen

May 2012

Abstract

This thesis introduces a new method for image reconstruction in collimated Computed Tomography called Searchlight CT. The method significantly reduces the overall radiation exposure when primarily the reconstruction of a specified region of interest is required. To achieve this, the Searchlight CT approach restricts the acquisition essentially to the region of interest, yet the algorithm provides a stable and robust reconstruction of the region of interest. The algorithm uses an iteration of the X-ray Transform and its regularized inverse.

The performance of the algorithm is illustrated on simulated phantoms as well as experimental data. It is tested initially on 2D data and studied in detail for the 3D case including the adaptation to spiral tomography. Various methods of regularization are explored with special a emphasis on wavelet-based non-linear regularization. Finally the sensitivity of the algorithm to noise is studied. Numerical results for all cases are provided.

The outline of an analytical proof for the convergence conditions is provided. The convergence is validated by the computation of the spectral radius of the iteration operator in various cases. A detailed analysis of the eigenvalues and eigenvectors leads to an apriori condition on convergence.

Contents

List of Figures

List of Tables

CHAPTER 1

Introduction

1.1 Background

Computed Tomography (CT) is a widely used medical imaging method which is employed to visualize interior organs within the human body and to obtain information on their structural properties. Starting with its introduction in the 1970s, CT has become an essential tool in medical diagnostic and preventive medicine, and its usage has increased very rapidly over the last decade due to technological advances which have made the procedure much more user-friendly to both patients and radiologists. Over 72 million CT scans were performed in the USA in 2007 [84]. In particular,

in recent years, the application of CT has been expanded rapidly due to the introduction of new imaging technology such as multi-detector scanners for applications such as angiography [36, 63]. However, the acceptance of new imaging instruments has been slow in past due to concerns about radiation safety and the dose that is needed [57, 39] to acquire CT images with high spatial resolution. Furthermore, in preclinical studies where high-resolution CT technique could be routinely used for longitudinal imaging of animal models, there is a great need for reducing radiation dose during imaging studies of tumors. Nevertheless, by its nature, CT involves the exposure of the patient to X-ray radiation and this is associated with health risks (in the form of radiation-induced carcinogens) which are essentially proportional to the levels of radiation exposure. Indeed, it is estimated that currently about 2% of cancers in the United States may be attributed to the radiation from CT examinations [10].

The method presented in this thesis aims to reduce the overall radiation exposure from CT when primarily the reconstruction of a specific region of interest within the human body or within an organ is required. This is the typical situation, for example, of patients undergoing regular CT screenings to monitor the progress of a tumor (when longitudinal studies with frequent scanning are needed). It is clear that, if the objective is to reconstruct only a "small" region of interest within a 3D object, it is possible in principle to dramatically reduce the radiation dose during a CT scan by using *collimated* X-ray projections, i.e., by limiting the irradiation mainly to the X-ray passing through the region of interest.

Indeed, in this thesis we show that it is possible to reconstruct a specific region

of interest in collimated three-dimensional X-ray tomography by employing a new reconstruction algorithm which ensures numerically stable and accurate reconstruction. The new algorithm, called Searchlight Computed Tomography, is based on an iterative procedure, which converges rapidly inside the region of interest and whose performance was validated on both synthetic and experimental data. The development of this new algorithm, which is able to maintain image quality while reducing incident dose of radiation, could have significant impact on the field of bio-medical imaging.

1.2 Framework

The objective of X-ray Tomography consists in converting a set of projection images of an object, usually obtained by measuring the attenuation of a certain radiation traveling along various directed paths, into a representation of the object structure. The X-ray Transform is the mathematical model used to establish a formal relationship between the observed data (i.e., the projection images) and the object under investigation. Specifically (in 3D), for a compactly supported Lebesgue-integrable function F on $\mathbb{R}^3$, its **X-ray Transform** XF is a function defined on the set of all straight lines l in $\mathbb{R}^3$. That is, for $w \in \mathbb{R}^3$ and $\theta \in S^2$ a unit vector, the X-ray Transform of F at (w, θ) is the line integral of F over the straight line $l(w, \theta)$, through w with direction θ.For a formal mathematical definition refer to Section 5.1

The objective of recovering F from the values of XF is formally achieved by inverting the X-ray Transform. The formula for the inversion of the X-ray Transform

is the so-called filtered back-projection which is an application of the Fourier Slice Theorem [3, 65]. Unfortunately, this is a classical **ill-posed problem**, in the sense the reconstructing F from the values of its X-ray Transform is numerically unstable.

The mathematical term 'well-posed problem' originates from a definition given by Jacques Hadamard [33]. He believed that mathematical models of physical phenomena should have the properties that

1. A solution exists
2. The solution is unique
3. The solution depends continuously on the data, in some reasonable topology.

A mathematical problem or model not satisfying these conditions is said to be 'ill-posed".

This numerical instability becomes even more challenging if one desires to recover F, or part of it, from an incomplete set of X-ray data [66]. Here, we are interested in a special instance of reconstruction from incomplete data where the goal is the reconstruction of a specific region of interest C of an unknown object F using mainly the X-rays passing through C. As expected, direct reconstruction attempts from collimated X-ray projections introduce many undesirable artifacts due to the ill-posedness of the inversion problem. To overcome this, that some form of regularized reconstruction is required. The regularized reconstruction method which is introduced based on an iterative procedure which is able to provide accurate reconstructions of the specific region of interest C mainly employing the collection of

X-rays collimated on C.

1.3 Outline of Thesis

The thesis is divided into thirteen chapters including the Introduction.

Chapter 2 introduces the 2D problem. The basic definitions and results are given for 2D. Data acquisition from parallel (cylindrical) beam and conical beam X-rays are discussed. The completion of X-ray data from a minimal number of projections is described. The concept of a collimated acquisition is defined and the causes for its non locality are outlined. We describe the algorithm for reconstruction of a region of interest from collimated projections.

In **Chapter 3** we give an outline to the analytical proof for the convergence of our algorithm. An apriori condition on the spectral radius which ascertains whether convergence is possible or not. A detailed validation through eigenvalues and eigenvectors is carried out (in 2D) using the spectral radius. The effect of expanding eigenvectors on the convergence is studied.

The Numerical results for the algorithm introduces in Chapter 2 are given in **Chapter 4**. Uncollimated reconstruction from both parallel and cone beam acquisition are visualized along with the collimated reconstruction which is very inaccurate. For our algorithm, the performance of the reconstruction is validated through various performance measures on Shepp Logan phantoms and comparisons with the standard reconstruction are given.

In **Chapter 5** the basic theory is extended to 3D. The definitions and results are restated in this case. First we state the method of reconstructing a 3D object from 2D slices and why it is not suitable. The general data acquisition and inversion formula are described. Collimation is introduced and a collimation condition is derived. The algorithm is extended to 3D and its convergence analysis using the spectral radius is given.

The implementation methods of 2D cannot be directly extended to 3D due to computational efficiency issues. Hence faster techniques need to be introduced which we develop in **Chapter 6**. Using the Fourier Slice Theorem, we introduce a new technique of data acquisition which is computationally much faster. The inversion formula is adapted to this type of data acquisition. We introduce the Spherical acquisition model. The algorithm we described in the previous chapter is slightly modified to suit the 3D case.

Chapter 7 presents a detailed numerical analysis for our algorithm's reconstruction in 3D. The algorithm is tested on Shepp Logan phantoms and randomly generated phantoms. Also testing on real data of a mouse and a human jaw is carried out. Detailed numerical results are provided for the same including the correlation of errors with edges. Another condition for convergence of the algorithm is stated using the concept of Relative Density.

The local averaging regularization technique used up to this point is elementary. The performance of our algorithm can be significantly improved by using sophisticated regularization techniques. Such regularization techniques are explored in **Chapter 8**. There is a special emphasis on wavelet-based regularization methods.

We review the basics of wavelets in one dimension. Non-linear regularization techniques such as hard thresholding (truncation) and soft thresholding (shrinkage) are studied in detail while linear regularization techniques are stated. The performances of reconstruction using different regularization techniques in our algorithm are compared. Finally the effect of regularization in the convergence analysis is detailed.

Chapter 9 deals with the performance of our algorithm in case the data is noisy. The various types of noise which occur naturally in image proceesing are described. We study the case of an acquisition device corrupted by additive Gaussian white noise. The algorithm is tested in such a case and the results are compared to the ones obtained previously. The algorithm is also tested after an initial denoising step.

The industrial approach of the proposed algorithm is described in **Chapter 10**. In most cases of CT scans, a spiral acquisition is used, where the source is moving in a spiral helix around the object. The geometry of spiral tomography is studied. The first theoretically exact reconstruction formula (based on the filtered back-projection) for 3D uncollimated data is given in [41, 43]. This formula is explained in detail. Our algorithms is stated for spiral tomography and the convergence is again studied through spectral radius.

In **Chapter 11** the implementation for data acquisition and numerical performance of our algorithm is given. The data acquisition technique suggested using the Fourier Slice Theorem is adapted to the spiral setting. The algorithm is tested on simulated phantoms and real data for which numerical results are provided. The dependence of the algorithm on parameters is experimented to arrive at a set of optimal parameters for best performance as well as realistic viability.

Chapter 12 provides a brief historical overview of Computed Tomography. Since the collimated 3D problem is relatively unexplored, the attempts on the local reconstruction problem is mainly in 2D. In one case we compare our results with another algorithm (in 2D). The historical attempts at uncollimated as well as collimated reconstruction in 3D (including spiral tomography) are reviewed. In particular the works of Tim Olson and Joe Destefano, Adel Faridani, Alexander Katsevich, David Finch, and Ge Wang are discussed.

Chapter 13 states the advantages and shortcomings of the described algorithm. It discusses the need to eliminate the shortcomings. Some possible changes to the algorithm to make it medically viable are discussed. Finally the prospects of future research in this area are discussed.

Note: Material in this thesis has appeared elsewhere. Parts of Sections 5.2-5.5 and Sections 7.1-7.4 have been published in [5].

CHAPTER 2

Reconstruction of 2D Collimated Data

This is a simpler case of the actual problem we want to study in 3D. The goal of computed tomography is to recover the density function F of whose supported will be denoted by Ω. In this chapter we develop the theory and the algorithmics in 2D. A 2D image can be considered as a function $F : \mathbb{R}^2 \to \mathbb{R}$ with support Ω. Since images are finite, we can assume $F : I^2 \to \mathbb{R}$, where I is a closed and bounded interval in $\mathbb{R}^+$. We first define the 'tomographic' acquisition of data.

2.1 Data Acquisition in 2D

As mentioned in Chapter 1, the X-ray Transform is the mathematical model used to establish a formal relationship between the observed data (i.e., the 1D projection acquired by tomography) and the object under investigation.

Definition 2.1.1. *Let $F : I^2 \to \mathbb{R}$ be a compactly supported, Lebesgue integrable function, θ a unit vector in S^1 and $w \in \mathbb{R}^2$. The **X-ray Transform** of F along the line $l(w, \theta)$, passing through w and in the direction θ is,*

$$XF(w, \theta) = \int_{-\infty}^{\infty} F(w + t\theta)dt. \tag{2.1}$$

The X-ray Transform $F \longrightarrow XF$ is a map from the set $V(\mathbb{R}^2)$ of all lines $l(w, \theta)$ where $w \in \mathbb{R}^2$ and $\theta \in S^1$ into the set $\mathbb{R}$.

Tomographic acquisition in 2 D can be modeled by the X-ray Transform. The X-rays are emitted from a radiating source. The source rotates around the object Ω. The X-rays are emitted by a radiating source. The X-rays pass through Ω where they are attenuated and the resulting attenuation intensities are recorded by a detector, (which is rotating along with the source) placed beyond the Ω. This data acquisition can be formalized in two ways, namely the **parallel beam** acquisition model and the **cone beam** acquisition model.

2.1.1 Parallel Beam Acquisition Model

In this type of acquisition, for each source position, the X-rays are parallel to each other. The source is at an infinite distance from the object. The detector$D$ is

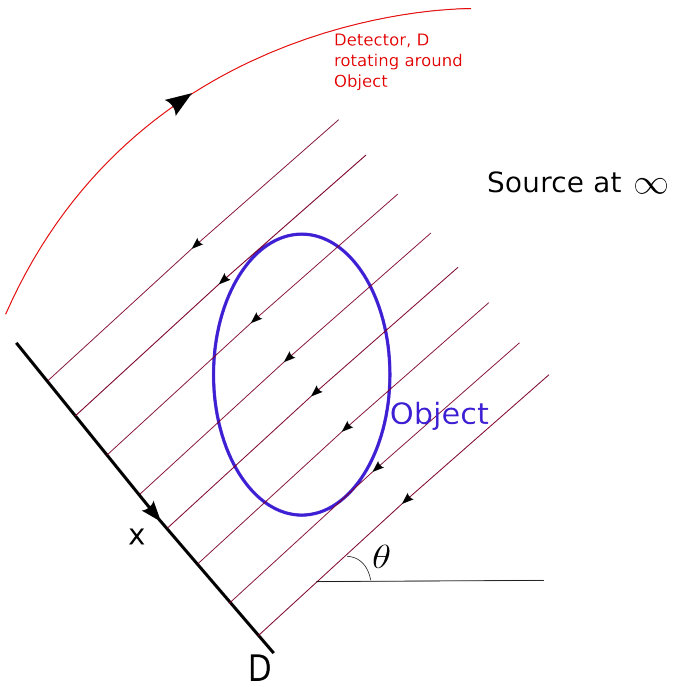

Figure 2.1: Parallel Beam Acquisition Model for a projection angle θ

perpendicular to the X-rays. The detector and the source rotate around the object Ω. Each source position is characterized by the angle θ, measured with respect to the horizontal axis. This angle is called the projection angle. The size of the detector is determined by the diameter of the object Ω, that is the maximum possible distance between two points in the object. Usually the detector is slightly larger than the diameter of Ω. This size remains constant for all source positions. The model for parallel beam acquisition is shown in Figure 2.1.

Due to the symmetrical nature of parallel beams, we only need to vary θ between 0 and π. As mentioned above the detector has a fixed size, say L. A position on the detector is denoted by $x \in [0\ L]$. A line can thus be characterized by the pair (x, θ), with θ the projection angle and x position on the detector.

This acquisition model, though simple is not practical. We require a setup where the source is at a finite distance from the object. So we introduce the cone beam acquisition model.

2.1.2 Cone Beam Acquisition Model

The cone beam acquisition model is more standard in industrial applications. The point source S, is placed at a finite distance d, from the the center O, of the object. The source S, rotates around the object Ω in a circle of radius d. It is assumed that d is large enough to contain the entire support Ω. From S, X-rays are emitted in all directions. For each source position, the projection angle θ is the angle which the ray OS passing through O makes with the horizontal. The size L of the detector is determined as in the parallel beam case. The cone beam acquisition model is shown in Figure 2.2. Though the detector might seem larger than the diameter of Ω, through a simple one-one correspondence it is seen that only the diameter of the object determines L.

Since conical beams are not symmetric, we will require acquisition data for all $\theta \in [0\ 2\pi]$. It will be shown in Section 2.2 the range on θ can be reduced by removing redundancies. So a ray is characterized by (x, θ) where θ is the projection angle and $x \in [0\ L]$. The higher number of required projections is a drawback of the conical acquisition model as it leads to higher exposure to radiation. Despite this, due to its realistic feasibility, this model is widely used. Henceforth we will use this model for several theoretical and numerical developments.

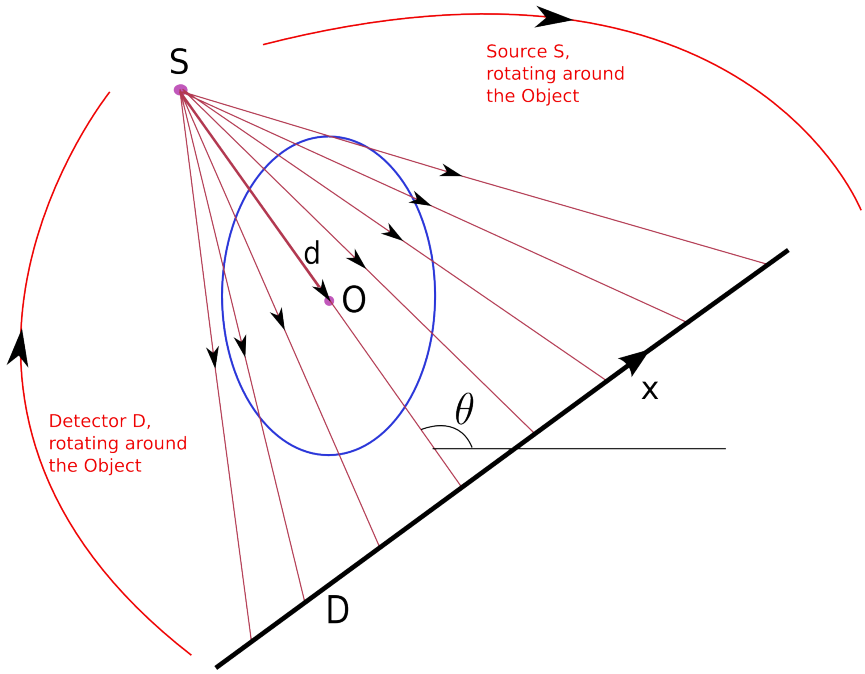

Figure 2.2: Cone Beam Acquisition Model for a source position S with projection angle θ at distance d from the center O, of the object

2.2 Acquisition from Minimal Projections

A major objective of tomographic acquisition is to reduce the patient's exposure to radiation, we recall that it is possible to carry out the cone beam data acquisition without requiring all projections for $0 \leq \theta \leq 2\pi$. Unlike the parallel beam model, the cone beam model is not symmetric, but as shown in Figure 2.3, redundancies do exist. The integrals calculated by the rays SY and $\tilde{S}\tilde{Y}$ are the same.

The source is rotating in a circle with center O and radius d. The detectors are placed at distance d' from O. The arrows on the detector show its orientation. The object, Ω is placed with its center at O. Let the initial position of the source be at S with projection angle θ. Let a ray from S hit the detector at position Y intersecting

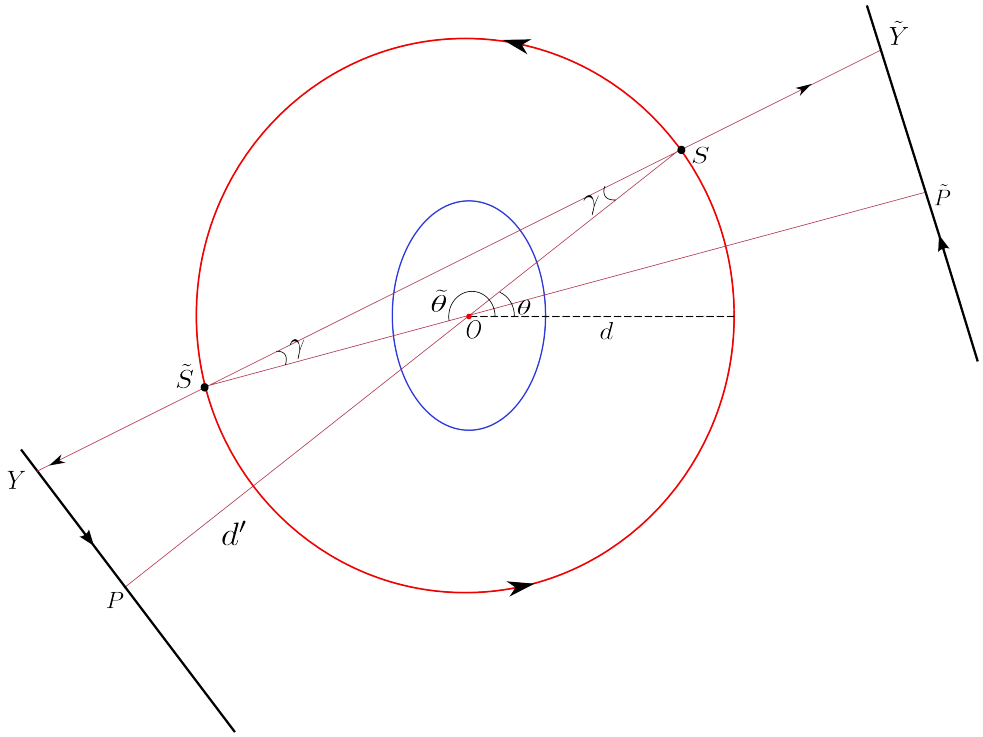

Figure 2.3: Presence of redundancy in Cone Beam Acquisition Model when the segment between source positions S and $\tilde{S}$ gets projected from both these positions

the circle of source rotation at $\tilde{S}$. The ray from S through O hits the detector at P which is the position $\frac{L}{2}$ in the detector. The angle between the central ray and the ray SY is given by,

$$\tan\gamma = \frac{\frac{L}{2} - Y}{d + d'}.$$

Note that as the value of Y changes on the detector, the angle γ will change but will remain within the limits $[-\alpha\ \alpha]$ where α is given by $\tan\alpha = \frac{\tau}{d}$ and τ is the radius of the object.

Now let the source position move to $\tilde{S}$ and $\tilde{\theta}, \tilde{Y}$ and $\tilde{P}$ be the corresponding positions of θ, Y and P. The angle between the central ray and the ray $\tilde{S}\tilde{Y}$ is given

by,

$$\tan(-\gamma) = \frac{\frac{L}{2} - \tilde{Y}}{d + d'}.$$

Equating the two expressions for γ we get,

$$\begin{aligned} \frac{L}{2} - Y &= \tilde{Y} - \frac{L}{2} \\ \Rightarrow \tilde{Y} &= L - Y. \end{aligned} \tag{2.2a}$$

Also by the properties of exterior angles,

$$\tilde{\theta} = \pi + \theta - 2\gamma. \tag{2.2b}$$

From (2.2a) and (2.2b) we get the **Geometric Redundancy Formula**,

$$XF(\tilde{Y}, \tilde{\theta}) = XF(L - Y, \pi + \theta - 2\gamma). \tag{2.3}$$

Now assume that the acquisition data is missing for $\theta \in [0\ T)$, and available for $\theta \in [T\ 2\pi]$. To be able to recover the full data from this, we need

$$0 \leq \theta \leq T \Rightarrow T \leq \pi + \theta - 2\gamma \leq 2\pi \quad \forall \gamma \in [-\alpha\ \alpha],$$

which leads to the two conditions,

$$T \leq \pi - 2\alpha,$$

$$\pi + T + 2\alpha \leq 2\pi.$$

This is the same as the single condition,

$$T \leq \pi - 2\alpha. \tag{2.4}$$

Hence if (2.4) holds we can recover the whole acquisition data set when the data is only known for $\theta \in [T\ 2\pi]$. The maximum such T will correspond to the case with minimal projections and hence minimal exposure.

2.3 Inversion of the X-ray Transform

The problem of interest is to recover F from its X-ray Transform XF. Before deriving the inversion formula, we state the Fourier Slice Theorem in 2D [3, 65].

Theorem 2.3.1. ***(Fourier Slice Theorem)*** *Let $F(x, y)$ be a 2D function which is Lebesgue integrable and has compact support. Let l be a line with direction θ. Denote $XF^{\theta}(w) = XF(w, \theta)$. Then the 1D Fourier Transform of XF^{θ} on a subspace (line), normal to l equals the 2D Fourier Transform of the F on that subspace.*

$$\begin{aligned} \widehat{XF^{\theta}}(\xi) &= \widehat{F}(\xi), \\ \int_{h(\theta)} XF(w,\theta) e^{-i\langle \xi . w \rangle} dw &= \widehat{F}(\xi), \end{aligned} \tag{2.5}$$

where $h(\theta(\xi))$ is the subspace with normal vector $\theta(\xi)$, and $\theta(\xi)$ is any vector orthogonal to ξ.

The classical formula for the inversion of the X-ray Transform is the so-called **filtered back-projection** which is an application of the Fourier Slice Theorem, obtained by applying the 2D inverse Fourier Transform to (2.5).

$$\begin{aligned} F(x,y) &= X^{-1}(XF)(x,y) \\ &= \int_{\mathbb{R}^2} \widehat{XF^\theta}(\xi) e^{i((x,y)\cdot\xi)} d\xi. \end{aligned} \tag{2.6}$$

The inversion formula works well when the acquisition data is complete. Notice that this approach requires the complete knowledge the X-ray Transform of F. As we will see below, this approach becomes unstable if only partial knowledge of the X-ray Transform of F is available.

In general for any function Y, defined on the set of rays $V(\mathbb{R}^2)$ we can define the **Inverse X-ray Transform**, X^{-1} as,

$$X^{-1}Y(x,y) = \int_{\mathbb{R}^2} \widehat{Y^\theta}(\xi) e^{i((x,y).\xi)} d\xi, \tag{2.7}$$

where $Y^\theta(\xi) = Y(\theta, \xi)$.

2.4 Collimation

We are interested in reconstructing a specific region of interest ROI of an object, Ω when only the values of the X-ray Transform associated with the lines of integration passing trough the ROI are available. All other rays are blocked. This collimated acquisition using the cone beam model is shown in Figure 2.4.

Definition 2.4.1. *Let $F : I^2 \to \mathbb{R}$ be a compactly supported, Lebesgue integrable function, θ a unit vector in S^1 and $w \in \mathbb{R}^2$. Let C be a circular region within the support Ω of F. The **Collimated X-ray Transform** of F is defined by,*

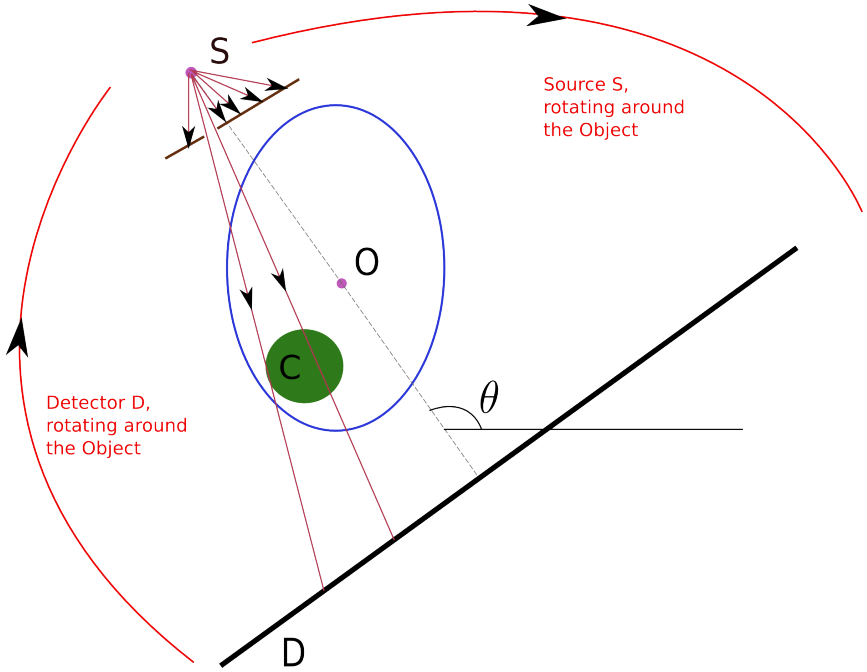

Figure 2.4: The Collimated Cone Beam Acquisition Model for a source position S with projection angle θ at distance d from the center O, of the object and a circular region of interest C

$$\tilde{X}(w,\theta) = \begin{cases} XF(w,\theta) & l(w,\theta) \bigcap C \neq \emptyset \\ 0 & l(w,\theta) \bigcap C = \emptyset \end{cases}. \tag{2.8}$$

The Region of Interest is chosen to be a circle C of center (p,q) and radius R. Consider a line $l(w,\theta)$, which has equation $y = \tan\theta x + (w_2 - w_1 \tan\theta)$ with $w = (w_1, w_2)$. For C and $l(w,\theta)$ to intersect the following system of equations must have a solution in x and y.

$$(x-p)^2 + (y-q)^2 = R^2,$$

$$y = x\tan\theta + (w_2 - w_1\tan\theta).$$

Eliminating y we get a quadratic in x which has a solution if the following condition holds:

$$(\tan\theta(w_2 - w_1\tan\theta - q) - p)^2 - \sec^2\theta(p^2 + (w_2 - w_1\tan\theta - q)^2 - R^2) \geq 0. \quad (2.9)$$

2.5 Non-locality of the Collimated X-ray Transform

Inverting the X-ray Transform is an ill-posed problem, that is the attempt to invert the collimated X-ray Transform through the classical filtered back-projection formula (2.6) is highly inaccurate. We will outline some of the reasons for this in view of [71, 76, 72, 70]. Recall the inversion formula (2.6),

$$F(x,y) = \int_{\mathbb{R}^2} \widehat{XF^\theta}(\xi) e^{i((x,y)\cdot\xi)} d\xi.$$

In terms of the polar coordinates t and θ, the integration can be stated as,

$$F(x,y) = \int_{S^1}\int_{\mathbb{R}} \widehat{XF^\theta}(t)|t| e^{it((x,y)\cdot\theta)} dt d\theta. \quad (2.10)$$

The filtered back-projection uses the inverse Fourier Transform which is infamously non-local. Hence even a local reconstruction requires global properties of the function. Also while computing, the reconstruction is taking place on a radial grid. So to convert back to rectangular coordinates, interpolation or approximation is required. This can create inaccuracies the magnitude of which depend on the nature of F.

For the collimation, we introduce a window function which is usually the characteristic function of an interval $\chi_{[-r\ r]}$,

$$F(x,y) = \int_{S^1} \int_{\mathbb{R}} \widehat{XF^\theta}(t)(\chi_{[-r\ r]}|t|)e^{it((x,y)\cdot\theta)}dtd\theta.$$

This can in fact be written as a convolution. Denoting the 1D inverse Fourier Transform by $\mathcal{F}_1^{-1}$ we get,

$$F(x,y) = \int_{S^1} XF^\theta(t) * \mathcal{F}_1^{-1}(\chi_{[-r\ r]}|t|)d\theta. \tag{2.11}$$

The strict cutoffs at $-r$ and r cause discontinuities and lead to inaccuracies at the edge of the ROI. The absolute value function is not differentiable at the origin. This will also cause problems in local properties, as seen below.

As the name suggests, the filtered back-projection is expressed in two steps. The filtering,

$$Q_\theta(t) = |t|\widehat{XF^\theta}(t),$$

and the back-projection operator,

$$F(x,y) = \int_{S^1} Q_\theta\langle v,\theta\rangle d\theta \qquad \text{where } v = (x,y).$$

The filtering can further be expressed in two steps [76], the differentiation with respect to t and then the application of the Hilbert Transform H, which is given by

$$(H(g))(t) = -\frac{1}{\pi}P.V.\int_{-\infty}^{\infty}\frac{g(u)}{t-u}du. \tag{2.12}$$

So,

$$Q_\theta(t) = H\frac{\partial}{\partial t}XF^\theta(t). \tag{2.13}$$

The Hilbert Transform is again not local. It induces a discontinuity of the Fourier Transform at 0. The imposition of the discontinuity at the origin in the Fourier domain will spread the support of the function in the time domain, that is, the Hilbert Transform of a compactly supported function can never be compactly supported [71, 76]. For this reason, a local basis will not remain local after filtering. Moreover, this implies that all values of XF must be known in order to recover F at (x, y) exactly from this formula.

2.6 Variants of Collimated X-ray Acquisition

Though such variants of collimation are defined rigorously in a mathematical sense, they may not be feasible practically. Hence before using a complicated model for collimation, care should be taken to make sure it is feasible to implement it by realistic modification of CT scan machines.

The collimated acquisition we have described is **complete** (that is all rays outside C are completely blocked) and **hard** (that is strict cutoffs are created at the edge of C). This acquisition modality can be relaxed slightly to attempt a better reconstruction. For a better understanding of various variants of collimation we introduce the notion of **Intensity function**.

Definition 2.6.1. *The Intensity function is a function from the set of all rays in* $\mathbb{R}^2$

to $[0, 1]$*. For any ray* $l(w, \theta)$ *the* ***Intensity function*** J*, maps it to the fraction of the intensity which is allowed to pass after collimation.*

In general we express J as a function of the distance $\rho = \rho(w, \theta)$, of $l(w, \theta)$ from (p, q) which is the center of C.The exact expression for ρ is

$$\rho(w, \theta) = \frac{|p \tan\theta - q + (w_2 - w_1 \tan\theta)|}{\sec\theta}. \tag{2.14}$$

For complete and hard collimation introduced above we have,

$$J(\rho) = \begin{cases} 1 & \rho \leq R \\ 0 & \rho > R \end{cases}. \tag{2.15}$$

In **Partial Collimation** the rays through C are retained fully, while for the other rays a very small fraction ϵ is retained. Typically $\epsilon \leq 0.1$. For partial collimation,

$$J(\rho) = \begin{cases} 1 & \rho \leq R \\ \epsilon & \rho > R \end{cases}. \tag{2.16}$$

If we relax the condition on strict cutoffs which cause discontinuities and instead taper the intensity factor rapidly down to 0 we get **Soft** or **Tapered Collimation**. The tapering takes place within 10% of R. The simplest way to taper is through a linear function.

$$J(\rho) = \begin{cases} 1 & \rho \leq R \\ 11 - \frac{10\rho}{R} & R < \rho \leq 1.1R \\ 0 & \rho > 1.1R \end{cases} . \tag{2.17}$$

This definition clearly implies that that any tapered collimation is always partial. However in most cases we can slightly increase the size of C to make the collimation complete and yet not compromise on the actual interest zone. An interesting approach could be to combine the tapered and the partial collimation. This is the **Soft Partial Collimation**.

$$J(\rho) = \begin{cases} 1 & \rho \leq R \\ 11 - 10\epsilon + \frac{10\rho(\epsilon-1)}{R} & R < \rho \leq 1.1R \\ \epsilon & \rho > 1.1R \end{cases} . \tag{2.18}$$

Tapering forces J to be continuous. However it may not be differentiable (as in the example just given). We also can use a Gaussian Kernel to obtain a smooth function J. To describe such a **Smoothed Soft Partial Collimation** simply, instead of ρ we use the distance $\bar{\rho}$, of a line from C. Of course for any line through C, $\bar{\rho} = 0$ while in other cases $\bar{\rho} = \rho - R$.

$$J(\bar{\rho}) = e^{-\frac{\alpha\bar{\rho}^2}{R^2}}. \tag{2.19}$$

The coefficient $\alpha > 0$ controls the tapering rate. If we use the same tapering region as before then $\alpha = 460$.

2.7 Regularization Operators

A major step in our reconstruction algorithm is the regularization of the estimated values of F outside the region of interest C. Several variants of the regularization operator σ can be employed, and will be discussed for the 3D case in Chapter 8. Here we give the first basic example of a regularization operator. We partition the complement of C into subsets $\{Q_j\}$, having the same fixed area v, and perform local averages. The regularization operator σ is given by:

$$\sigma F(x,y) = \begin{cases} F(x,y) & (x,y) \in C \\ \tau(F,Q_j) & (x,y) \in Q_j \end{cases}, \tag{2.20}$$

where $\tau(F,Q_j) = \dfrac{1}{v}\iint_{Q_j} F(x,y)dxdy$.

For discretized coordinates averages are taken on 2×2 squares. Then the sets Q_j are just these 2×2 squares. Coordinate-wise this can be described by defining for every coordinate $(x,y) \in I^2$,

$$\begin{aligned} \tilde{x} &= x - 1 + (x \mod 2), \\ \tilde{y} &= y - 1 + (y \mod 2). \end{aligned}$$

The function τ defined in (2.20) becomes,

$$\tau(F(x,y)) = \frac{1}{4}\sum_{i=0}^{1}\sum_{j=0}^{1} F(\tilde{x}+i, \tilde{y}+j).$$

2.8 A New Reconstruction Algorithm

We fix a Region of Interest C. In view of the definition (2.4.1), we denote the fully retained set of rays in the collimated X-ray Transform as T and we let U be the complement of T in the set of all rays $V(\mathbb{R}^2)$.

$$T = \{(w, \theta) : l(w, \theta) \bigcap C \neq \emptyset\}.$$

Our **CT Reconstruction Algorithm** for collimated data is initialized by setting

$$G = \tilde{X}F = 1_T.XF, \tag{2.21}$$

where F is the unknown density function and the dot denotes point-wise multiplication, and by computing the initial approximation of F as $f_0 = X^{-1}G$. The subsequent approximations f_n, $n \geq 1$, of F are obtained through the following iterative procedure. Let σ be a fixed regularization operator. Here σ will be of the form (2.20).

1. Compute σf_n as in (2.20).

2. Compute $X\sigma f_n$, the standard X-ray Transform of σf_n, using (2.1). Since T and U are complementary sets, we have,

$$X\sigma f_n = 1_T.X\sigma f_n + 1_U.X\sigma f_n.$$

3. Replace $1_T.X\sigma f_n$ by the known collimated data $G = 1_T.XF$ in the preceding formula to define $Y_n = G + 1_U.X\sigma f_n$.

4. Compute f_{n+1} by applying the X-ray inversion formula (2.7) to Y_n, so that

$$f_{n+1} = X^{-1}Y_n = X^{-1}G + X^{-1}1_U.X\sigma f_n. \tag{2.22}$$

Under mild assumptions, inside the region of interest C the sequence of functions f_n converges to the regularization σF of the unknown density function F. The analysis of the convergence is outlined in the next chapter.

CHAPTER 3

Convergence of Reconstruction Algorithm for Collimated Data

We will call the reconstruction algorithm we have just presented as **Searchlight CT**. We have described the Searchlight CT algorithm for the 2D case. This chapter provides a theoretical approach to analyze the convergence of Searchlight CT. We will begin with an outline of the convergence argument in a general setting. The same arguments hold true for any type of collimated acquisition. This is followed by a numerical analysis of the convergence for the 2D case.

3.1 Analysis of Convergence

Let σ be a regularization operator such as the operator described in (2.20). In addition we assume that the regularization operator σ is a projection, i.e. $\sigma^2 = \sigma$. To discuss the convergence of the algorithm, we need some technical assumptions on the unknown density function F. Specifically, we assume that the support of F is contained in a fixed closed ball $B \subset \mathbb{R}^2$ (or $B \subset \mathbb{R}^3$) for the 3D case), and that the regularized density σF is sufficiently close to F.

The set of X-ray source positions P which could be a circle (or a sphere or a circular helix in 3D) is taken to be disjoint from B and assumed to be large enough to ensure the existence of a formal inverse X^{-1} which is correctly defined for uncollimated data. In 3D this situation is satisfied, in particular, if P is a complete sphere. With notations being exactly the same as Chapter 2, recall the iteration given by (2.22).

$$f_{n+1} = X^{-1}Y_n = X^{-1}G + X^{-1}1_U.X\sigma f_n.$$

The iterative algorithm generates f_{n+1} from f_n by (2.22), starting from the given collimated data $G = 1_T.XF$. Since σ is idempotent, the functions $h_n = \sigma f_n$ satisfy the iterative formula,

$$h_{n+1} = \sigma X^{-1}G + \sigma X^{-1}(1_U.Xh_n). \tag{3.1}$$

Denote by A the fixed function

$$A = \sigma X^{-1}G$$

on $\mathbb{R}^2$, taking values in $\mathbb{R}^+$ and by M the linear operator which maps h to

$$Mh = \sigma X^{-1} 1_U . X \sigma h.$$

Hence, we have

$$h_{n+1} = A + Mh_n, \tag{3.2a}$$

which implies

$$h_{n+1} - h_n = M(h_n - h_{n-1}). \tag{3.2b}$$

Assume that the density functions F lies in a vector space H such that the space $\sigma(H)$ of regularized densities can be endowed with a Banach norm for which the operator M becomes a strict contraction in the Banach space $\sigma(H)$, then the iteration converges to the fixed point.

The sequence of functions h_n converges to a limit h in $\sigma(H)$, and the limit h satisfies

$$h = A + Mh. \tag{3.3}$$

Since M is a strict contraction, this last equation has a unique solution in $\sigma(H)$ which is the fixed point of the iteration (3.2a).

We now prove that $\tilde{F} = \sigma F$ verifies

$$A + M\tilde{F} = \sigma X^{-1}(1_T . X\tilde{F}) + \sigma X^{-1}(1_U . X\tilde{F}) = \sigma\tilde{F} = \tilde{F}, \tag{3.4}$$

which, by the uniqueness of h, implies $h = \sigma F$. The iteration always converges to σF and hence for $F \in \sigma(H)$, the iterative approximations h_n converge to the true density function F.

However, in general, $F \notin \sigma(H)$ and, in this situation, the iterative procedure will only produce an approximation of the unknown F by σF. Since M is a strict contraction, the operator $Id - M$ has a bounded inverse and hence the solution h of the equation $h = A + Mh$ is continuous in A. Thus, if F and $\sigma(F)$ are sufficiently close, then the limit h of h_n, as $n \to \infty$, is as close as desired to the unknown function F.

A necessary condition for convergence is that the norm of the function F outside S is sufficiently small. This can be verified by considering a function which vanishes inside C. Extensive numerical tests have indeed verified that the algorithm converges under reasonable conditions on the space H and the regularization operator σ, provided that the circular region of interest C is large enough, and provided that the indicator function 1_U is regularized in the space of rays by convolution with a Gaussian kernel.

3.2 Numerical Analysis of Contraction Properties in 2D

In this section, we will analyze the convergence properties of the algorithm in 2D by calculating the spectral radius, ρ of the iteration matrix $M = \sigma X^{-1} 1_U X \sigma$. To make this numerically feasible, we use small data size. The procedure for this is summarized below.

To keep the dimensions reasonable we will consider a small object Ω of dimension

45×45 pixels. The discretization of the circle of positions of the rotating source is kept at a relatively large 6°. So there are 60 source positions. The size of the detector is 69 pixels. This makes the size of each projection image 69×60. The discretized X-ray Transform can then be viewed as an image of size 69×60. Hence the X-ray Transform X, can be interpreted as a linear operator $X : \mathbb{R}^{45\times45} \longrightarrow \mathbb{R}^{69\times60}$ or alternatively $X : \mathbb{R}^{2025} \longrightarrow \mathbb{R}^{4140}$.

However, due to regularization by local averaging we know that outside the region C, the densities will be constant in 2×2 boxes. This fact can be used to significantly reduce the dimensions of the iteration matrix M. Of course this reduction is dependent upon the size of C. To compute the matrix Q of X, we will consider the following basis. For a point (i, j) inside C, we associate a matrix of size 45×45 with 1 in the (i, j)-th coordinate and zeros in the rest. For a point (i, j) outside C, it will be $\frac{1}{4}$ at the four coordinates in the 2×2 box where (i, j) is located and zero otherwise. These canonical basis matrices are denoted by E_k. The size of this basis is the reduced dimension and denoted by z.

XE_k is the discretized X-ray Transform image of size 69×60. Listing this as a vector we get a vector of length 4140 which is the $k-$th column of Q. Carrying this out for each of the basis matrices we get Q of size $z \times 4140$.

We can find the matrices for σ (dimension $z \times z$) and X^{-1} (dimension $4140 \times z$) in a similar way. Note that 1_U is an affine transformation which involves a projection first which is followed by an addition of a vector. We just need to calculate the the matrix of the projection (dimension 4140×4140) the projection in the calculation of the spectral radius. Denote M as the matrix for $\sigma X^{-1} 1_U X \sigma$. We calculate the

eigenvalues of M and in turn the spectral radius.

Definition 3.2.1. *Let A be a matrix in $\mathbb{R}^{n\times n}$. The spectral radius $\rho(A)$ of A is defined as,*

$$\max_i |\lambda_i|, \tag{3.5}$$

where $\lambda_1, \ldots \lambda_n$ are eigenvalues of A.

The set $\mathcal{B}$ of eigenvectors of M, forms orthonormal basis of $\mathbb{R}^n$ where n is the reduced dimension, z of $\mathbb{R}^{2025}$ as seen in Table 3.1. Hence the function F can be expanded as a linear combination of the eigenvectors,

$$F = \sum_{i=1}^{n} \gamma_i v_i = \sum_{i=1}^{n} \langle F, v_i \rangle v_i \qquad v_i \in \mathcal{B}. \tag{3.6}$$

We also introduce the following terminology.

Definition 3.2.2. *For a matrix E, let $\varsigma(E)$ be its spectrum. For any eigenvalue $\lambda \in \varsigma(E)$ we say λ is a **contracting eigenvalue** if $|\lambda| < 1$ and the corresponding eigenvector is called a **contracting eigenvector**. If $|\lambda| \geq 1$ then λ is said to be a **expanding eigenvalue** and the corresponding eigenvector a **expanding eigenvector**.*

*The subspace spanned by all contracting eigenvectors of E is the **contracting subspace** of E and the one spanned by the expanding eigenvectors is the **expanding subspace** of E.*

The spectral radius $\rho(M)$ is tabulated in Table 3.1, where for radii of C between

Table 3.1: Spectral radius $\rho(M)$ for various ROI-radii

ROI-radius	Reduced Dimension,z	$\rho(M)$
4 pixels	552	14.55
7 pixels	652	9.26
8 pixels	700	7.81
9 pixels	756	4.06
10 pixels	812	0.82
13 pixels	1024	0.69
16 pixels	1300	0.63

4 and 16 pixels, we calculated the spectral radius, $\rho(M)$ of M. The corresponding plot is shown in Figure 3.1

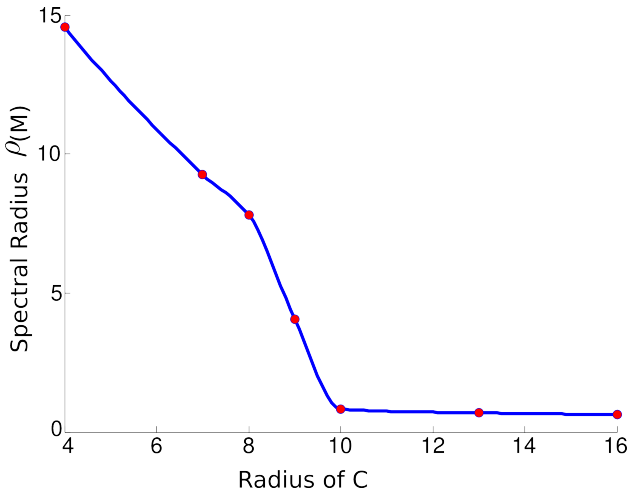

Figure 3.1: Spectral radius, $\rho(M)$ plotted as a function of ROI radius

The observations from Table 3.1 indicate that, for convergence to occur, the radius of C has to be sufficiently large. A minimal radius of 10 pixels was required for $\rho(M)$ to be less than 1. For a case where convergence occurs (with a radius of 13 pixels), the histogram for the eigenvalues of M is shown in Figure 3.2 showing that all the eigenvalues and hence ρ is less than 1.

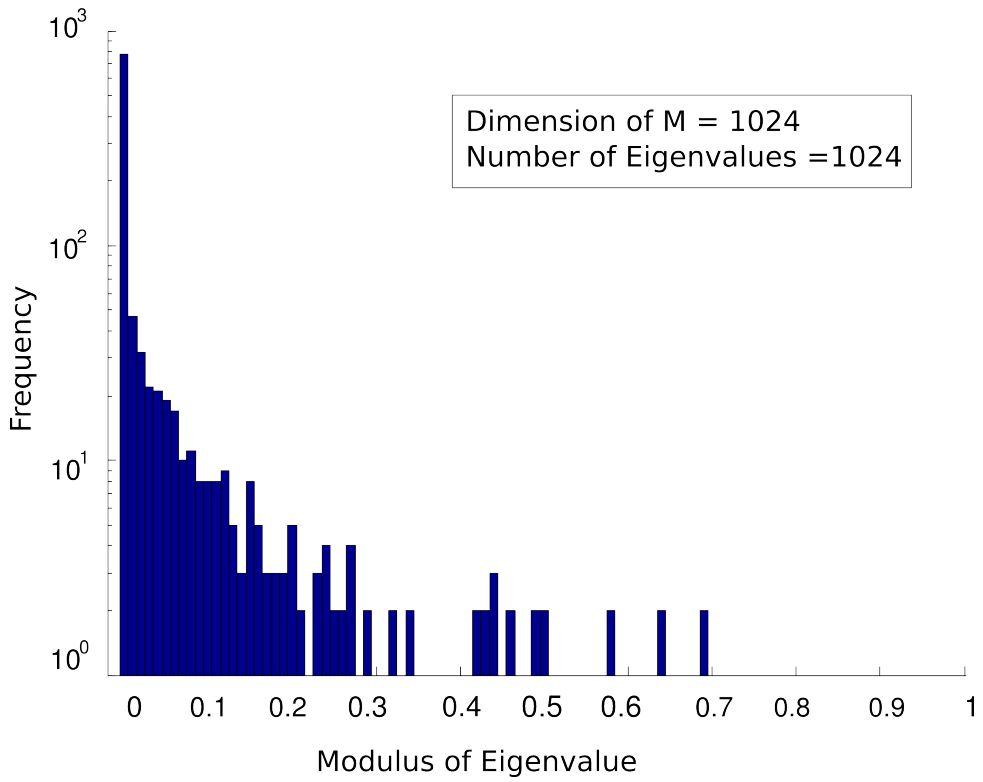

Figure 3.2: Histogram for the eigenvalues of M for a converging case when the radius of C is 13 pixels

The regularization step used in the technique mentioned above is very important. Without this regularization, the spectral radius $\rho(N)$ of the operator $N = X^{-1}1_U X$, is significantly larger. Some examples are given in Table 3.2.

By contrast, for very small ROI-radius, some eigenvalues are greater than 1 which

Table 3.2: Comparison of Spectral radii $\rho(M)$ and $\rho(N)$ for various ROI-radii

ROI-radius	8 pixels	9 pixels	10 pixels	13 pixels	16 pixels
$\rho(\mathbf{M})$	7.81	4.06	0.82	0.69	0.63
$\rho(\mathbf{N})$	10.36	7.54	2.43	2.12	1.79

lead to divergence. The histogram for the eigenvalues of M in a case when convergence does not occur (with a radius of 8 pixels) is shown in Figure 3.3, showing that several eigenvalues are greater than 1.

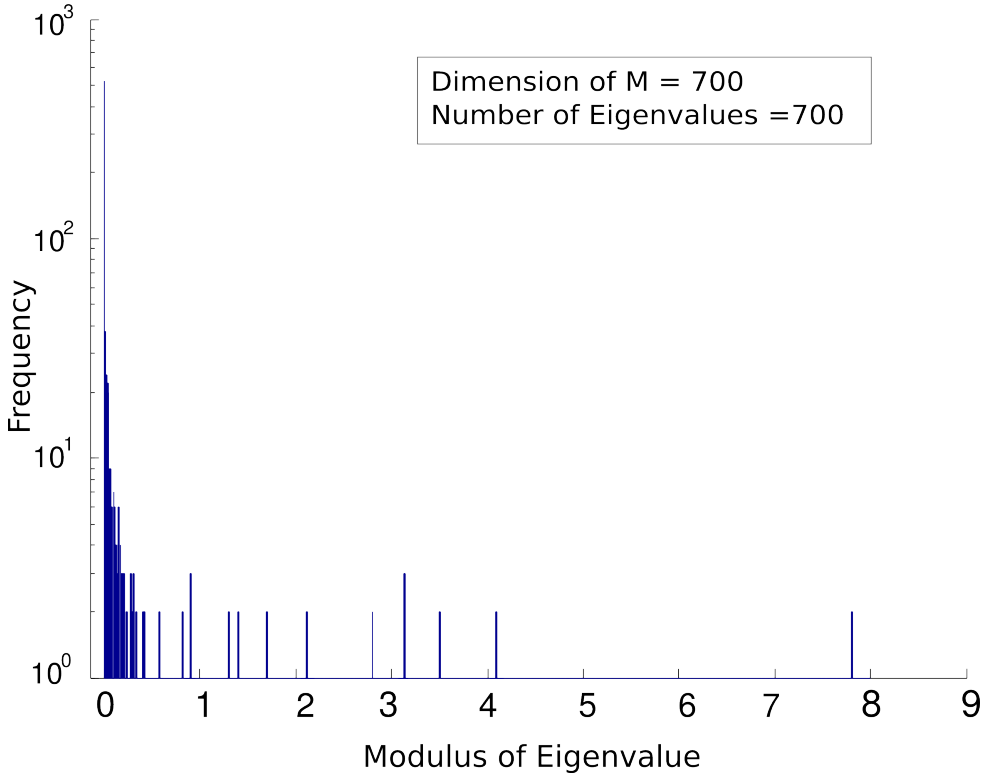

Figure 3.3: Histogram for the eigenvalues of M for a diverging case when the ROI has a small radius of 8 pixels

Note that our numerical analysis of the spectral radius of M does not depend on the unknown density function F but only on the size of data and the radius of the ROI, C. If we change the object but keep the same C we will obtain the same spectral radius for M. This can be stated as the following theorem:

Theorem 3.2.3. *Let $F : \mathbb{R}^2 \longrightarrow \mathbb{R}$ be a Lebesgue integrable function with compact support Ω. For a given 2D acquisition geometry let X be the X-ray Transform (on*

a set of rays V) and X^{-1} be its corresponding inverse. Let σ be a regularization operator such that $\sigma^2 = \sigma$. For a region of interest $C \subset \Omega$ let $T \subset V$ be the set of rays which pass through C and $U = V \setminus T$. Set $G = 1_T.XF$ and $f_0 = X^{-1}G$. Then sequence of iterates given by,

$$f_{n+1} = A + Mf_n,$$

with $A = X^{-1}G$ and $M = \sigma X^{-1} 1_U X \sigma$, converges to σF within C if and only if the spectral radius $\rho(M) < 1$.

However if we change the regularization operator σ we can expect to modify the spectral radius associated to a given ROI C. This is studied in Section 8.5.

3.3 Analysis of the Expanding Eigenvectors

For the diverging cases of the algorithm it is of interest to analyze the expanding eigenvectors (corresponding to the eigenvalues of M higher than 1). The concentration of these eigenvectors on certain zones of in the support of F show how these eigenvectors affect the convergence. For this purpose we need to identify the 'high intensity coordinates' of the eigenvector. Since we fail to get convergence inside C, we expect these eigenvectors to be concentrated within C. That is done in the following way.

For an eigenvector v, let v_n be the vector where the n coordinates of v with highest modulus are retained and the rest are set to zero. Let

$$\epsilon_n = \|v - v_n\|. \tag{3.7}$$

Let m be the smallest integer such that $\frac{\epsilon_m}{\|v\|} < 85\%$. Now the support of v_m will identify the 'high intensity zones' of v. For the case shown in Figure 3.3, the eigenvector corresponding to the highest eigenvalue was plotted and its high intensity zones were located as just described. This is shown in Figure 3.4 confirming that a substantial fraction of the high intensities are within C.

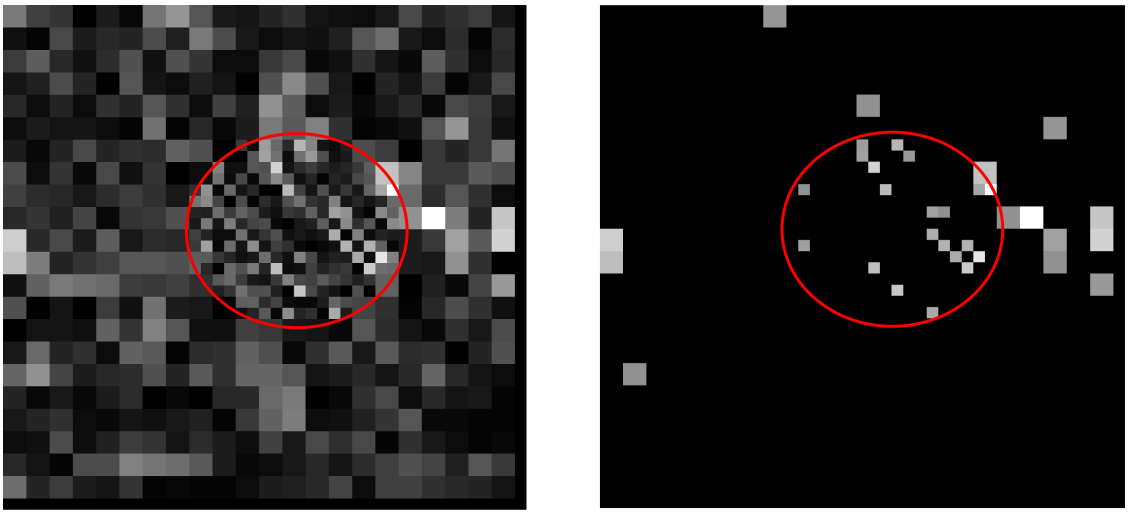

Figure 3.4: For the diverging case when radius of C is 8 pixels (a) Image of the eigenvector corresponding to the highest eigenvalue and (b) The location of the $m = 76$ coordinates of v with highest modulus

When the diameter of C is smaller than the critical diameter (of 10 pixels in this case), the operator M is not a contraction but it might be still possible to get an acceptable reconstruction of C. This can happen if the weights (absolute coefficients in the expansion (3.6)) associated to the expanding eigenvectors are small enough. For convenience assume that the first k eigenvectors are the expanding ones.

Definition 3.3.1. *For any eigenvector v_i the associated* ***weight*** *is* $|\gamma_i| = |\langle F, v_i \rangle|$

Table 3.3: Expansion weight, ω for various small radii of C

C-radius	Reduced Dimension	Expansion Weight, ω_d
4 pixels	552	6.52%
5 pixels	576	5.36%
6 pixels	616	4.01%
7 pixels	652	3.13%
8 pixels	700	1.86%

where γ_i is as described in (3.6)*. The* ***expansion weight*** *ω_d, is the fraction of the total weights associated with expanding eigenvectors. That is,*

$$\omega_d = \frac{\sum_{i=1}^{k} |\langle F, v_i \rangle|}{\sum_{i=1}^{n} |\langle F, v_i \rangle|}. \tag{3.8}$$

Consequently the ***contraction weight*** *ω_c is given by $\omega_c = 1 - \omega_d$.*

To determine the effect of the expanding eigenvectors we calculate expansion weights for various (small) radii of C between 4 and 8 pixels. This is tabulated in Table 3.3.

Next we see the effect of these expanding eigenvectors on the objective function F which we assume F to be already regularized. To achieve this, we project F into the contracting subspace to obtain an approximation of F, that is, we set to zero the coefficients (weights) corresponding to the expanding eigenvectors in (3.6), obtaining:

$$PF = \sum_{i=m+1}^{n} \gamma_i v_i = \sum_{i=k+1}^{n} \langle F, v_i \rangle v_i. \tag{3.9}$$

It is expected that in cases ω_d is small enough, PF is sufficiently close to F. It is observed that ω_d increases with the decrease in radius of C. However when regularizing by local averages, only for the largest radius of 8 pixels is the projection PF close enough to P. For smaller radii PF is not an accurate approximation. Both these cases of accurate and inaccurate projections are shown in Figure 3.5.

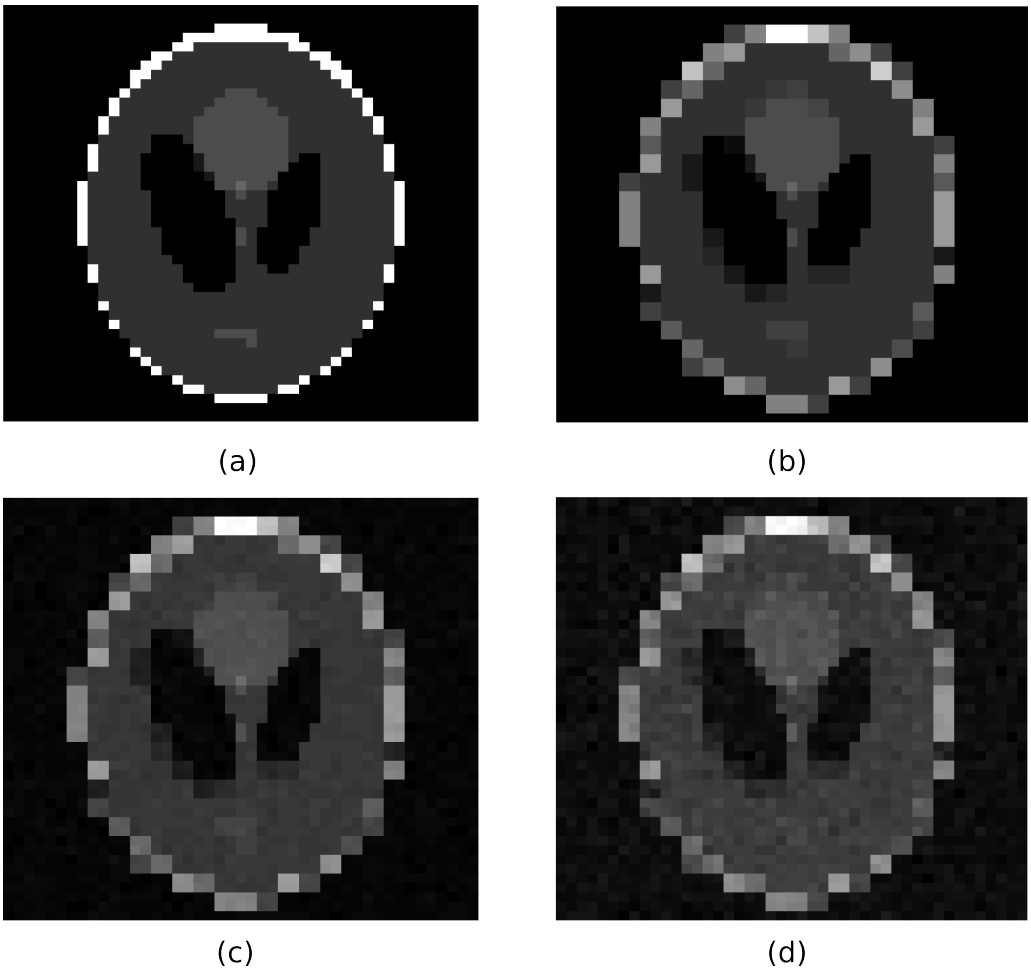

Figure 3.5: (a) The Shepp-Logan phantom of size 45 (b) The phantom regularized outside the region C of radius 8 pixels (c) The projection of the regularized phantom with radius of C 8 pixels on to the contracting subspace of M_N(d) The projection of the regularized phantom with radius of C 5 pixels on to the contracting subspace of M_N

The approximation by projecting on to the contracting subspace can be improved by using sophisticated regularization operators as will be seen in 8.5. In future work we plan to study further this effect in order to extend the reconstruction algorithm provided here.

CHAPTER 4

Numerical Results for Reconstruction of 2D Collimated Data

In this chapter we present the numerical and visual results of our algorithm in 2D and compare it to the standard reconstruction case in terms of various performance measures. For simulations we need to discretize the settings. The 2D density function F is now assumed to be defined on $N \times N$ pixel grid $I^2 \rightarrow [0\ 1]$, where I is a set of discrete pixel coordinates of the form $I = \{1, 2, 3, \ldots N\}$.

For our experiments we have used the **2D Shepp-Logan phantom** with $N = 257$ as our simulated phantom. The phantom is shown in Figure 4.1.

Figure 4.1: 2D Shepp-Logan phantom

To simulate the acquisition, we discretize the projection angle θ. We use a discretization, $a = 0.4^{\circ}$.

4.1 Reconstruction for 2D Uncollimated Acquisition

For the parallel beam case, this discretization of θ leads to 450 source positions enumerated as S_i. The size of the detector (determined by the diameter of the phantom) is 369 pixels. When the acquisition (Figure 4.2) is uncollimated the inversion using the standard reconstruction method (2.6) gives an accurate reconstruction as shown in Figure 4.3.

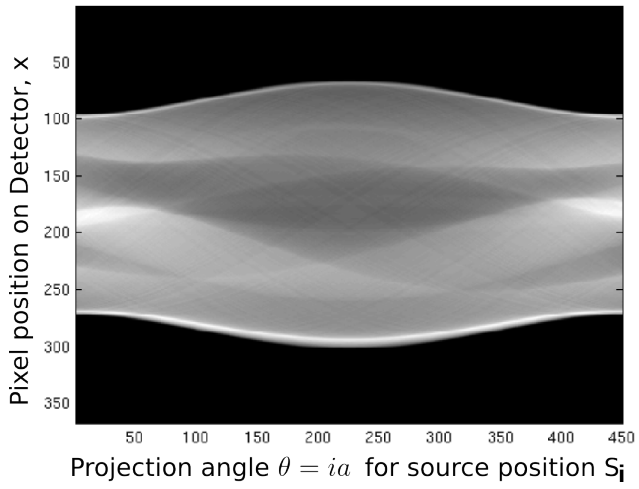

Figure 4.2: **Uncollimated** X-ray Transform of the Shepp-Logan phantom 4.1 using the parallel beam acquisition model

Figure 4.3: Inversion from the **uncollimated** X-ray Transform 4.2 using the Standard Reconstruction

In the cone beam case the only difference is that for $a = 0.4°$, we get 900 source positions enumerated as S_i. When the acquisition (Figure 4.4) is uncollimated, the standard reconstruction again gives an accurate reconstruction (Figure 4.5).

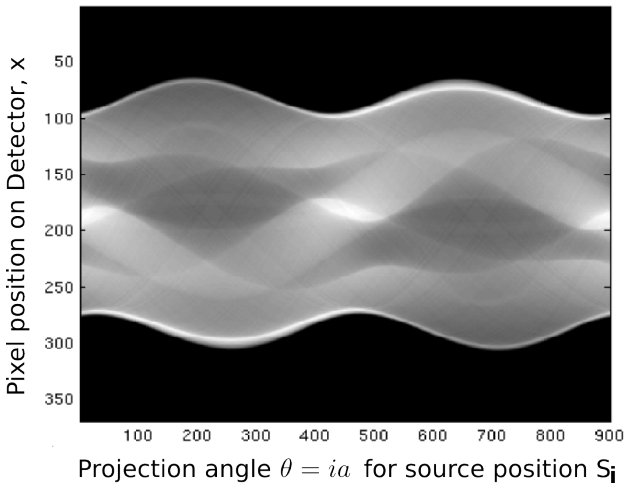

Figure 4.4: **Uncollimated** X-ray Transform of the Shepp-Logan phantom 4.1 using the cone beam acquisition model

4.2 Reconstruction from 2D Collimated Acquisition

Next we consider the collimated case (complete and hard). We choose a region C of radius 50 pixels within the phantom, which is shown in Figure 4.6. Since only the X-rays though C are allowed to pass through, the collimated X-ray Transform looks truncated as in Figure 4.7.

As expected this gives an inaccurate reconstruction. The inaccuracies are especially pronounced at the edges. This correlation will be discussed in more detail in

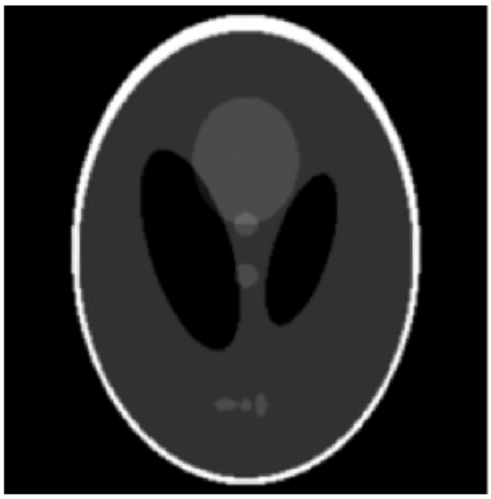

Figure 4.5: Inversion from the **uncollimated** X-ray Transform 4.4 using the Standard Reconstruction

Section 7.5. The Searchlight CT algorithm attempts a better reconstruction which is evident in Figure 4.8(b). A comparison between the standard reconstruction, the Searchlight CT reconstruction and the ground truth is shown in Figure 4.8.

As it is seen in Figure 4.8 The Searchlight CT algorithm performs a far better reconstruction. The standard reconstruction produces high intensities at the edges and several artifacts inside C. The reconstruction through Searchlight CT on the other hand is comparable to the ground truth.

The iteration is very fast in 2D. Each iteration ran in less than a minute. We required at most 15 iterations for convergence which ran in a total of 13 minutes.

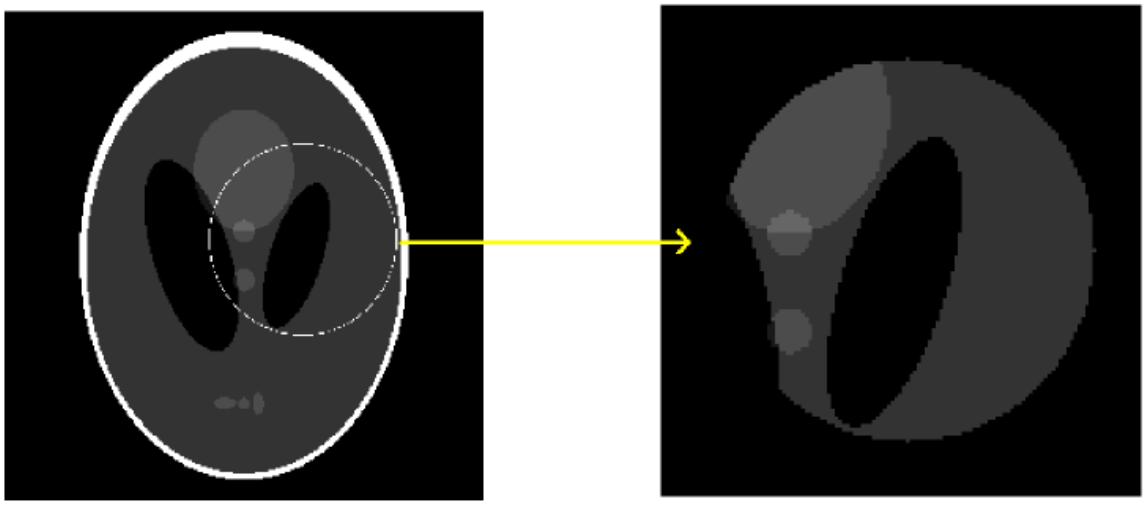

Figure 4.6: Collimated Acquisition: Position of the region of interest C of radius 50 pixels in the Shepp-Logan phantom

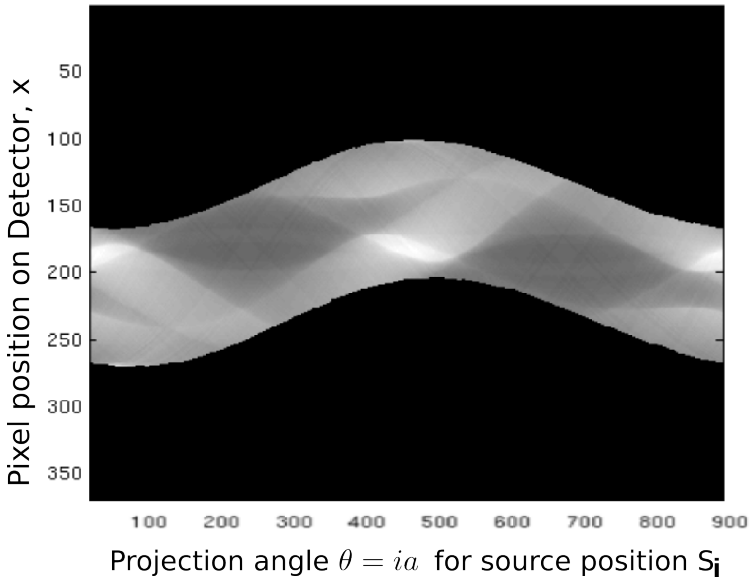

Figure 4.7: The **collimated** X-ray Transform corresponding to the region C of radius 50 pixels, 4.6 in the Shepp-Logan phantom 4.1

(a) Standard Reconstruction (b) Searchlight CT (c) Ground Truth

Figure 4.8: A comparison of reconstruction methods for the region of interest C 4.6 (a) Standard Reconstruction through the filtered back-projection (b) Reconstruction through Searchlight CT (c) Ground Truth

4.3 Numerical Quantification of Reconstruction Accuracy

While visual inspection give a good qualitative comparison between various reconstruction accuracies, they often fail to quantify the minute differences. We now quantify reconstruction accuracy much more precisely.

Definition 4.3.1. *Let F be the density function to reconstruct and F_{rec} be a reconstruction of F. The **Relative Reconstruction Error**, Rel is defined by,*

$$Rel = \sum_{v \in C} \frac{\|F(v) - F_{rec}(v)\|}{\|F(v)\|}, \tag{4.1}$$

where C is a circular region of interest in the support of F.

We can use the L_1 or the L_2 norm. Table 4.1 provides the relative reconstruction

Table 4.1: Performance of reconstruction methods for various ROI-radii

ROI-radius	*Rel* (Standard)	*Rel* (Searchlight CT)	Exposure
50	11.2%	4.1%	27%
60	11.0%	3.8%	35%
70	10.8%	3.7%	46%

errors for various radii of C methods (in the mentioned region) using the L_2-norm when reconstructed through Searchlight CT. For soft partial collimation $\epsilon = 0.01$.

Another important performance measure for a is the exposure of a patient to radiation.

Definition 4.3.2. *The radiation dose $\delta(v)$ received by a pixel v is defined as the number of rays passing through v. Let $c = \sum_{v \in I^2} \delta(v)$ be the sum of received doses over all pixels, in the case of collimated irradiation, and m be the maximal dose which is received in the uncollimated case. We define the* ***Radiation Exposure*** *E, as*

$$E = \frac{c}{m}. \tag{4.2}$$

The radiation exposure, E for various radii of C is also tabulated in Table 4.1.

Note that the Searchlight CT algorithm and standard reconstruction have the same exposure levels however Searchlight CT has significantly higher accuracy. Reconstruction from uncollimated acquisition performs well but the exposure is 100% which is much higher than Searchlight CT. Hence Searchlight CT saves on significantly on exposure with minimal compromise in reconstruction accuracy. A more detailed analysis of the numerical quantification will be presented for the 3D case in Chapter 7.

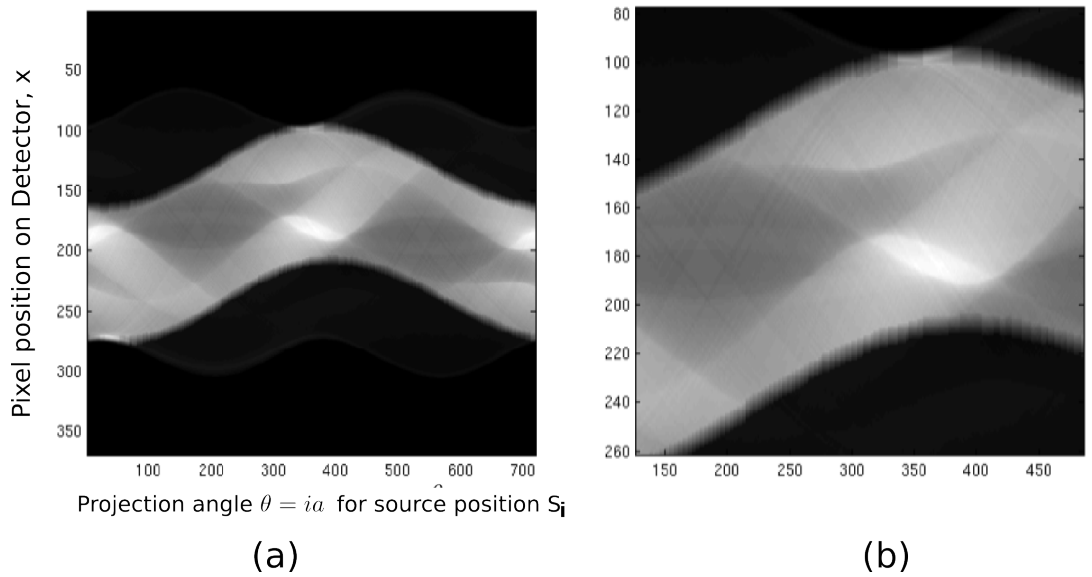

Figure 4.9: (a)The soft partial collimated X-ray Transform corresponding to the region C (b) a zoomed view of the adjoining figure emphasizing the tapering

4.4 Soft Partial Collimation

Instead of using complete and hard collimation we can use one of the variants. For example, in soft partial collimation, the tapering is evident in the acquisition (Figure 4.9). Here we have used a linear tapering and $\epsilon = 0.1$ in (2.18).

The reconstruction which does not look significantly different from Figure 4.8(b) is slightly better, as will be seen in the next section. This is shown is Figure 4.10.

For a soft partial collimation with $\epsilon = 0.01$ and radius of C 50 pixels Relative Reconstruction Error is 3.9% while exposure is 34%. Here the reconstruction error is slightly lower but exposure is slightly higher as compared to complete and hard collimation.

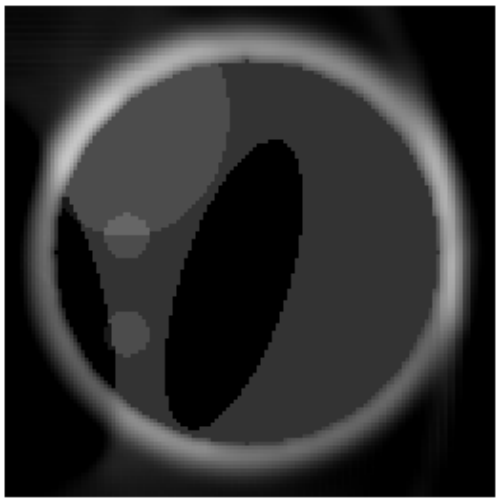

Figure 4.10: Reconstruction through Searchlight CT from the soft partial collimated X-ray Transform shown in Figure 4.9

CHAPTER 5

Reconstruction of 3D Collimated Data with Spherical Acquisition

In real life all objects and acquisition devices are three dimensional. Hence all the theoretical and practical applications from the previous chapter need to be extended to 3D to be applicable in industrial contexts. The next three chapters discuss the 3D problem with spherical acquisition, that is when the source is assumed to rotate in a spherical surface. In Chapter 10 it will be seen that our reconstruction algorithm for collimated acquisition data works well even when the source positions are on a spiral helix.

Though most of the theory from circular acquisition in the 2D case can directly be extended to spherical acquisition in 3D, the numerical extension is far more challenging due to the much higher computational burden. Direct implementation of the theory would lead to unacceptably high CPU time which would be impractical in the medical 3D imaging applications. Hence it is crucial to devise computationally viable methods in the implementation. In the next chapter such methods will be presented after the general theory in this chapter. We begin with the 3D reconstruction from 2D slices.

5.1 3D Reconstruction from 2D Slices

The simplest way to extend a 2D method to 3D is to use 2D slices in a 3D object. The 3D object is divided into 2D slices. On each of the slices the 2D method is applied individually. Though this seems a natural extension, several problems arise. First, it is computationally very expensive to reconstruct every slice specially in the case of our algorithm where acquisition and reconstruction are iterated. Hence we have analyzed a scheme where one would reconstruct only a fraction of the slices and interpolate between them. This is shown in Figure 5.1.

The interpolation could be carried out in several ways. It can be done in the X-ray domain right after the data acquisition. Alternatively the known slices can first be reconstructed and then interpolation be performed in the image domain. A slightly more advanced technique could be to detect the edges (through any gradient-based edge detector, for example [34]) and interpolate between edges by using the wavelet

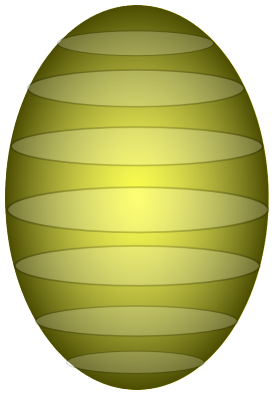

Figure 5.1: Reconstruction of 2D slices: The object is reconstructed on a few horizontal slices as shown and interpolated in the space between them

transform [86].

However all these methods fail to retain major characteristics of the original image. For example the piece-wise constant nature of the Shepp-Logan phantoms is not retained anymore. In real data the inaccuracies are magnified due to the irregular nature of the image.

After several numerical experiments with 3D phantom data, we have concluded that 3D reconstruction from 2D slices is inaccurate and practically infeasible. We omit the presentation of these negative results which has led us to develop a far more efficient reconstruction technique.

5.2 Data Acquisition in 3D

We start by defining the **X-ray Transform** in 3D.

Definition 5.2.1. *Let* $F : I^3 \to \mathbb{R}$ *be a compactly supported, Lebesgue integrable*

function, θ a unit vector in S^2 and $w \in \mathbb{R}^3$. The ***X-ray Transform*** *of F along the line $l(w, \theta)$, passing through w and in the direction θ is,*

$$XF(w, \theta) = \int_{-\infty}^{\infty} F(w + t\theta)dt. \tag{5.1}$$

The X-ray Transform can be viewed as a real valued function on the set $V(\mathbb{R}^3)$ of rays in $\mathbb{R}^3$ which associates to each ray l the line integral of F along the ray l.

Remark 5.2.2. It must be noted that the X-ray Transform is different from the Radon Transform [65, 2]. In general in n dimensions the Radon Transform computes integrals over $(n-1)$-dimensional hyper-planes while the X-ray Transform always computes integrals over lines. In 2D the two coincide. But is 3D the X-ray Transform is a set of line integrals whereas the Radon Transform is a set of plane integrals.

There can be several ways to acquire data in 3D. We will study the situation the source is rotating on a fixed sphere surrounding the object $\Omega \in \mathbb{R}^3$. Note that Ω is essentially identical to the support of the unknown density function F. This is shown if Figure 5.2.

The direct calculation of the X-ray Transform from the definition is computationally expensive. Hence we will introduce a method using the Fourier Slice theorem the simulation of collimated acquisition of the X-ray Transform data. The Fourier Slice Theorem for 3D functions is stated below.

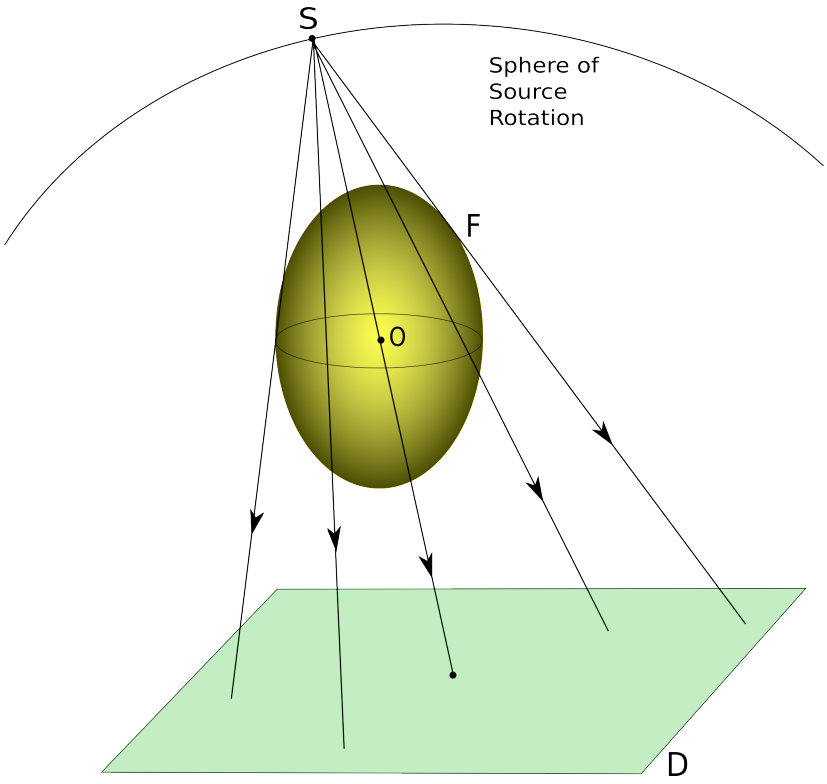

Figure 5.2: The Spherical Data Acquisition model for a source position S and detector D orthogonal to SO

Theorem 5.2.3. ***(Fourier Slice Theorem)*** *Let $F(x, y, z)$ be a real valued function on $\mathbb{R}^3$ which is Lebesgue integrable and has compact support Ω. Let l be a ray with direction θ. Let $\hat{F}$ be the 3D Fourier Transform of F.*

$$\hat{F}(\xi) = \int_{\mathbb{R}^3} F(v)e^{-i\langle \xi, v\rangle}dv \qquad \text{where } v = (x, y, z). \tag{5.2}$$

For all $\xi \in \mathbb{R}^3$ and all unit vectors $\theta \in S^2$ that are orthogonal to ξ we have,

$$\int_{h(\theta)} XF(w, \theta)e^{-i\langle \xi . w\rangle}dw = \widehat{F}(\xi), \tag{5.3}$$

where $h(\theta)$ is the subspace (plane) orthogonal to θ.

5.3 Inversion of the 3D X-ray Transform

The classical formula for the inversion of the X-ray Transform is the **3D filtered back-projection** which is an application of the Fourier Slice Theorem, obtained by applying the 3D inverse Fourier Transform to (5.3). Let,

$$\widehat{XF^\theta}(\xi) = \int_{h(\theta)} XF(w, \theta)e^{-i\langle w, \xi\rangle}dw, \tag{5.4}$$

then,

$$F(x, y, z) = \int_{\mathbb{R}^3} \widehat{XF^\theta}(\xi)e^{i((x,y,z)\cdot\xi)}d\xi. \tag{5.5}$$

In general for any function Y on the set of rays $V(\mathbb{R}^3)$, the **3D Inverse X-ray Transform** can be defined similarly. Let,

$$\widehat{Y^\theta}(\xi) = \int_{h(\theta)} Y(w, \theta)e^{-i\langle w, \xi\rangle}dw, \tag{5.6}$$

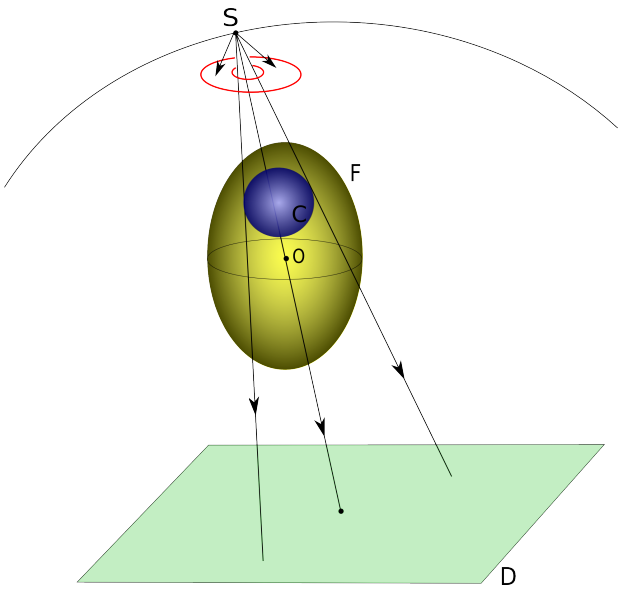

Figure 5.3: The collimated spherical acquisition model corresponding to a source position S, a spherical region of interest C and the detector placed orthogonal to SO

then,

$$X^{-1}Y(x,y,z) = \int_{\mathbb{R}^3} \widehat{Y^\theta}(\xi) e^{i((x,y,z)\cdot\xi)} d\xi. \tag{5.7}$$

5.4 Collimated Acquisition

To model the collimated acquisition we only allow the rays passing through a region of interest C to pass through the object. The physical setup of this is shown in Figure 5.3.

Formally the collimated X-ray Transform in 3D is defined exactly as in the 2D case.

Definition 5.4.1. *Let F be a real valued function in $\mathbb{R}^3$ which is compactly supported*

and Lebesgue integrable, $w \in \mathbb{R}^3$ and$\theta \in S^2$. Let C be a spherical region within the support of F. The ***Collimated X-ray Transform*** *of F is defined as,*

$$\tilde{X}(w,\theta) = \begin{cases} XF(w,\theta) & l(w,\theta) \bigcap C \neq \emptyset \\ 0 & l(w,\theta) \bigcap C = \emptyset \end{cases}. \tag{5.8}$$

We have chosen the region of interest C to be a sphere with center (p,q,r) and radius R. For a ray $l(w,\theta)$ to intersect the region C the following system of equations must have a solution in $x,\ y$ and z.

$$\begin{aligned} (x-p)^2 + (y-q)^2 + (z-r)^2 &= R^2, \\ \frac{x-w_1}{\theta_1} = \frac{x-w_2}{\theta_2} &= \frac{x-w_3}{\theta_3}. \end{aligned}$$

Eliminating x and y by,

$$\begin{aligned} x &= w_1 + \frac{\theta_1}{\theta_3}(z-w_3), \\ y &= w_2 + \frac{\theta_2}{\theta_3}(z-w_3), \end{aligned}$$

we get,

$$\left[w_1 + \frac{\theta_1}{\theta_3}(z-w_3) - p\right]^2 + \left[w_2 + \frac{\theta_2}{\theta_3}(z-w_3) - q\right]^2 + (z-r)^2 = R^2,$$

which simplifies to,

$$\left[\frac{\theta_1^2}{\theta_3^2} + \frac{\theta_2^2}{\theta_3^2} + 1\right] z^2 + \left[-2\frac{\theta_1}{\theta_3}w_3 + 2\frac{\theta_1}{\theta_3}(w_1-p) - 2\frac{\theta_2}{\theta_3}w_3 + 2\frac{\theta_2}{\theta_3}(w_2-q) - 2r\right] z +$$
$$\left[(w_1-p)^2 + \frac{\theta_1^2}{\theta_3^2}w_3^2 - 2\frac{\theta_1}{\theta_3}w_3(w_1-p) + (w_2-q)^2 + \frac{\theta_2^2}{\theta_3^2}w_3^2 - 2\frac{\theta_2}{\theta_3}w_3(w_2-q) + r^2 - R^2\right] = 0.$$

Hence the condition for the ray $l(w,\theta)$ to intersect C is $Q(w,\theta) \geq 0$ where Q has the following expression,

$$\left[-2\frac{\theta_1}{\theta_3}w_3 + 2\frac{\theta_1}{\theta_3}(w_1-p) - 2\frac{\theta_2}{\theta_3}w_3 + 2\frac{\theta_2}{\theta_3}(w_2-q) - 2r\right]^2 - 4\left[\frac{\theta_1^2}{\theta_3^2} + \frac{\theta_2^2}{\theta_3^2} + 1\right]$$
$$\left[(w_1-p)^2 + \frac{\theta_1^2}{\theta_3^2}w_3^2 - 2\frac{\theta_1}{\theta_3}w_3(w_1-p) + (w_2-q)^2 + \frac{\theta_2^2}{\theta_3^2}w_3^2 \right.$$
$$\left. -2\frac{\theta_2}{\theta_3}w_3(w_2-q) + r^2 - R^2\right]. \tag{5.9}$$

All collimation variants mentioned for the 2D case such as tapered collimation or smoothed collimation can be applied here.

As expected the standard reconstruction given by the inversion formula (5.7) for collimated acquisition fails. It creates several artifacts and is inaccurate. Hence we introduce the Searchlight CT reconstruction algorithm to overcome these problems.

5.5 3D Reconstruction Algorithm for Collimated Data

For 3D collimated data the reconstruction algorithm is essentially the same as in the 2D case. As before we introduce the regularization operator in 3D. One of our basic examples of regularization operator is the following. We partition the complement of the region of interest C into subsets $\{Q_j\}$, each one of fixed volume $\mathrm{vol}(Q_j) = v$,

and perform local averages. The regularization operator σ is given by:

$$\sigma F(x,y,z) = \begin{cases} F(x,y,z) & (x,y,z) \in C \\ \tau(F,Q_j) & (x,y,z) \in Q_j \end{cases}, \tag{5.10}$$

where $\tau(F,Q_j) = \frac{1}{v} \iiint_{Q_j} F(x,y,z)dxdydz$.

Note that we require $\sigma^2 = \sigma$. Several other regularization operators will be discussed in Chapter 8.

In view of the definition (5.8), we denote the set of rays where the X-ray Transform is uncensored as $T \subset V(\mathbb{R}^3)$ and the complement of T as $U = V(\mathbb{R}^3) \setminus T$.

$$T = \{(w,\theta) : l(w,\theta) \bigcap C \neq \emptyset\}.$$

Our reconstruction is initialized by setting $G = \tilde{X}F = 1_T.XF$, where F is the unknown density function and the dot denotes point-wise multiplication, and by computing the initial approximation of F as $f_0 = X^{-1}G$. Note that G is exactly the collimated X-ray Transform of F. The subsequent approximations f_n, $n \geq 1$, of F are obtained through the following iterative procedure.

1. Compute σf_n as in (5.10).

2. Compute $X\sigma f_n$, the standard X-ray Transform of σf_n, using (5.1). By projecting the data into the complementary sets T and U, write

$$X\sigma f_n = 1_T.X\sigma f_n + 1_U.X\sigma f_n.$$

3. Replace $1_T.X\sigma f_n$ by the known data $G = 1_T.XF$ in the preceding formula to define $Y_n = G + 1_U.X\sigma f_n$.

4. Compute f_{n+1} by applying the X-ray inversion formula (5.7) to Y_n. Hence,

$$f_{n+1} = X^{-1}Y_n = X^{-1}[G + 1_U.X\sigma f_n]. \tag{5.11}$$

As mentioned under mild assumptions and if the ROI-radius is greater than a critical radius, the sequence of functions f_n converges to the unknown density function σF inside the region of interest C. The same convergence argument as Section 3.1 is valid here as it was independent of dimension and acquisition method.

5.6 Numerical Analysis of Convergence through Spectral Radius

Recall that the convergence of the Searchlight CT iteration depended on the matrix M of the operator $\sigma X^{-1}1_U X\sigma$.

A detailed numerical analysis for the eigenvalues and eigenvectors of the matrix M was carried out in 2D (see Chapter 3) as in 3D the computations become very expensive. However we can do a very simple test to ascertain that the Searchlight CT algorithm will converge in 3D. Instead of computing all the eigenvalues of M, we just need to compute its spectral radius, $\rho(M)$. We study the 3D spherical acquisition case here and and we will present a similar study for the collimated spiral acquisition is Chapter 10.

We will consider a fairly small 3D object Ω included in a cubic box B of 32^3 voxels. The density function $F : \Omega \longrightarrow \mathbb{R}$ has its support Ω included in the box

B. This implies that our unknown data, namely F, can be viewed as a 3D image and hence as a vector in $\mathbb{R}^{32768}$. We consider the standard basis in this space, i.e. E_{ijk} is the matrix with 1 at the (i, j, k)-th position and zeros everywhere else. We consider regions of interest with radii between 3 and 9 voxels and report the spectral radius for the operator $M = \sigma X^{-1} 1_U X \sigma$ in Table 5.1, with X being the 3D X-ray Transform through spherical acquisition.

Table 5.1: Spectral Radius $\rho(M)$ of M for ROI's of various ROI-radii (with 3D spherical acquisition)

ROI-radius	3 voxels	5 voxels	6 voxels	7 voxels	9 voxels	11 voxels
$\rho(\mathbf{M})$	10.41	9.22	4.53	0.89	0.72	0.65

We observe that for an ROI radius higher than 7 voxels convergence occurs. Also notice that as for the 2D case this condition on spectral radius is independent of the data and just depends on the data size, the ROI and the techniques of acquisition, inversion and regularization. Hence the theorem 3.2.3 can be restated for the 3D case as:

Theorem 5.6.1. *Let $F : \mathbb{R}^3 \longrightarrow \mathbb{R}$ be a Lebesgue integrable function with compact support Ω. For a given 3D acquisition geometry let X be the X-ray Transform (on a set of rays V) and X^{-1} be its corresponding inverse. Let σ be a regularization operator such that $\sigma^2 = \sigma$. For a region of interest $C \subset \Omega$ let $T \subset V$ be the set of rays which pass through C and $U = V \setminus T$. Set $G = 1_T.XF$ and $f_0 = X^{-1}G$. Then sequence of iterates given by,*

$$f_{n+1} = A + Mf_n$$

with $A = X^{-1}G$ *and* $M = \sigma X^{-1} 1_U X \sigma$*, converges to* σF *within* C *if and only if the spectral radius* $\rho(M) < 1$.

In this chapter we have used the data acquisition geometry to be spherical acquisition and the set V of rays on which we require the X-ray Transform is described in 6.1.1.

CHAPTER 6

Numerical Implementation for Reconstruction of 3D Collimated Data with Spherical Acquisition

In 2D the numerical implementation in 2D reconstruction algorithm was simple, efficient, and followed from definitions. A similar approach in 3D leads to unacceptable computational time. Hence there is a need to devise fast implementation strategies to speed up the acquisition and inversion process. Due to certain aspects of the 3D case minor modifications are also required in the algorithm to avoid numerical errors in the implementation. We will consider these numerical implementation aspects in this chapter.

6.1 Implementation of Simulated Data Acquisition in 3D

Simulating data acquisition to compute numerically the X-ray Transform requires sophisticated implementation to reach acceptable CPU times. We introduce a simulated acquisition technique based on the Fourier Slice Theorem. This technique is independent of the mode of acquisition.

6.1.1 Spherical Acquisition

To describe the full set of rays required for spherical acquisition let the source points on a sphere of radius D be denoted by

$$W = \{(D\cos\alpha\sin\beta,\ D\sin\alpha,\sin\beta,\ D\cos\beta) : \alpha \in [0, 2\pi),\ \beta \in [0, \pi)\}. \tag{6.1}$$

Note that α and β will be discretized. Recall that for a ray $l(w, \theta)$ the unit vector specifies the direction. The range of the values for θ depend upon the support Ω of the density function, F. The set of ray directions Θ is specified by,

$$\Theta = \left\{ \frac{(x - w_1, y - w_2, z - w_3)}{\|(x - w_1, y - w_2, z - w_3)\|} : (w_1, w_2, w_3) \in W,\ (x, y, z) \in P \right\}. \tag{6.2}$$

So the set of rays required for spherical acquisition is,

$$\{(w, \theta) : w \in W,\ \theta \in \Theta\}. \tag{6.3}$$

Note that W is discretized as well as Ω, which implies Θ is discretized. The X-ray Transform along these rays an be calculated by as follows.

6.1.2 The Implementation

Recall that by the Fourier Slice Theorem (5.3), if $\hat{F}$ is the 3D Fourier Transform of F, we have

$$\widehat{XF^{\theta}}(\xi) = \widehat{F}(\xi),$$

which gives,

$$XF(w,\theta) = \int_{h(\theta)} \hat{F}(\xi) e^{i\langle \xi, w\rangle} d\xi, \tag{6.4}$$

where $h(\theta)$ is a plane orthogonal to θ.

Practically this requires first to compute the 3D Fourier Transform of F. For every unit vector θ we need to select a plane $h(\theta)$ passing through the origin and orthogonal to θ. We compute the 2D Inverse Fourier Transform on these planes. We will describe this set of planes as follows.

Consider a unit vector Φ in the xz-plane, making an angle ϕ with the x-axis. The angle ϕ defines a rotation around the $y-$axis. Another unit vector Ψ in the xy-plane, at an angle of ψ with the x-axis defines a rotation about the z-axis. There exists a unique plane containing the pair of unit vectors (Φ, Ψ). By varying the angles ϕ and ψ we obtain a family of planes. In fact given any direction θ we can find a plane characterized by (Φ, Ψ), which is perpendicular to it. Such a plane is denoted by $P(\phi, \psi)$. Due to redundancy it is enough to consider $\phi \in [0, 2\pi]$ and $\psi \in [0, \pi]$. A visual idea of these planes is given in Figure 6.1 and Figure 6.2.

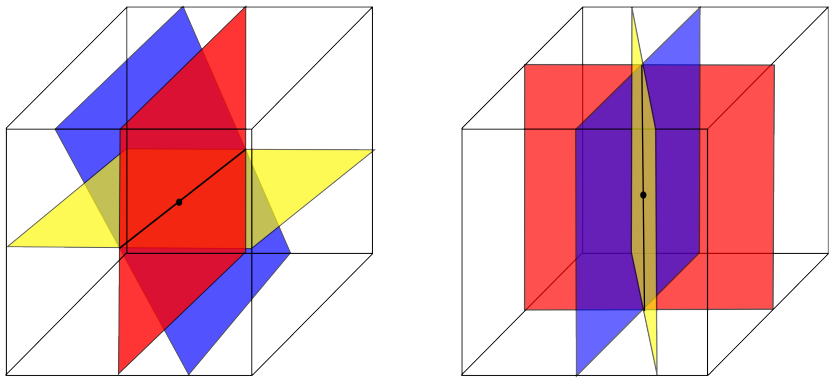

Figure 6.1: Special cases of the planes characterized by (ϕ, ψ) (a) Planes corresponding to $\psi = 0$ (b) Planes corresponding to $\phi = 0$

We have used a discretization of 2° for both ϕ and ψ. So the set Π of discretized pairs (ϕ, ψ) is

$$\Pi = \{(\phi_i, \psi_j) : i = 2, 4, \ldots 360 \text{ and } j = 2, 4, \ldots 180\},$$

The steps for data acquisition by the Fourier Slice theorem using this enumeration for the planes are listed below.

1. Compute $\hat{F}$, the 3D Fourier Transform of F.
2. Choose $(\phi_i, \psi_j) \in \Pi$.
3. Denote (ϕ_i, ψ_j) by (ϕ, ψ).
4. Restrict $\hat{F}$ to the plane $P(\phi, \psi)$. Call the restriction of $\hat{F}$ to $P(\phi, \psi)$ as $\hat{F}_{\phi,\psi}$.
5. Compute the 2D Inverse Fourier Transform of $\hat{F}_{\phi,\psi}$ and store the result.
6. Return to Step 2 until the whole of Π has been exhausted.

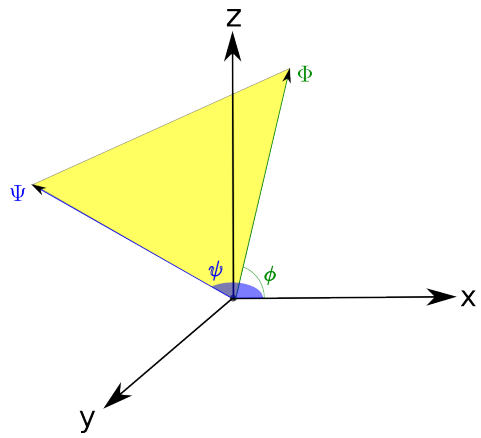

Figure 6.2: A portion of a general plane $P(\phi, \psi)$ characterized by the unit vectors Φ and Ψ

Note that we have obtained XF in terms of ϕ, ψ and the planar coordinates of each plane. We will reconvert to our original coordinates in terms of w and θ in the next subsection.

6.1.3 Conversion of Data to Original Coordinates

Let the coordinate system on a plane $P(\phi, \psi)$ be given by two orthogonal vectors W_1 and W_2. Hence we have the X-ray Transform data in terms of W_1, W_2, ϕ and ψ. We choose W_1 to be along the direction on Φ and W_2 in an orthogonal direction on $P(\phi, \psi)$. We need to reorder this in terms of our original coordinates w and θ. Let $w = (w_1, w_2, w_3)$ and $\theta = (\theta_1, \theta_2, \theta_3)$ with $\|\theta\|_2 = 1$. The positions of the original and the new coordinates are shown in Figure 6.3.

By definition $\Phi = (\cos\phi, 0, \sin\phi)$ and $\Psi = (\cos\psi, \sin\psi, 0)$. The normal to the plane $P(\phi, \psi)$ is then given by $\Phi \times \Psi$. Hence the unit normal is $\frac{\Phi \times \Psi}{\|\Phi \times \Psi\|}$. We also know

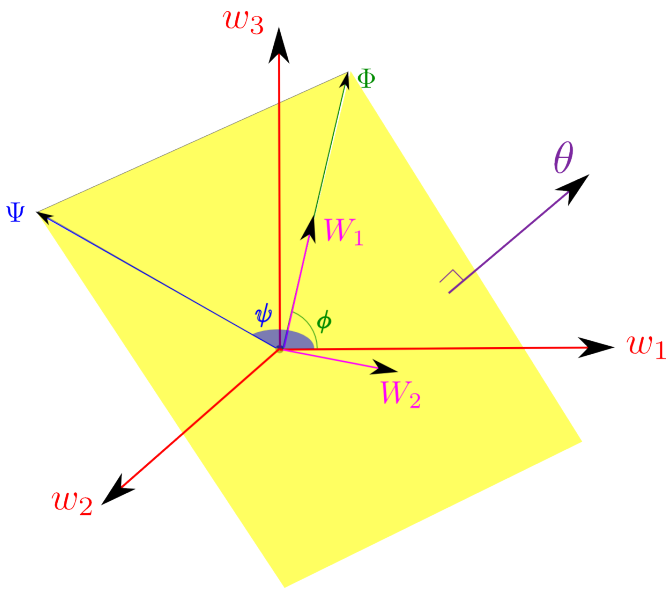

Figure 6.3: Position of the coordinate systems (w, θ) and (W_1, W_2, ϕ, ψ) used in converting from one system to the other

that θ is the unit normal. Equating the two we get,

$$\theta_1 = \frac{-\sin\phi\sin\psi}{\sqrt{\sin^2\phi + \cos^{\phi}\sin^2\psi}}, \tag{6.5a}$$

$$\theta_2 = \frac{\cos\psi\sin\phi}{\sqrt{\sin^2\phi + \cos^{\phi}\sin^2\psi}}, \tag{6.5b}$$

$$\theta_3 = \frac{\cos\phi\sin\psi}{\sqrt{\sin^2\phi + \cos^{\phi}\sin^2\psi}}. \tag{6.5c}$$

Without losing generality we can assume the point w to lie on the plane $P(\phi, \psi)$ orthogonal to θ. From the position of Φ we have,

$$w_1 = W_1\cos\phi, \tag{6.6a}$$

$$w_3 = W_1\sin\phi. \tag{6.6b}$$

Finally since w lies on the plane $P(\phi, \psi)$, (w_1, w_2, w_3) satisfy its equation $\theta_1 x + \theta_2 y + \theta_3 z = 0$. So,

$$w_2 = \frac{-\theta_1 w_1 - \theta_3 w_3}{\theta_2}. \tag{6.6c}$$

Hence we now have the data in terms of w and θ.

Remarks 6.1.1. It must be noted that:

1. For a particular type of acquisition we just need to identify the set of rays required for reconstruction and then apply the method as done for spherical acquisition in Section 6.1.1.

2. For the implementation of collimated acquisition, for any (W_1, W_2, ϕ, ψ) as described in Section 6.1.2, compute the corresponding values of w and θ using Section 6.1.3. Then check if $Q(w, \theta) \geq 0$ (Section 5.9). If so then $\tilde{X}F(w, \theta) = XF(w, \theta)$ otherwise set $\tilde{X}F(w, \theta) = 0$.

6.2 Numerical Implementation for Inverse X-ray Transform

Since we employed a specific technique to implement the X-ray Transform we need a corresponding technique to implement $X^{-1}G$ for a function G on the set of rays $V(\mathbb{R}^3)$. The steps for inversion follow exactly by reversing the steps for the acquisition. The details are not provided but the steps are briefly summarized.

Recall the set Π of discretized pairs (ϕ, ψ),

$$\Pi = \{(\phi_i, \psi_j) : i = 2, 4, \ldots 360 \text{ and } j = 2, 4, \ldots 180\}.$$

Also recall that during the implementation of the acquisition the data had been stored in an enumeration of (ϕ, ψ) corresponding to the plane $P(\phi, \psi)$. The steps for the inversion are as follows.

1. Choose $(\phi_i, \psi_j) \in \Pi$. Denote (ϕ_i, ψ_j) by (ϕ, ψ).
2. $G_{\phi,\psi}$ is the acquired data corresponding to the plane $P(\phi, \psi)$.
3. Compute the 2D Fourier Transform $\widehat{G_{\phi,\psi}}$ of $G_{\phi,\psi}$ on the plane $P(\phi, \psi)$.
4. $\widehat{G_{\phi,\psi}}$ corresponds to the 3D Fourier Transform of $X^{-1}G$ restricted to the plane $P(\phi, \psi)$.
5. Return to Step 1 until the whole of Π has been exhausted.
6. Let $\hat{H}$ be the collection of $\widehat{G_{\phi,\psi}}$ for all $(\phi, \psi) \in \Pi$. Interpolate $\hat{H}$ on 3D rectangular coordinates by using the weighted average of the 4 nearest neighbors.
7. Compute the 3D Inverse Fourier Transform of $\hat{H}$ to obtain the reconstructed function H.

The implementation of both the acquisition and the inversion are computationally faster than direct techniques. For a cubical data of size 257 acquisition took about 6 minutes while inversion took about 3 minutes. The computations by applying the direct formulae were also tested but computation time ran into several hours.

6.3 Boundary Smoothing

There are certain aspects of our algorithm which we need to modify for the 3D case. We have already described the alternative technique for the data acquisition and inversion which were primarily adopted for computational feasibility. Here we describe another such modification.

We are using the Fourier Transform in our algorithm for both acquisition and inversion. The density function F is defined only on a compactly supported set Ω but the calculation of the Fourier Transform for points within Ω will require values of the function for points outside of Ω. In such cases during the implementation of the Fourier Transform its periodic extension is used. This means that the function is extended periodically outside its support. The periodic extension may cause jump discontinuities.

The effect of these discontinuities is more pronounced in the 3D case than in 2D. Hence we smooth along the boundaries (faces, edges and corners) to reduce the jump discontinuities. This step takes place right after every inversion (Step 4 of the algorithm).

We describe this procedure in discretized coordinates. Assume that the support Ω of F is included in a cubical voxel grid box $B = \{(x, y, z) : x, y, z = 1, 2, \dots L\}$. The smoothing has to be carried out along faces, edges and corners of B. Due to their relative large size the we do a multi-step smoothing on the faces while on the edges and corners a single step is enough. We start by defining smoothing on the faces. This needs to be done along all three coordinates. Consider the $x-$coordinate,

i.e the faces of the box B which are parallel to the yz-coordinate plane. Define,

$$S_x F(x,y,z) = \begin{cases} \frac{1}{2}(F(L-1,y,z) + F(1,y,z)) & x = L \\ \frac{1}{2}(F(L-2,y,z) + F(L,y,z)) & x = L-1 \\ \frac{1}{2}(F(L,y,z) + F(2,y,z)) & x = 1 \\ \frac{1}{2}(F(L-3,y,z) + F(L-1,y,z)) & x = L-2 \\ \frac{1}{2}(F(1,y,z) + F(3,y,z)) & x = 2 \\ F(x,y,z) & otherwise \end{cases} \tag{6.7a}$$

Note that the operations must be carried out in the given order. Similarly we can define S_y and S_z for smoothing along the other faces. Hence the resultant operator for smoothing along the faces is $S_{fac} = S_z S_y S_x$. Next we need to smooth along the edges. Let $K = \{1, L\}^2$. Define,

$$S_{xy} F(x,y,z) = \begin{cases} \frac{1}{4} \sum_{(x,y) \in K} F(x,y,z) & (x,y) \in K \\ F(x,y,z) & (x,y) \notin K \end{cases}. \tag{6.7b}$$

Similarly define S_{yz} and S_{zx} for smoothing along other edges. The resultant operator for smoothing along edges is $S_e dg = S_{zx} S_{yz} S_{xy}$. Lastly we smooth at the corners. Let $J = \{1, L\}^3$. Define,

$$S_{xyz} F(x,y,z) = \begin{cases} \frac{1}{8} \sum_{(x,y,z) \in J} F(x,y,z) & (x,y,z) \in J \\ F(x,y,z) & (x,y,z) \notin J \end{cases}. \tag{6.7c}$$

Thus the operator to smooth along corners is $S_{cor} = S_{xyz}$. Combining the above steps we get the boundary smoothing operator S_B.

$$\begin{aligned} S_B F &= (S_{cor} S_{edg} S_{fac}) F \\ &= (S_{xyz} S_{zx} S_{yz} S_{xy} S_z S_y S_x) F. \end{aligned} \tag{6.7d}$$

CHAPTER 7

Numerical Results for Reconstruction of 3D Collimated Data with Spherical Acquisition

We present a detailed analysis for the performance of the our reconstruction algorithm for 3D collimated data. Some of the performance measures mentioned in Chapter 2 like **Relative Reconstruction Error** and **Radiation Exposure**. We restate them here for the 3D case. The basic properties assumed for F remain the same. F is a density function with compact support Ω and is Lebesgue integrable. The density functions we use for our experiments are all bounded.

Definition 7.0.1. *Let F be the density function in $\mathbb{R}^3$ to be reconstructed and F_{rec}*

*be a reconstruction of F. The **Relative Reconstruction Error**, Rel is defined by,*

$$Rel = \sum_{v \in C} \frac{\|F(v) - F_{rec}(v)\|}{\|F(v)\|}, \tag{7.1}$$

where C is a spherical region of interest in the support Ω of F.

Definition 7.0.2. *The radiation dose $\delta(v)$ received by a voxel v is defined as the number of rays passing through v. Let $c = \sum_{v \in I^3} \delta(v)$ be the sum of received doses over all pixels, in the case of collimated irradiation, and m be the maximal dose which is received in the uncollimated case. We define the **Radiation Exposure** E, as*

$$E = \frac{c}{m}. \tag{7.2}$$

Another measure for accuracy used in the industry is the **Peak Signal to Noise Ratio** or **PSNR**.

Definition 7.0.3. *Let F be a function and F_{rec} be its reconstruction with Relative Reconstruction Error* **Rel**. *Then the $PSNR$ is defined as,*

$$PSNR = 20 \log_{10} \left(\frac{\max(F)}{Rel} \right). \tag{7.3}$$

The discretization of the coordinates is also the direct extension of the 2D case. In particular, the regularization operator σ averages over $2 \times 2 \times 2$ cubes which are precisely the sets Q_j described in (5.10). Coordnitewise this can be described by defining for a coordinate $(x, y, z) \in Q_j \subset I^3$, the function τ (as in Section 5.10),

$$\tau(F(x, y, z)) = \frac{1}{8} \sum_{(\tilde{x}, \tilde{y}, \tilde{z}) \in Q_j} F(\tilde{x}, \tilde{y}, \tilde{z}).$$

7.1 Relative Density and Convergence Criterion

In Chapter 3 we have outlined the condition on the ROI-radius which ensures convergence of the Searchlight CT Algorithm in the region of interest C. We require the norm of the density function outside C to be small enough. To get an accurate numerical evaluation of this aspect we introduce the concept of **Relative Density**.

Definition 7.1.1. *The Relative Density, D of a region C is defined as the ratio between the sum of densities over voxels on C and the sum of densities over all voxels, i.e.*

$$D(C,F) = \frac{\sum_{v\in C} F(v)}{\sum_{v\in\Omega} F(v)}. \tag{7.4}$$

We will seek a critical threshold value α of $D(C,F)$ such that we have accurate reconstruction for an ROI C if and only if $D(C,F) > \alpha$. α depends on the nature of the unknown density function F. Naturally requiring $D(C,F) > \alpha$ will be roughly equivalent to require the radius of C to be larger than a fixed critical radius.

A few aspects of $D(C,F)$ must be studied in order to get a better idea about the convergence condition. First for a spherical region C with fixed radius but variable center the variation in D must be noted. Next with these different centers the least value α for convergence must be studied and the radii at which $D = \alpha$ is attained should be noted. These aspects will be considered for two examples of density functions in 3D namely the Shepp Logan phantom and a biological data set of mouse tissue.

In the next chapter we will study the critical density ratio α for the same region

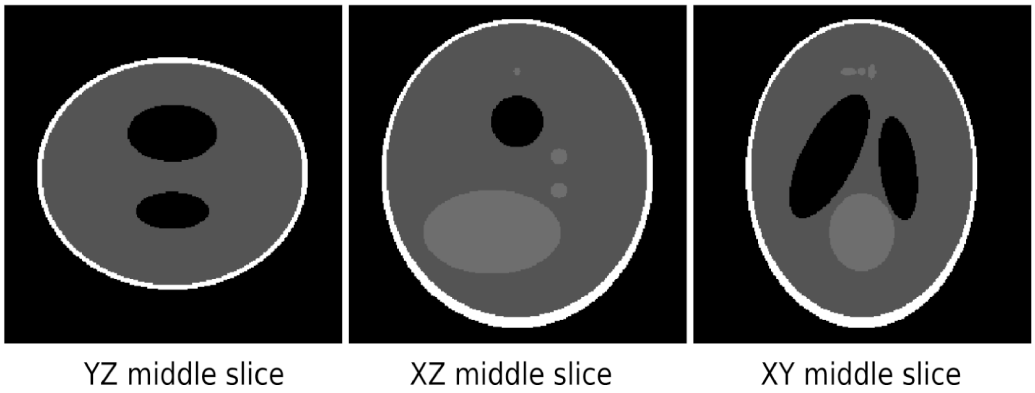

Figure 7.1: The 3 middle slices of the 3D Shepp-Logan phantom

but for different regularization operators.

7.2 Reconstruction Tests on the 3D Shepp-Logan Phantom

We start the numerical demonstrations with the 3D Shepp-Logan phantom whose three middle slices are shown in Figure 7.1. The phantom is discretized on a cubic voxel grid of size 257^3.

We select multiple spherical regions of interest, C within this phantom and carry out reconstruction tests on C. The intersection of C with three middle slices orthogonal to the coordinate axes is shown in Figure 7.2.

As expected the standard reconstruction on collimated data fails to be accurate when applied. Several artifacts and false edges are created as seen in resulting reconstruction as seen in Figure 7.3. When we apply the Searchlight CT Algorithm,

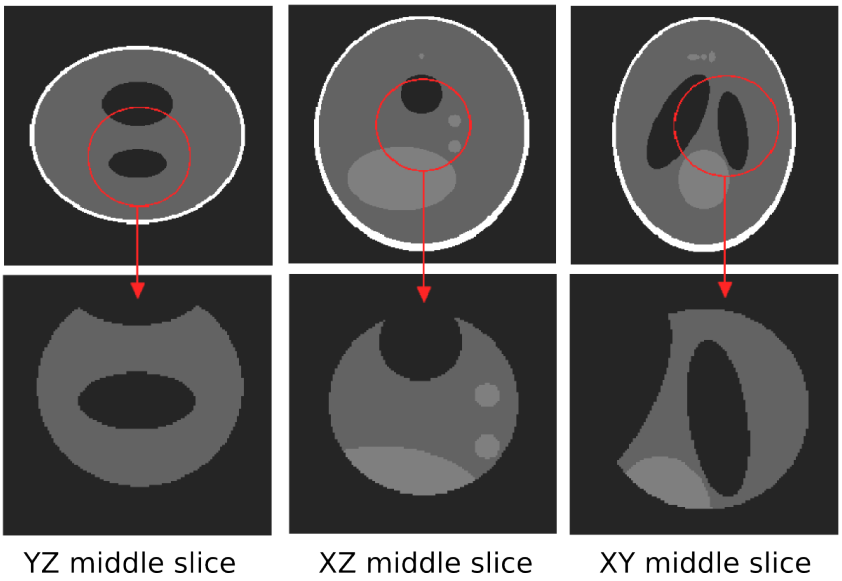

Figure 7.2: Position of the region C in the 3 middle slices of the Shepp-Logan phantom with their magnified views given below

the results are far superior (Figure 7.4). A comparison of the two methods (for the XZ middle slices) along with the ground truth is shown is Figure 7.5.

Though the difference in reconstruction quality is evident in the figures, we will quantify the gains in reconstruction accuracy by the four performance characteristics Rel, E, D, and $PSNR$. These were defined at the beginning of the chapter. Table 7.1 lists the performance of the Searchlight CT algorithm in terms of these reconstruction performance characteristics for multiple ROI radii between 45 and 90 voxels.

Numerical tests show that for accurate reconstruction, the relative density $D(C, F)$ should be larger than $D > 2.5\%$. This corresponds to a an ROI-radius of approximately 40 voxels below which reconstruction fails. To test the variability of $D(C, F)$

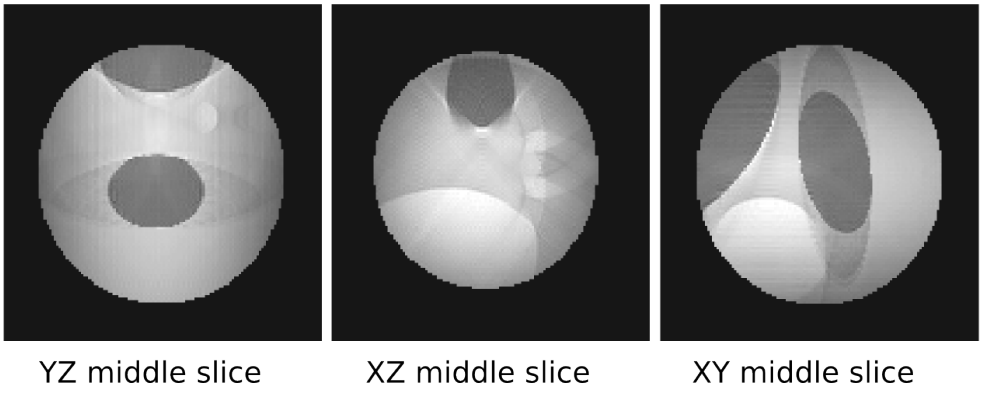

Figure 7.3: Collimated Reconstruction: The 3 middle slices of the Standard reconstruction of the region C (using the filtered back-projection)

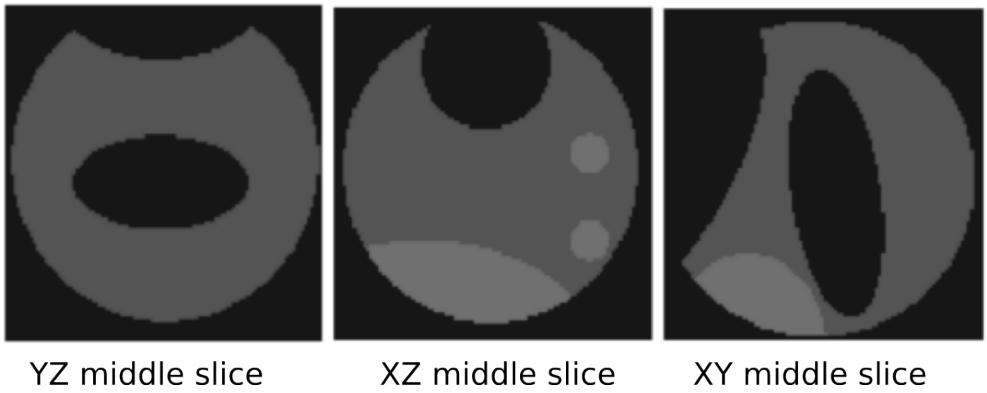

Figure 7.4: Collimated Reconstruction: The 3 middle slices of the reconstruction by Searchlight CT of the region C

with the position of C in the phantom, we divided the phantom into $3^3 = 27$ sub-cubes and studied the 27 potential positions of C the ROI within each sub-cube. Since the Shepp-Logan phantom is dense at the center and sparse away from it, $D(C, F)$ is significantly higher near the center. This is shown in Figure 7.11. However this doesn't affect the critical threshold for $D(C, F)$ for convergence. We still require $D(C, F) > 2.5\%$ though this critical threshold might be attained at varying ROI-radii.

(a) Standard Reconstruction (b) Searchlight CT (c) Ground Truth

Figure 7.5: Comparison of Reconstruction methods for the region C in the Shepp-Logan phantom with representative 2D slices shown: (a) Standard Reconstruction (b) Reconstruction through Searchlight CT (c) Ground Truth

Table 7.1: Performance for various ROI-radii (Shepp-Logan phantom)

ROI-radius	$D(C,F)$	E	Rel	$PSNR$
45 voxels	3.8 %	19 %	10.3 %	58.9 dB
60 voxels	8.5 %	31 %	8.6 %	62.2 dB
75 voxels	15.3 %	44 %	7.6 %	63.4 dB
90 voxels	23.8 %	57 %	7.2 %	64.0 dB

As the ROI-radius increases the radiation exposure, E increases,(Figure 7.6) and relative reconstruction error decreases. The fact to be noted is that even as exposure decreases from 57% to 19%, the Relative Reconstruction Error increases quite moderately from 7.2% to 10.3%. This is of great importance in the medical industry. The mutual dependence between Relative Reconstruction Error and Radiation Exposure is seen in Figure 7.7.

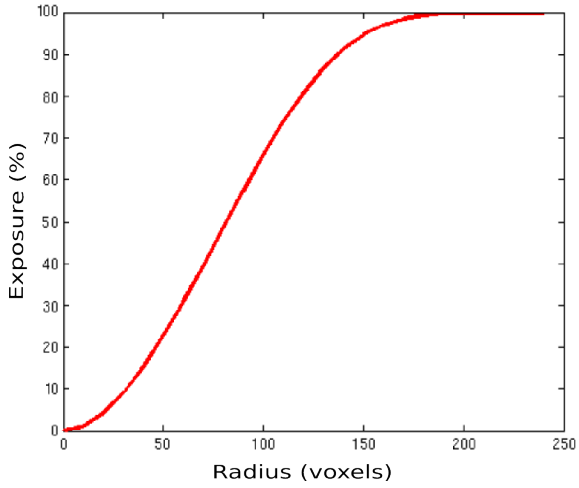

Figure 7.6: Variation of exposure, E (for collimated data) with the radius of the region of interest

7.3 Validation on Random Phantoms

We need to make sure that the convergence properties of our reconstruction algorithm are not dependent on the specific phantom. Hence we create a "phantom generator" to generate random spherical head phantoms of random sizes. The generation steps are described briefly as follows.

1. Choose a size L. Create a null 3D phantom with zero densities.

2. Create an outer sphere S_1 with highest density 1.0 inside, which is centered at $(\frac{L+1}{2}, \frac{L+1}{2}, \frac{L+1}{2})$ and has radius $0.45L$.

3. Create an inner sphere S_2 with low density 0.1 inside, which is centered at $(\frac{L+1}{2}, \frac{L+1}{2}, \frac{L+1}{2})$ and has radius $0.43L$. Thus the difference $S_1 \setminus S_2$ has the highest density and represents the skull.

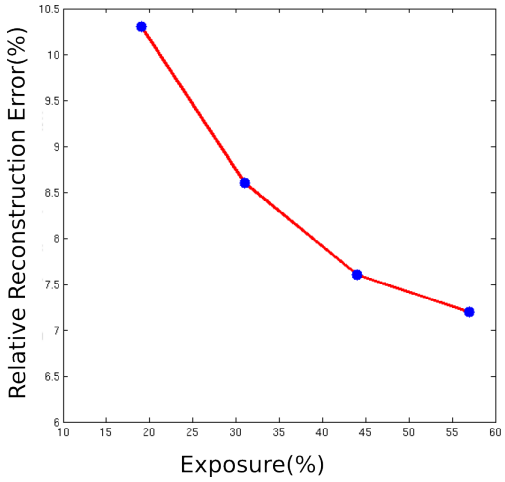

Figure 7.7: Relationship between exposure, E and Relative Reconstruction Error Rel for a regions of interest with same center

4. Create a small sphere s_1 inside S_2 with random center and radius in the range $[0.1L,\ 0.2L]$. This sphere should have low-medium density (in $[0.2,\ 0.5]$) inside.

5. Create another small sphere s_2 inside S_2 with the same specifications as s_1 but it should not intersect s_1.

6. Create a tumor, T with high density 0.9 inside S_2 with random center and radius less than $0.1L$.

7. The region of interest, C is centered at the tumor T, and has radius equal to twice the tumor radius.

A typical cross sectional slice of such a randomly generated spherical head phantom is shown in Figure 7.8.

The performance of the Searchlight CT Algorithm for such a random phantom is tabulated in Table 7.2. The size of the phantom generated was 129 voxels. The

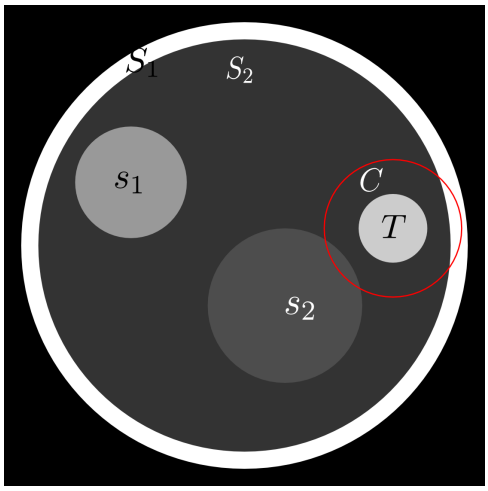

Figure 7.8: A Typical 2D slice in a random phantom created as described in Section 7.3

radius of the tumor was fixed at 11 voxels. Various cases for the position of the tumor were studied over randomly generated phantoms and we the algorithm was tested for a few radii of C between 20 and 30 voxels.

Table 7.2: Relative Reconstruction Error for various ROI-radii (Random phantom)

ROI-radius	Case 1	Case 2	Case 3	Case 4
20	10.8%	10.5%	11.4%	11.2%
25	9.3%	9.2%	9.8%	9.7%
30	8.1%	8.0%	8.6%	8.4%

7.4 Tests on Real Data

The final validation of our reconstruction algorithm is demonstrated on real biological data. Generally its more challenging to work with real data. Since we are studying spherical acquisition which is not used in practice for medical CT acquisition, we

could not directly work data acquired by collimated X-ray Transform. We start from 3D density data reconstructed classically from real uncollimated acquired data. On these density functions we simulate collimated spherical acquisition and we then apply our reconstruction algorithm.

The first data set we studied was reconstructed classically after the full body scan of a mouse. Its size was $512 \times 768 \times 512$. The middle slices of these mouse data are shown in Figure 7.9.

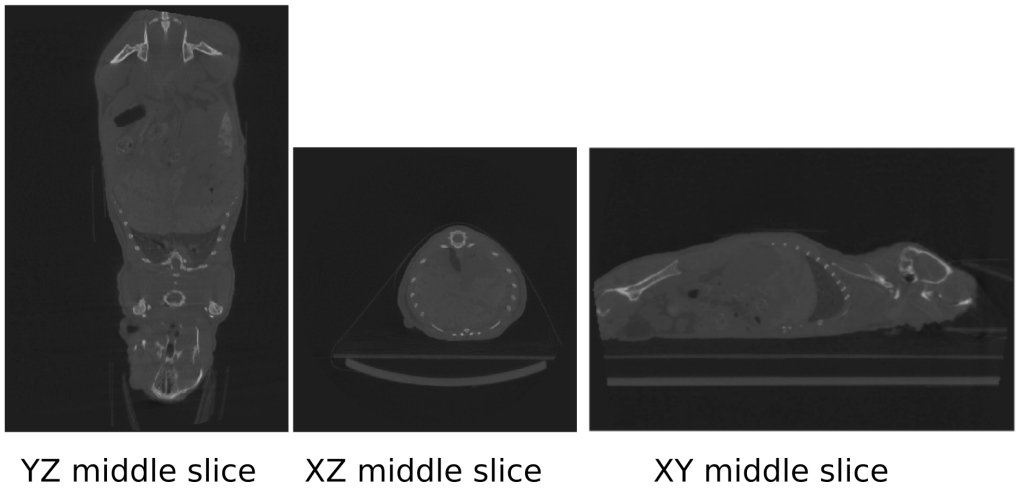

Figure 7.9: 2D views of the middle slices for the full body scan of a mouse

To carry out our tests we extracted a sub-cube Ω of these data (near the brain). The data size was 257^3. A small region of interest C was chosen in Ω and reconstruction by standard method and Searchlight CT was carried out on C after simulation of a collimated acquisition. A comparison of the two reconstruction techniques is shown in Figure 7.10 for the XZ middle slice. A summary of performance for various ROI-radii between 45 and 90 voxels is given in Table 7.3.

We noted that for accurate reconstruction one needs $D(C, F) > 2.8\%$ which

Table 7.3: Performance for various ROI-radii (Mouse Data)

ROI-radius	D	E	Rel	$PSNR$
45 voxels	4.0 %	19 %	10.8 %	53.1 dB
60 voxels	9.9 %	31 %	8.8 %	58.2 dB
75 voxels	20.7 %	44 %	7.9 %	60.7 dB
90 voxels	29.8 %	57 %	7.5 %	61.9 dB

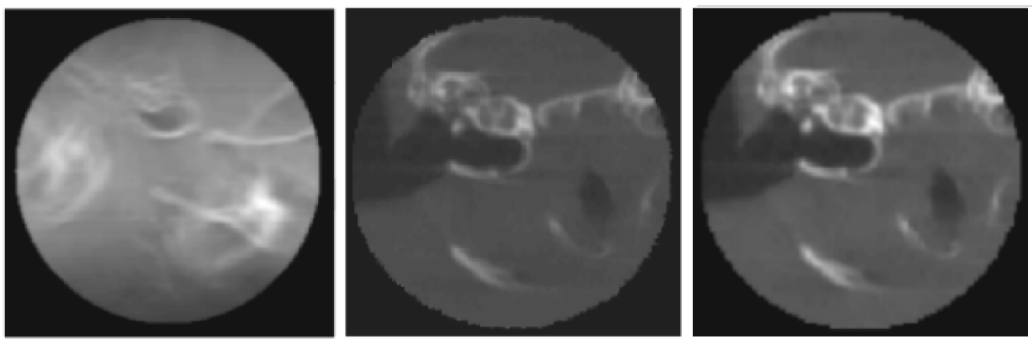

(a) Standard Reconstruction (b) Searchlight CT (c) Ground Truth

Figure 7.10: Comparison of Reconstruction methods for the region C in the mouse tissue data with representative 2D slices shown: (a) Standard Reconstruction (b) Reconstruction through Searchlight CT (c) Ground Truth

corresponded to a radius of about 40 voxels. At this radius the relative reconstruction error was 12%. Once again we checked the variance of D with position in a similar way to the Shepp-Logan phantom. Since these real data are more evenly distributed than the artificial phantom studied before, not much variation was observed between the values of $D(C, F)$ at different positions for a fixed radius of C. This is shown in Figure 7.11 The critical threshold α of $D(C, F)$ for convergence was also found to be approximately the same throughout the data.

From the important relationship between the Radiation Exposure, E and the Relative Reconstruction Error, Rel we see that a large reduction in exposure leads

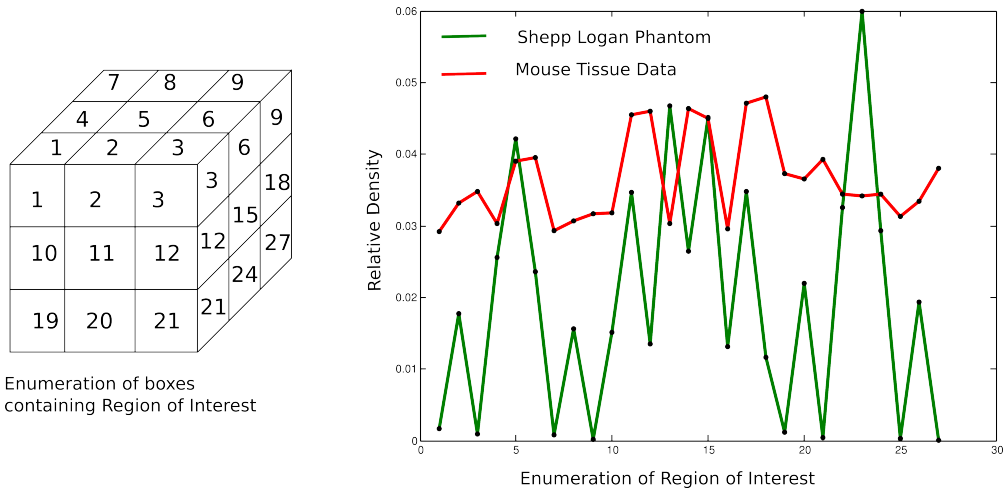

Figure 7.11: Variation of relative density with the position of the region C

to only a fairly small increase in relative reconstruction error. The graph of E vs Rel (7.12) is similar to the graph observed for the Shepp-Logan phantom.

The second biological data set we used was reconstructed classically from uncollimated data of a human jaw. This data set was of size $536 \times 536 \times 440$. The central slices of the data are shown in Figure 7.13.

Again we extract a sub-cube, Ω of size 257^3 select a region of interest C in Ω. A comparison of the standard reconstruction and Searchlight CT on C is shown in Figure 7.14 for the XY middle slice. A summary of performance for various ROI-radii between 45 and 90 voxels is given in Table 7.4.

Table 7.4: Performance for various ROI-radii (Jaw Data)

ROI-radius	D	E	Rel	$PSNR$
45 voxels	3.2 %	19 %	11.4 %	50.6 dB
60 voxels	9.1 %	31 %	9.6 %	55.3 dB
75 voxels	19.7 %	44 %	9.0 %	58.7 dB
90 voxels	28.5 %	57 %	8.2 %	59.9 dB

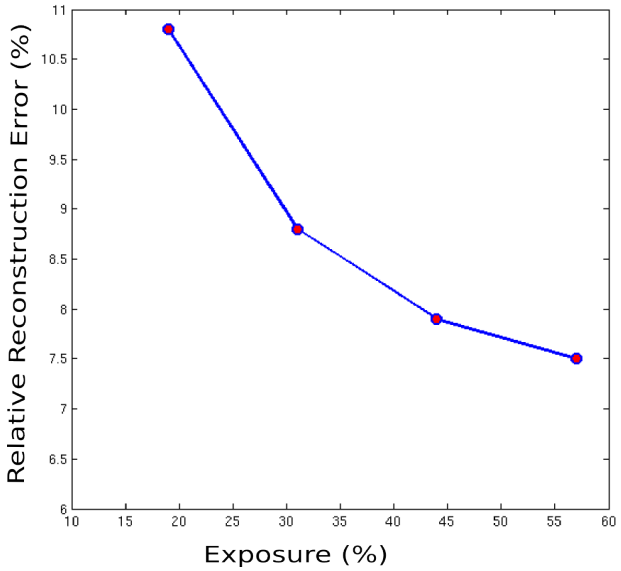

Figure 7.12: Relationship between exposure, E and Relative Reconstruction Error for a region C in the mouse data reconstructed through Searchlight CT

7.5 Analysis of the Reconstruction Error for Collimated Data

The Relative Reconstruction Error *Rel* provides a global measure of the error. However a closer look at the algorithm performance shows that the reconstruction error is strongly localized on discontinuity points of the density function F i.e. along the edges. Edges in an image can easily be detected by any simple gradient based edge detector, (see for example [34]).

This behavior is illustrated in Figure 7.15, where, for a representative 2D slice of the mouse data inside the region of interest C, the gradient of F and the voxels where the reconstruction error is large are displayed side by side.

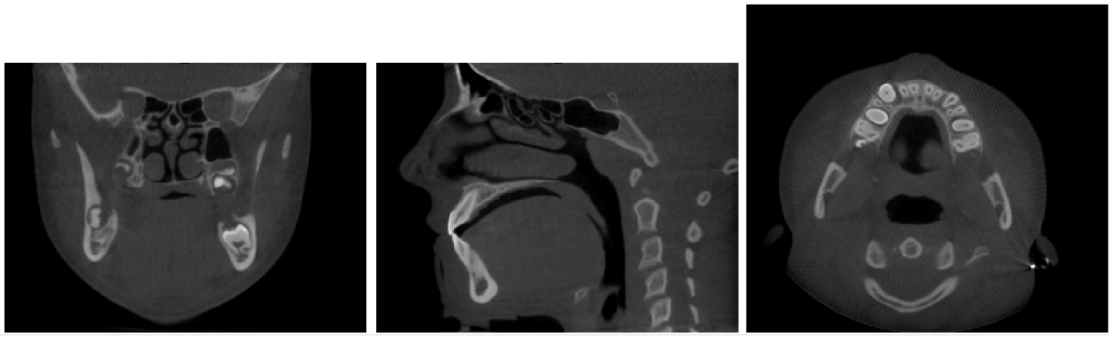

Figure 7.13: 2D views of the middle slices for the scan of a human jaw

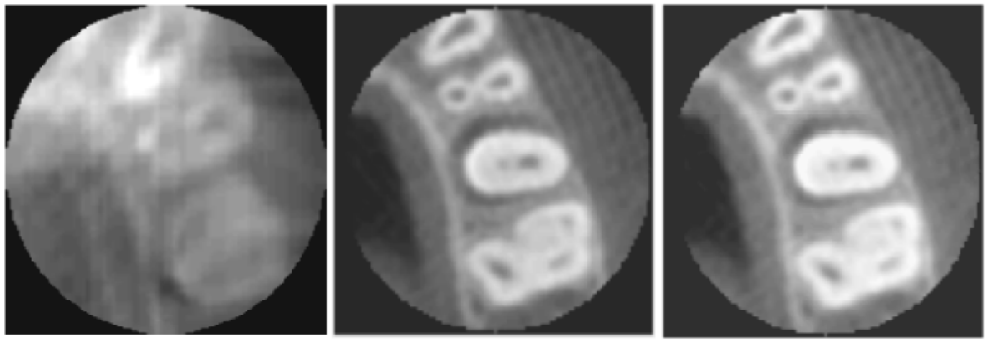

Figure 7.14: Comparison of Reconstruction methods for the region C in the mouse tissue data with representative 2D slices shown: (a) Standard Reconstruction (b) Reconstruction through Searchlight CT (c) Ground Truth

We compute the high gradient zone of the mouse data F as follows. At every voxel v compute the norm of the gradient $\|\nabla F(v)\|$. Calculate the 85th quantile q of these norms. The voxels for which $\|\nabla F(v)\| > q$ comprise the high gradient zone.

The correlation between edge locations and large-error points is confirmed by the comparison of histograms for distribution of errors over the whole ROI and for the the zone of high gradient, which is shown in Figure 7.16. Whereas over the whole of ROI the there is a strong difference between the number of high error and low error

points, this difference is far less pronounced in the high gradient zone.

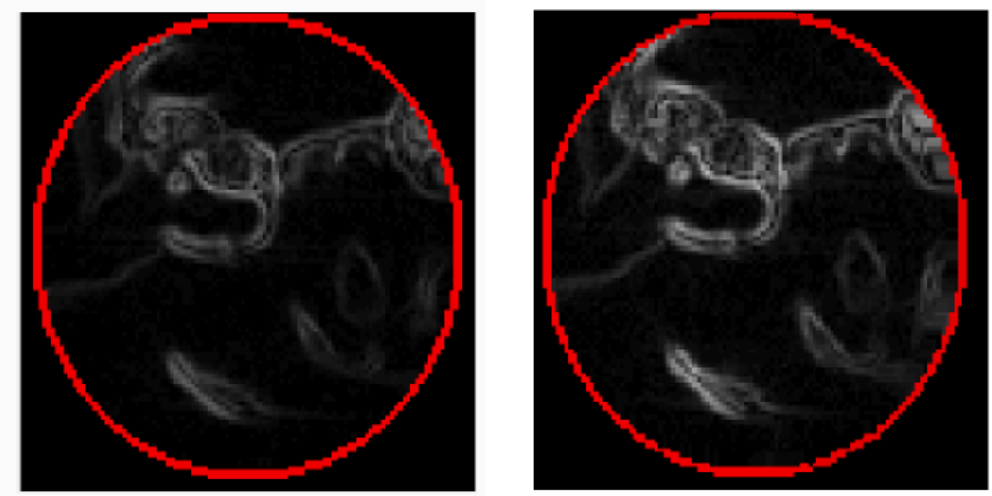

(a) High gradient zone (b) High error zone

Figure 7.15: Reconstruction of collimated mouse data: High correlation between the (a) High density gradient zone (edge locations) and (b) high error zone shown in a representative 2D slice

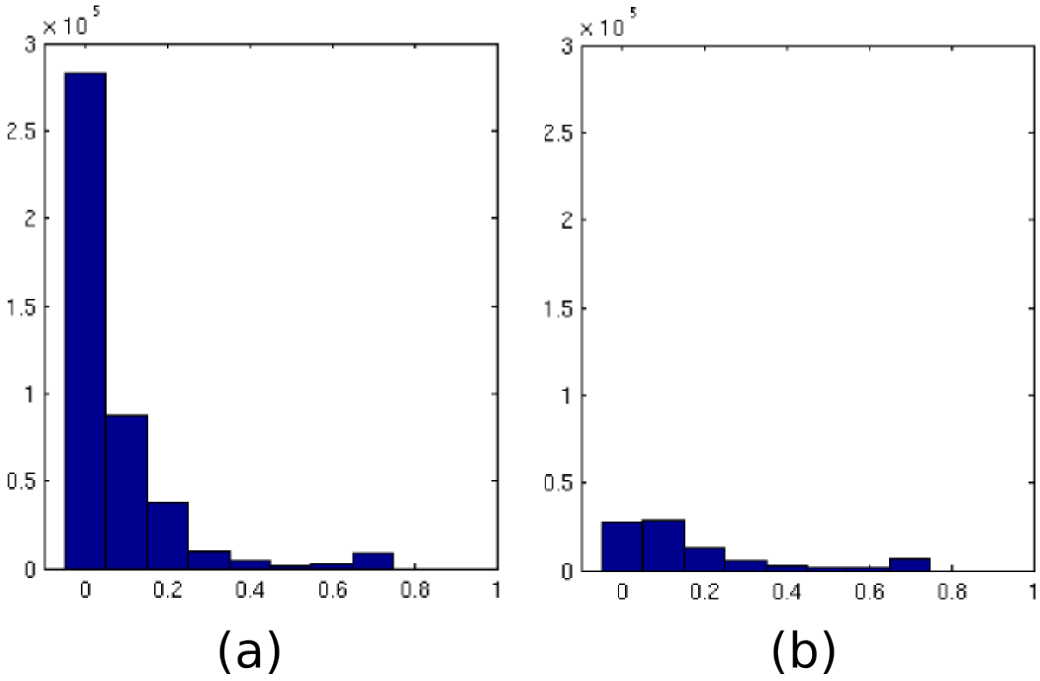

Figure 7.16: Comparison of histograms of Relative Reconstruction Error on (a) the whole of$C$ and on (b) the high gradient zone of C for the case in Figure 7.15

CHAPTER 8

Regularization Operators

The Searchlight CT reconstruction algorithm we have introduced, includes a major step involving regularization of densities outside the region of interest C. Up to this point we have used a very simple regularization technique which averages over boxes of a fixed size. In this chapter we will introduce more sophisticated regularization techniques. We start with a slight generalization of the local averaging technique. The other techniques we will study will be wavelet-based. For this purpose we will provide a brief review of wavelets, mainly in one dimension. The presentation can be naturally extended to three dimensions. The wavelet based methods will include hard thresholding, soft thresholding, and their variants.

Regularization techniques are used for a variety of mathematical and physical applications. Two major aspects of a regularization operator are its performance for the task and its computational feasibility. In the case of Searchlight CT performance is evaluated by reconstruction accuracy comparison with the 'local averaging' technique. Of course sophisticated techniques that produce better performance, are computationally more expensive. The trade off between these two aspects must be taken into account while selecting a technique.

The numerical simulations and tests in this chapter are performed in the 3D spherical acquisition model.

8.1 Adaptive Local Averaging

Here we study an adaptive generalization of the 'local averaging' operator. Earlier we computed local averages over cubic windows of fixed $(2 \times 2 \times 2)$. In this section we will use windows of adaptive size depending on the **visibility index**.

Definition 8.1.1. *Given a collimated acquisition scheme, for each point (x, y, z) in the object $\Omega \subset I^3$ the visibility index $V(x, y, z)$, is defined as the percentage of the collimated rays which pass through (x, y, z).*

Of course for points in the ROI, $V = 1$ and V decreases as we move away from the ROI. For a given point the size of the window on which we average the densities of F is determined by $\lceil \frac{1}{V(x,y,z)} \rceil$ where $\lceil u \rceil$ in the smallest integer greater than u.

The advantage of this regularization technique is that it is almost as fast as the

local averaging. The performance is marginally better than local averaging. For the same set of parameters, while local averaging yields a relative reconstruction error $Rel = 9.8\%$, adaptive local averaging does slightly better with $Rel = 9.1\%$. Though an improvement, we will attempt better results by implementing wavelet based regularization. We begin by reviewing the basics of wavelets.

8.2 A Brief Review of Wavelets

In the next section, we will present an alternative approach for the implementation of the regularization operator σ, which employs the wavelet multi-resolution analysis to regularize the function F outside the region of interest by computing the wavelet expansion of F followed by an appropriate thresholding procedure of the wavelet coefficients.

Recall that a *Multi-resolution Analysis* (MRA), in dimension $d = 1$, is defined as a sequence of closed subspaces $(V_j)_{j\in\mathbb{Z}}$ in $L^2(\mathbb{R})$ which satisfies the following properties:

(i) $\{0\} \ldots \subset V_{-2} \subset V_{-1} \subset V_0 \subset V_1 \subset V_2 \subset \ldots \subset L^2(\mathbb{R})$.

(ii) $\bigcap_{j\in\mathbb{Z}} V_j = \{0\}$ and $\overline{\bigcup_{j\in\mathbb{Z}} V_j} = L^2(\mathbb{R})$.

(iii) $f(x) \in V_j$ if and only if $f(2^{-j}x) \in V_0$.

(iv) There exists a *scaling function* $\phi \in L^2(\mathbb{R})$, such that $\{T_m\phi : m \in \mathbb{Z}\}$ is an

orthonormal basis for V_0, where $T_m\phi(t) = \phi(t-m)$.

Hence, the MRA enables the decomposition of functions into different *resolution* levels associated with the so-called *wavelet spaces* W_j, $j \in \mathbb{Z}$. Each W_j is the orthogonal complement of V_j in V_{j+1}.

$$W_j := V_{j+1} \ominus V_j, \qquad j \in \mathbb{Z}.$$

A function $f_{j+1} \in V_{j+1}$ is decomposed as $f_{j+1} = f_j + g_j \in V_j \oplus W_j$, where f_j contains, the 'lower frequency' component of f_{j+1} and g_j its 'higher frequency' component. The space $L^2(\mathbb{R})$ is then a direct sum of wavelet spaces W_j. There always exists a *wavelet* $\psi \in L^2(\mathbb{R})$ such that, for each $j \in \mathbb{Z}$, the collection

$$\{\psi_{j,k} = 2^{j/2}\psi(2^j \cdot -k) : \ k \in \mathbb{Z}\}$$

is an orthonormal basis for $V_j \subset L^2(\mathbb{R})$. Combining the various resolution levels, this implies that the collection

$$\{\psi_{j,k} = 2^{j/2}\psi(2^j \cdot -k) : \ j,k \in \mathbb{Z}\}$$

is an orthonormal basis for $L^2(\mathbb{R})$ and, thus, any $f \in L^2(\mathbb{R})$ admits the *wavelet expansion*

$$f = \sum_{j\in\mathbb{Z}} \sum_{k\in\mathbb{Z}} \langle f, \psi_{j,k}\rangle \, \psi_{j,k}. \tag{8.1}$$

Usually, the wavelet ψ is a well-localized function, so that each element $\psi_{j,k}$ has effective support size 2^{-j}. Hence, the wavelet expansion of f can be interpreted as a decomposition of f into its components associated with various scales 2^{-j} and locations $2^{-j}k$.

Essentially the same ideas hold for functions of several variables, with the difference that the wavelet ψ is replaced by a multi-wavelet $(\psi_1, \ldots, \psi_L)$ so that, for $f \in L^2(\mathbb{R}^3)$, we have the wavelet expansion

$$f = \sum_{j\in\mathbb{Z}} \sum_{k\in\mathbb{Z}} \sum_{\ell=1}^{L} \langle f, \psi^{\ell}_{j,k} \rangle \, \psi^{\ell}_{j,k}, \tag{8.2}$$

and $L = 2^D - 1$ (hence, $L = 7$ when $D = 3$). As an example, we have computed a 2-level (i.e., the scale parameter ranges over $j = 0, 1, 2$) wavelet decomposition of the human jaw data. In Figure 8.1, we reported one planar slice extracted from this decomposition, corresponding to the XY middle slice from the data set. Notice that the top figure contains the coarse information in the data and the other 2 sets below (each set contains 7 images corresponding to one of the 7 wavelet coefficients at the resolution level), represent the information associated with finer scales.

8.3 Wavelet-based Regularization

One of the most useful properties of wavelets is that they provide *optimally sparse* approximations for a large class of functions. Specifically, this holds for the function that belong to Besov spaces, a large class of functions spaces including L^2 and Sobolev spaces as special cases. If one computes the N term approximation f_N of a function f by keeping the N largest coefficients in its wavelet expansion, $\|f_N - f\|$ is asymptotically minimal. Intuitively, the large wavelet coefficients capture the main features of the function f, while the small wavelet coefficients are associated with "noise-like" features. Two classes of regularization techniques are associated with wavelets: Linear and Non-linear regularizations.

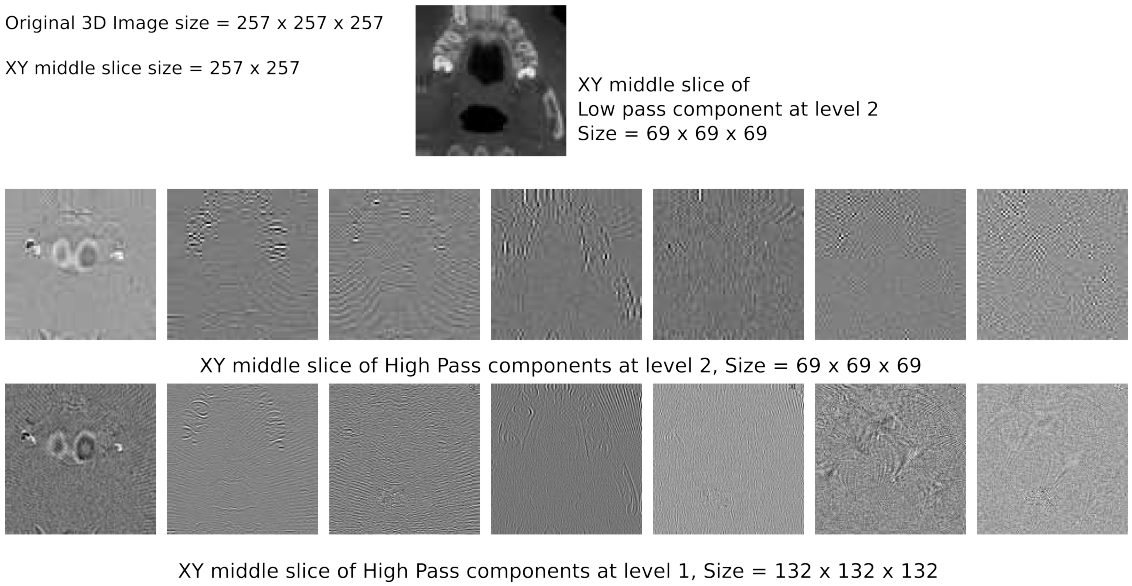

Figure 8.1: Wavelet decomposition of the human jaw data (XY middle slice is shown) where the top row is the low pass component at level 2 and the 2 rows below are the high pass components at level 2 and 1 respectively

8.3.1 Non-linear Regularization

Non-linear methods generally perform better as we retain some of the high-pass components. A very effective methods to remove the unwanted noise in a signal is obtained by a procedure called **wavelet (hard) thresholding**. This consists in calculating the wavelet expansion of f and computing its regularized version $\tilde{f}$ as

$$\tilde{f} = \sum_{j\in\mathbb{Z}} \sum_{k\in\mathbb{Z}} \sum_{\ell=1}^{L} c_{j,k,\ell}(f)\, \psi_{j,k}^{\ell},$$

where $c_{j,k,\ell}(f) = \langle f, \psi_{j,k}^{\ell} \rangle$, if $|\langle f, \psi_{j,k}^{\ell} \rangle| \geq Th_j$, and $c_{j,k,\ell}(f) = 0$ otherwise. In this procedure, the *threshold* parameters Th_j are determined as a function of the noise level at the resolution level j [1]. In several denoising applications, a useful variant of this thresholding is the so-called **soft thresholding**. where coefficients slightly

above the threshold are not fully retained but attenuated [19, 69].

For $f \in L^2(\mathbb{R}^3)$, let (8.2) be its wavelet expansion. Then we define a *hard thresholding regularization operator* σ_H as follows

$$\sigma_H f = \sum_{j\in\mathbb{Z}} \sum_{k\in\mathbb{Z}} \sum_{\ell=1}^{L} c_{j,k,\ell}(f)\, \psi_{j,k}^{\ell}, \tag{8.3}$$

where

$$\begin{cases} c_{j,k,\ell}(f) = \langle f, \psi_{j,k}^{\ell} \rangle & \text{if } j \le j_0, \\ c_{j,k,\ell}(f) = \langle f, \psi_{j,k}^{\ell} \rangle & \text{if } j > j_0 \ \& \ |\langle f, \psi_{j,k}^{\ell} \rangle| \ge Th_j, \\ c_{j,k,\ell}(f) = 0 & \text{if } j > j_0 \ \& \ |\langle f, \psi_{j,k}^{\ell} \rangle| < Th_j. \end{cases}$$

Hence σ_H acts essentially as a hard thresholding wavelet operator, with the only difference that all coarse scale coefficients at scale $j \le j_0$ are retained. The reason for keeping the coarse scales is that, in the reconstruction algorithm, σ_H will only be applied "locally" outside the region of interest S. Thus, in the construction of the regularized function $\sigma_H f$, it is important to keep all coarse coefficients which are associated with the "global" features of f.

Finally, we have also considered a similar regularization operator where the hard thresholding is replaced by soft thresholding. For $f \in L^2(\mathbb{R}^3)$, a *soft thresholding regularization operator* σ_S is given by

$$\sigma_S f = \sum_{j\in\mathbb{Z}} \sum_{k\in\mathbb{Z}} \sum_{\ell=1}^{L} c_{j,k,\ell}(f)\, \psi_{j,k}^{\ell}, \tag{8.4}$$

where

$$\begin{cases} c_{j,k,\ell}(f) = \langle f, \psi^{\ell}_{j,k} \rangle & \text{if } j \leq j_0, \\ c_{j,k,\ell}(f) = \langle f, \psi^{\ell}_{j,k} \rangle - Th_j & \text{if } j > j_0 \ \& \ \langle f, \psi^{\ell}_{j,k} \rangle \geq Th_j, \\ c_{j,k,\ell}(f) = \langle f, \psi^{\ell}_{j,k} \rangle + Th_j & \text{if } j > j_0 \ \& \ \langle f, \psi^{\ell}_{j,k} \rangle \leq -Th_j, \\ c_{j,k,\ell}(f) = 0 & \text{if } j > j_0 \ \& \ |\langle f, \psi^{\ell}_{j,k} \rangle| < Th_j. \end{cases}$$

8.3.2 Linear Regularization

In linear regularization the regularization is carried out by computing the n-level Wavelet Expansion and retaining only the low-pass component of it while setting all the high-pass components to zero. The wavelet transform is then inverted to obtain the regularized function. We have already explored a few examples of Linear Regularization operators. The regularization by local averages is a linear regularization by using the Haar Wavelet. In general other wavelets such as various forms of Daubechies wavelets or the Meyer wavelet can also be used.

To see this mathematically we consider an alternate version of the wavelet expansion. Instead of decomposing $L^2(\mathbb{R})$ as a direct sum of wavelet spaces $W_j,\ j \in \mathbb{Z}$ we apply the following equivalent decomposition.

$$L^2(\mathbb{R}) = V_0 \bigoplus \left(\bigoplus_{j \geq 0} W_j \right). \tag{8.5}$$

With this decomposition the corresponding expansion to (8.2) would be

$$f = \sum_{k \in \mathbb{Z}} \langle f, T_k \phi \rangle T_k \phi + \sum_{j \geq 0} \sum_{k \in \mathbb{Z}} \sum_{\ell=1}^{L} \langle f, \psi^{\ell}_{j,k} \rangle \psi^{\ell}_{j,k}. \tag{8.6}$$

The linearly regularized version of f is then given by simply eliminating the high resolution part of the sum. Hence the linear regularization operator is defined as,

$$\sigma_L f = \sum_{k\in\mathbb{Z}} \langle f, T_k\phi\rangle T_k\phi. \tag{8.7}$$

It is well known that non-linear regularization methods give better performance than linear methods [61] in approximations. Hence we will evaluate the numerical performance of Searchlight CT using mostly non-linear regularization methods only. However wavelet-based linear regularization will also be used for numerical studies of Searchlight CT convergence.

8.4 Numerical Demonstrations

We have considered here three regularization operators σ, namely the local averaging operator, the hard thresholding regularization operator and the soft thresholding regularization operator. The simplest choice is the local averaging operator, which was applied by selecting a moving window of size $2 \times 2 \times 2$ outside the region of interest C.

Also the thresholding regularization operators were only applied outside the spherical region of interest C. In this case, however, to ensure that no wavelet coefficients associated with the region C could be affected, the operators were applied on the complement of the region $\tilde{C}$, where $\tilde{C}$ is a sphere having the same center as C, and radius 10% larger than the radius of C. In all tests, a 3-level wavelet

decomposition was applied, using the standard Daubechies filters Daub4.

For the choice of the hard thresholding parameters, Th_j was selected so that between $5-10\%$ of the wavelet coefficients are kept at the resolution level j. In fact, heuristic observations shows that the best performance in the case of the hard thresholding operator is achieved when 9% of the highest magnitude wavelet coefficients are kept at the resolution level j.

In the case of soft thresholding, to maintain consistency with the hard thresholding, we choose Th_j in such a way that approximately 90% of the coefficients were set to zero. Since we are altering the coefficients more than by hard thresholding, the performance of soft thresholding may be expected to be worse.

We have studied the performances of the Searchlight CT algorithm for the 3D Shepp-Logan phantom and for the mouse tissues data using different choices of the regularization operator σ. In all these tests, the algorithm was run for 40 iterations which was enough to ensure adequate convergence. The results, reported in Table 8.1 and Table 8.2 shows that the wavelet-based regularization operators perform significantly better that the local averaging operator. In fact, the hard thresholding regularization operator is found to provide the best performance.

We have seen in Section 7.5 that the density function can be divided into the high gradient zone and the low gradient zone. Though the Relative Reconstruction Error *Rel* provides a global measure of performance, these errors are much higher in the high gradient zone than the low gradient zone of the density function. Hence to assess the performance of our reconstruction algorithm, we will also compute

Table 8.1: 3D Shepp-Logan phantom - Performance of Regularization Operators

Regularization Method	Rel	Rel^{LG}	Rel^{HG}
Local Averaging	9.8%	5.6%	33.6%
Hard Thresholding (7% coeff.)	8.0%	4.9%	25.5%
Hard Thresholding (9% coeff.)	7.8%	4.8%	24.8%
Hard Thresholding (5% coeff.)	8.5%	5.0%	28.3%
Soft Thresholding (9% coeff.)	8.6%	5.1%	28.4%
Soft Thresholding (12% coeff.)	8.5%	5.1%	27.8%

Table 8.2: Mouse Tissue - Performance of Regularization Operators

Regularization Method	Rel	Rel^{LG}	Rel^{HG}
Local Averaging	10.3%	5.9%	35.2%
Hard Thresholding (7% coeff.)	8.7%	5.2%	28.5%
Hard Thresholding (9% coeff.)	8.4%	5.1%	27.1%
Hard Thresholding (5% coeff.)	9.3%	5.4%	31.4%
Soft Thresholding (9% coeff.)	9.5%	5.5%	32.1%
Soft Thresholding (12% coeff.)	9.4%	5.4%	32.0%

the quantities Rel^{HG} and Rel^{LG}, measuring the Relative Reconstruction Error Rel restricted respectively to the high gradient region and to the low gradient region.

Both thresholding methods, specially the hard thresholding leads to significantly better performance. These methods are computationally more expensive than the local averaging technique due to their complexity. In particular for a ROI-radius of 50 voxels 40 iterations of the Searchlight CT reconstruction algorithm ran in 6 hours using the local averaging regularization but took 8 hours using wavelet based hard thresholding regularization. However the improved performance outweighs the additional computing time and leads to a better convergence criterion on the Relative density, $D(C, F)$.

For accurate reconstruction with local averaging we required $D(C, F) > 2.5\%$ for

the Shepp-Logan phantom. With hard thresholding we only require $D(C, F) > 2.3\%$ which is almost a 10% improvement. The corresponding figures for the rat tissue data were $D(C, F) > 2.8\%$ with local averaging and $D(C, F) > 2.5\%$ with hard thresholding.

8.5 Effect of Regularization Techniques on Spectral Radius

In this section we will discuss the effect of regularization in context of convergence analysis for the 2D case. We have discussed different regularization techniques on the complement of ROI. Since we have used linear theory in the context of convergence analysis through spectral radius (see Chapter 3), we will restrict the spectral radius study here to linear regularization methods. As in Chapter 3, a phantom of size 45×45 is used. The basis used is the standard basis $\{E_{ij}\}$ for $\mathbb{R}^{45\times 45}$, where E_{ij} is a 45×45 matrix with 1 in the (i, j)th position and 0's everywhere else. Note that we cannot use the same reduction of dimensions as done for the local averages regularization method since the regularized function will not be constant on blocks. Results for the spectral radius of the operator $M = \sigma X^{-1} 1_U X \sigma$ using linear regularization with the the standard Daubechies daub4 wavelet are shown in Table 8.3. Various ROI-radii between 4 and 16 pixels were examined.

We perform a spectral analysis similar to the study in Chapter 3. For a reasonably large ROI-radius (13 pixels), where convergence does hold the histogram of the

Table 8.3: Spectral radius $\rho(M)$ for various radii of C

ROI-radius	$\rho(M)$
4 pixels	12.63
7 pixels	9.13
8 pixels	6.42
9 pixels	3.55
10 pixels	0.78
13 pixels	0.64
16 pixels	0.52

modulus of the eigenvalues of M is shown in Figure 8.2.

Again if we make the radius smaller, convergence does not occur. The histogram for the modulus of the eigenvalues of M for such a case (with ROI-radius equal to 8 pixels) is shown in Figure 8.3.

We note that the spectral radii for the converging cases is lower for wavelet-based linear regularization than local averaging. For example at the critical radius of 10 pixels wavelet based linear regularization produced a spectral radius of 0.78 while local averaging regularization produced 0.82. This leads to a faster rate of convergence. Another improvement (for the diverging cases) is the number of expanding eigenvectors. For example, when the ROI-radius is 8 pixels local averaging regularization led to 10 expanding eigenvectors as compared to 6 for wavelet-based linear regularization. This could be exploited when the projection analysis is carried out similar to Section 3.3 is performed.

As before we observe the eigenvector corresponding to the highest eigenvalue and identify its high intensity zones. We note that in case of wavelet-based linear regularization the concentration of this expanding eigenvector in the region C is

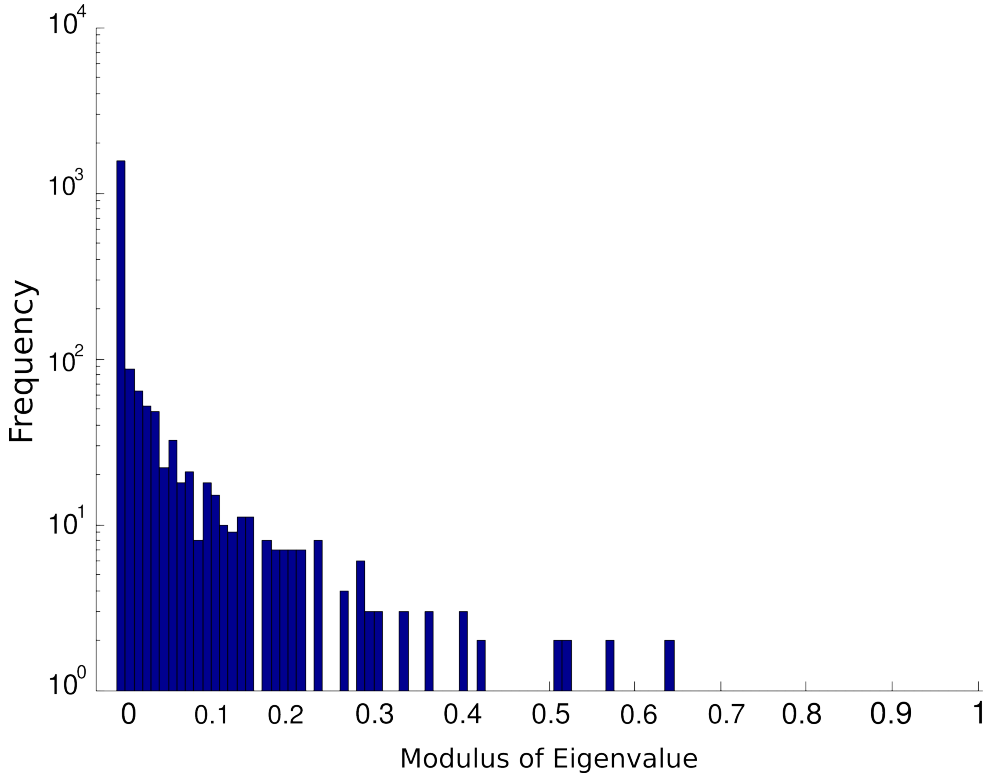

Figure 8.2: Histogram for the eigenvalues of M for a converging case when the radius of C is 13 pixels (using wavelet-based linear regularization)

much stronger. This is shown in Figure 8.4 for an ROI-radius of 8 pixels.

Next we will note the effect of the expanding eigenvectors with the same definitions and notations as Section 3.3. As the number of expanding eigenvectors are fewer in this case, we expect the expansion weight defined in Section 3.3 ω_d to be lower. Hence the approximation by projecting into the contracting subspace should be more accurate. The value of ω_d for various radii between 4 and 8 pixels is shown in Table 8.4.

In stark contrast to the local averaging case, wavelet-based linear regularization gives a low value of ω_d even for a radius of 6 pixels. Hence PF is an acceptable

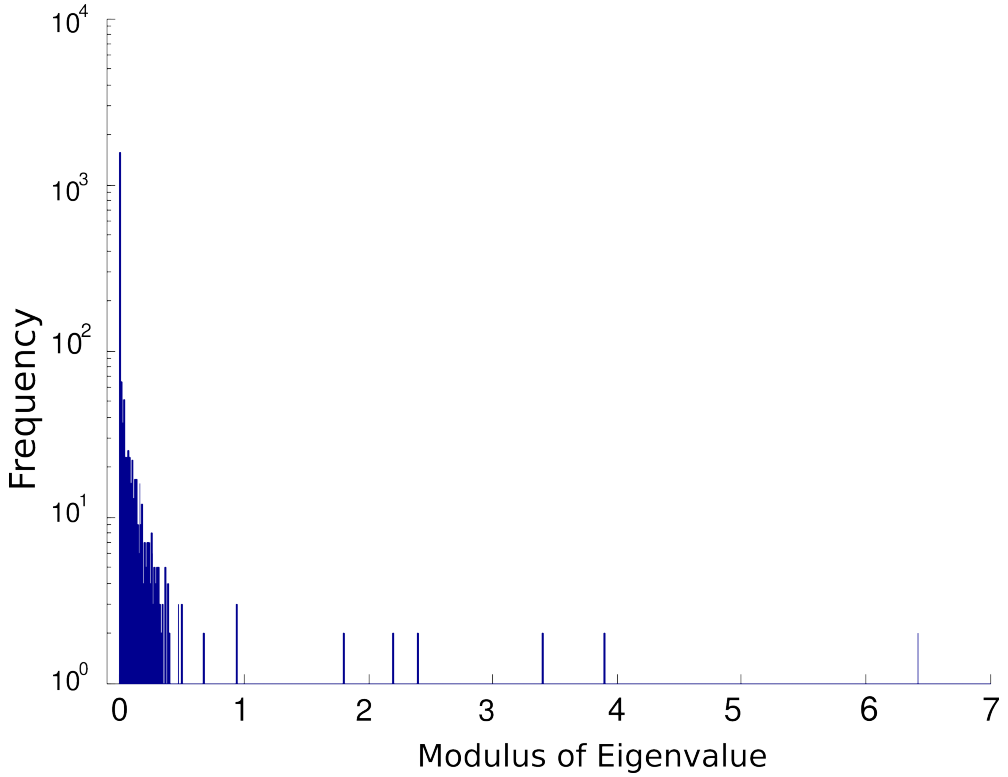

Figure 8.3: Histogram for the eigenvalues of M for a diverging case when the radius of C is 8 pixels (using wavelet-based linear regularization)

approximation to the regularized version of the objective function F. For very low ROI-radii (under 5 pixels) the approximation by PF is inaccurate. These cases are shown in Figure 8.5.

For PF to be a good approximation of F the weight, ω_d should be sufficiently small. We have seen through extensive numerical tests on various data sets that the

Table 8.4: Expansion weight ω_d for small ROI-radii for wavelet-based linear regularization

ROI-Radius	4 pixels	5 pixels	6 pixels	7 pixels	8 pixels
Expansion Weight, ω_d	5.19%	3.83%	2.23%	1.37%	0.66%

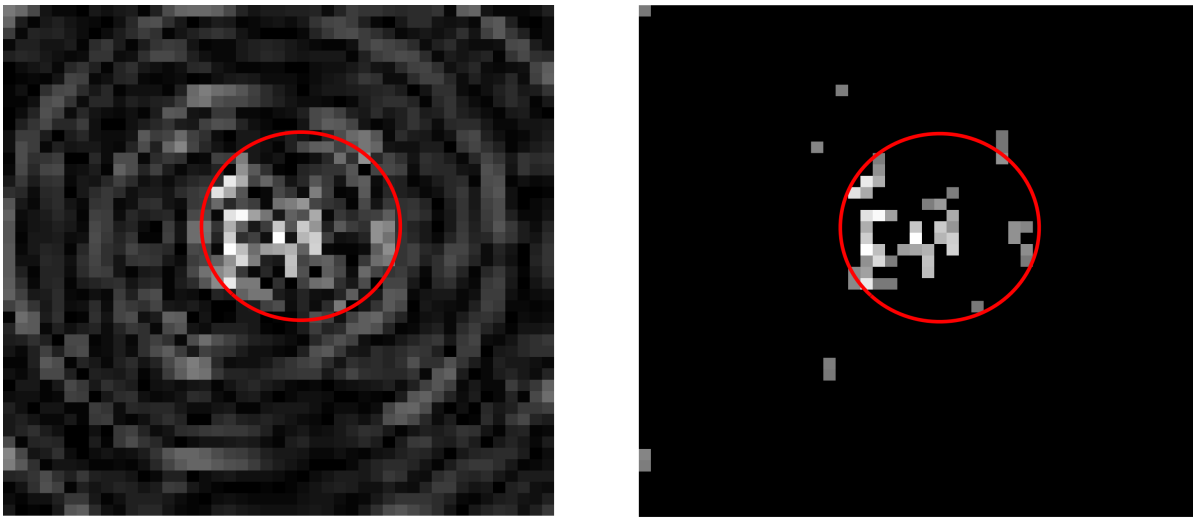

Figure 8.4: For the diverging case when radius of C is 8 pixels (a) Image of the eigenvector corresponding to the highest eigenvalue and (b) its high intensity zone calculated using the described method with $\alpha = 85\%$ (using wavelet-based linear regularization)

upper bound for ω_d is approximately 2.5%. Any value greater than this would fail to approximate F accurately. This fact can be used to formalize an alternate version for Searchlight CT when the ROI-radius is small.

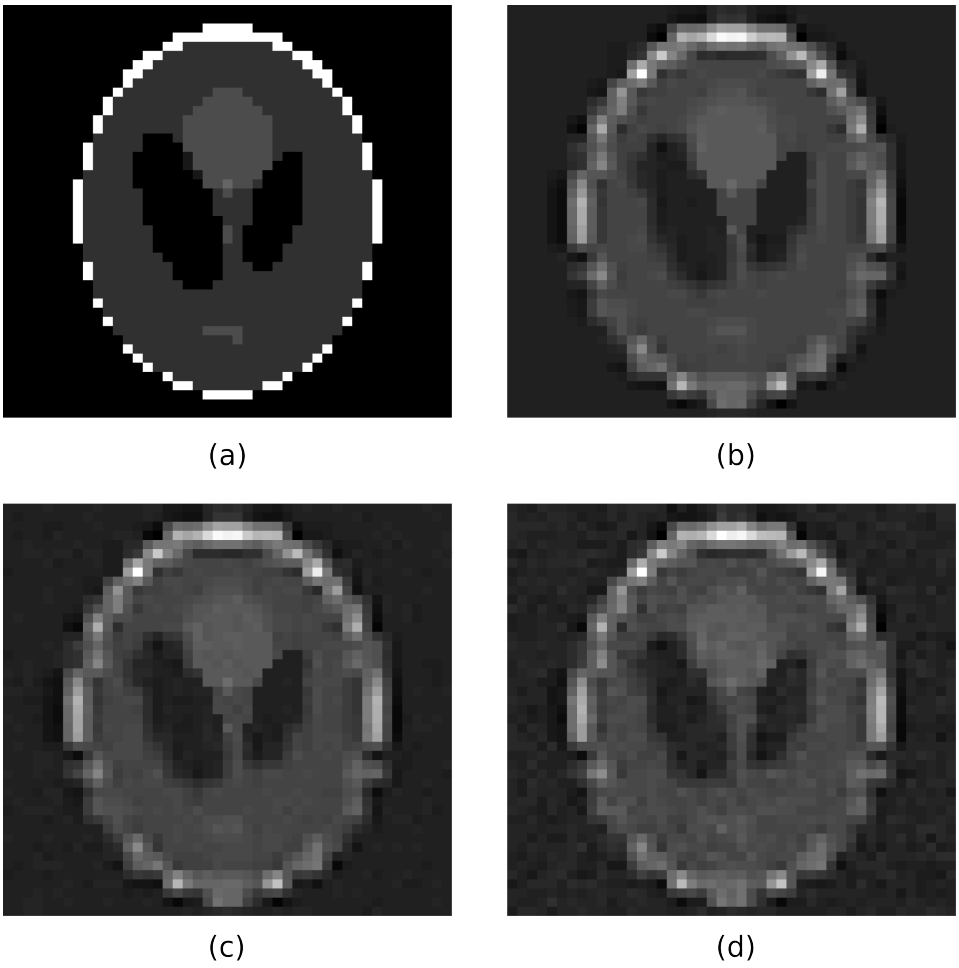

Figure 8.5: (a) The Shepp-Logan phantom of size 45 (b) Phantom linearly regularized using wavelets outside the ROI of radius 8 pixels (c) Projection of the wavelet-regularized phantom with ROI-radius 6 pixels on to the contracting subspace of M(d) Projection of the wavelet-regularized phantom with ROI-radius 5 pixels on the contracting subspace of M

8.6 Searchlight CT for Small Regions of Interest

When the ROI-radius is too small during collimated acquisition the affected *ROI* cannot be treated by Searchlight CT to give an accurate reconstruction. In such cases, we propose an alternative version of Searchlight CT. We have no way of computing ω_d from the CT data. Hence we first assume ω_d to be less than 2.5% and carry out the computations. In case ω_d is higher than 2.5% the reconstruction would fail. This alternate version of Searchlight CT has an additional step after each regularization namely a step to project the regularized function on the contracting subspace of M i.e. the space spanned by the contracting eigenvectors of M. The steps for the 2D case are briefly summarized below. The notations used are exactly the same as in Chapter 2 (2.22). Initially we need to compute the contracting subspace of M.

1. Compute σf_n through local averaging (2.20) or any of the mentioned wavelet-based techniques [(8.3) or (8.4)].

2. Compute $P\sigma f_n$ as in (3.9), that is project σf_n into the contracting subspace of M.

3. Compute $XP\sigma f_n$, the standard X-ray Transform of $P\sigma f_n$, using (2.1). By separating the $XP\sigma f_n$ into the complementary sets T and U, write

$$XP\sigma f_n = 1_T.XP\sigma f_n + 1_U.XP\sigma f_n.$$

4. Replace $1_T.XP\sigma f_n$ by the known data $G = 1_T.XF$ in the preceding formula to define $Y_n = G + 1_U.XP\sigma f_n$.

5. Compute f_{n+1} by applying the X-ray inversion formula (2.6) to Y_n. Hence,

$$f_{n+1} = X^{-1}Y_n = X^{-1}[G + 1_U.XP\sigma f_n]. \tag{8.8}$$

8.7 Other Regularization Techniques

Other regularization techniques may be used depending on the trade off between accuracy and computational efficiency. Though both the thresholding methods are effective, due to numerical round off errors can generate inaccuracies. To remove such inaccuracies the regularization process can be iterated. Another variant could be to implement a step of soft thresholding after a step of hard thresholding. The major disadvantage of such iterated or multi-step methods is that they are computationally very expensive.

Regularization techniques similar to the ones described in this chapter have been explored for Computed Tomography in various papers. One of the options could be to replace wavelets by complex wavelets. The complex wavelet transform is a complex-valued extension of the standard discrete wavelet transform. It is a two-dimensional wavelet transform which provides multi-resolution, sparse representation, and useful characterization of the structure of an image. The use of complex wavelets in image processing was originally set up in 1995 by J.M. Lina and L. Gagnon [60] in the framework of the Daubechies orthogonal filters banks [59]. It was then generalized in 1997 by Nick Kingsbury [51, 82, 50] of Cambridge University. Regularization through complex wavelets in CT scans is seen in [90, 91, 77].

Another regularization technique could be to use shearlets instead of wavelets. The traditional wavelet transform does not posses the ability to detect directionality, since it is merely associated with two parameters, the scaling parameter and the the translation parameter. The shearlet transform attempts to overcome this problem, while retaining the key aspects of wavelets' the mathematical framework. The shearlets satisfy all these properties in addition to showing optimal behavior with respect to the detection of directional information. The inversion of the Radon Transform by using shearlets is presented for 2D in [21, 20].

CHAPTER 9

Reconstruction from Noisy Data

In medical imaging noise can occur in several ways. In this chapter we review the effect of noise on medical images and the various associated noise models. We test the sensitivity of the Searchlight CT algorithm to noise.

9.1 Noise in Medical Imaging

Noise occurring in imaging devices have far-ranging effects. Noise is typically defined as the uncertainty in a signal due to random fluctuations in that signal.There are many causes for such fluctuations. We briefly discuss the presence and causes for

noise in some imaging processes.

In tomography, an X-ray beam is statistical in nature. That is, the number of photons emitted from the source per unit time varies according to a Poisson distribution [54]. These fluctuations primarily come from the inherent random variations in the counting of photons and is related to the number of photons detected and used for the generation of images [79]. Other sources of random fluctuation introduced by the process of attenuation of the materials present in the path of the radiation beam such as the patient, patient table, detector enclosure, etc. are also Poisson processes. Finally, the detectors themselves often introduce noise. Another source of noise is the interaction between digital and analogue signals in mixed signal systems [52].

Positron Emission Tomography (PET) is another form of tomography. The PET system detects pairs of gamma rays emitted indirectly by a positron-emitting tracer (radioactive material), which is introduced into the body on a biologically active molecule. Three-dimensional images of tracer concentration within the body are then reconstructed by computer analysis. In PET images, the main sources of noise are in decreasing order of magnitude are emission, transmission, and blank scans [38]. Detectors, electronics, and recorder systems together may add to the noise [62, 92]. The choice of reconstruction algorithm significantly affect the magnitude and texture of noise. Other factors which contribute to noise features include mode of corrections, in particular attenuation correction.

Along with Computed Tomography, Magnetic Resonance Imaging (MRI) is another important diagnostic tool in medical imaging. There are two major sources of

noise in MRI. Rician noise arises from complex Gaussian noise in the original frequency domain measurements [67]. A different type of noise in the coherent imaging of objects is called speckle noise. This noise is, in fact, caused by errors in data transmission [30, 32]. Speckle noise also has a major advantage. It is very useful for viewing a MR image by following the path of noise.

Noise in digital pictures is caused by heat in the sensor. Astronomical photographers that use long exposures a lot often cool the sensor up to -20°C with a Peltier unit, just to avoid noise. When light levels are high in any exposure this inherent noise level will only be a tiny percentage. It's when we come to low light shots that noise becomes a noticeable problem as the exposure moves into the underlying sensor noise.

9.2 Noise Models

There are various noise models which appear in different forms of images. We will briefly describe some of these models in this section. Most of these models are based on a probability distribution, for which details can be found in [6]. To see the effect of noise we will consider a very simple 2D test image consisting of three identical vertical strips with the central one having a relatively lower density (0.3) as compared to the other two (0.7). The image along with the histogram of its intensity values is shown in Figure 9.1.

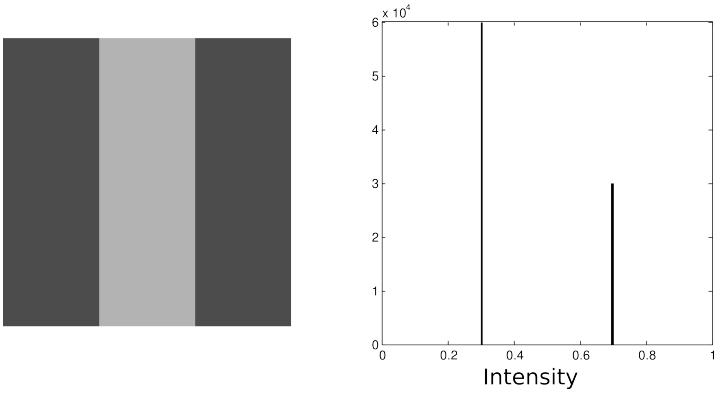

Figure 9.1: The test image and its histogram

Uniform Noise

The uniform noise model is based on the continuous uniform distribution, i.e. every value in the given range has an equal probability. For $a, b \in \mathbb{R}$ the distribution is denoted by $U(a, b)$ and the probability density function is given by,

$$f(x) = \begin{cases} \frac{1}{b-a} & x \in [a, b] \\ 0 & \text{otherwise} \end{cases}. \tag{9.1}$$

Generally uniform noise is not encountered in real life imaging systems but is important for comparison purposes. It can be used to generate any other type of noise and is also used to degrade images for denoising algorithms as it provides the most unbiased form of noise. Uniform noise on the test image is shown in Figure 9.2

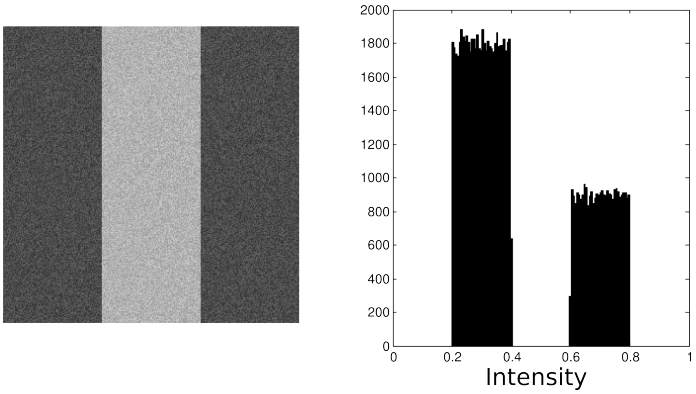

Figure 9.2: The test image corrupted with uniform noise

Exponential Noise

The exponential noise model is based on the exponential distribution. For $\lambda > 0$ the probability density function is,

$$f(x) = \begin{cases} \lambda e^{-\lambda x} & x \geq 0 \\ 0 & x < 0 \end{cases}. \tag{9.2}$$

This type of noise is used to model noise in laser imaging. It is shown in Figure 9.3.

Rayleigh Noise

The Rayleigh distribution models the Raleigh noise. For $\sigma > 0$ the probability density function is given by,

$$f(x) = \frac{x}{\sigma^2} e^{-\frac{x^2}{2\sigma^2}} \qquad x \geq 0. \tag{9.3}$$

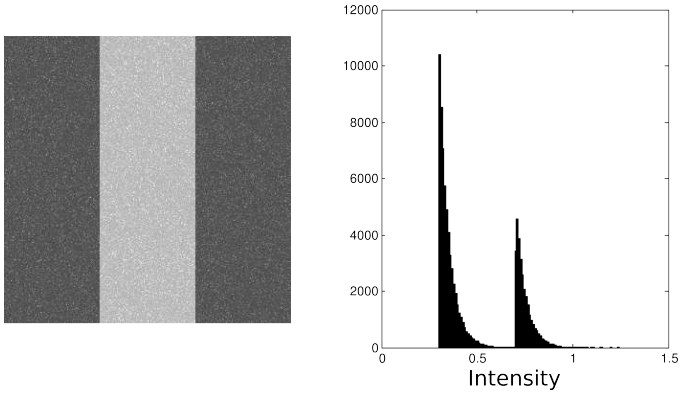

Figure 9.3: The test image corrupted with exponential noise

It is used to model noise in range imaging and velocity images. Raleigh noise occurs typically in Magnetic Resonance Imaging (MRI). As MRI images are recorded as complex images but most often viewed as magnitude images, the background data is Rayleigh distributed. Hence, a maximum likelihood estimate for the parameter can be used to estimate the noise variance in an MRI image from background data [83].

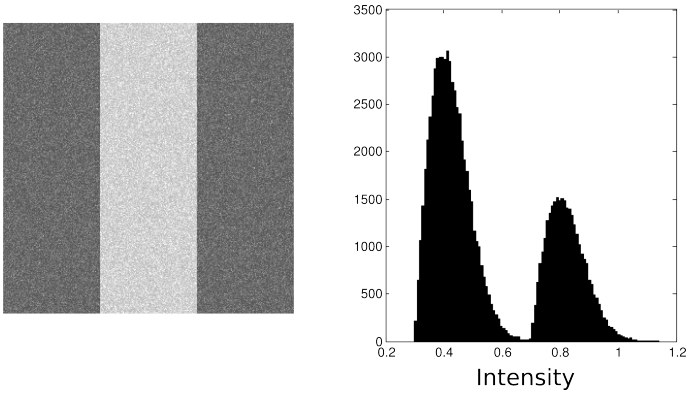

Figure 9.4: The test image corrupted with Rayleigh noise

Gamma (Erlang) Noise

The Gamma distribution models the Gamma noise. For $k > 0$ and $\theta > 0$ the distribution is denoted as $\Gamma(k, \theta)$ and its probability density function is,

$$f(x) = \frac{1}{\Gamma(k)\theta^k} x^{k-1} e^{-\frac{x}{\theta}} \qquad x \geq 0 \tag{9.4}$$

where $\Gamma(z) = \int_0^\infty e^{-t} t^{z-1} dt$.

Gamma noise can be obtained by lowpass filtering exponential noise. The exponential nature of the histogram of the intensities is apparent in Figure 9.5.

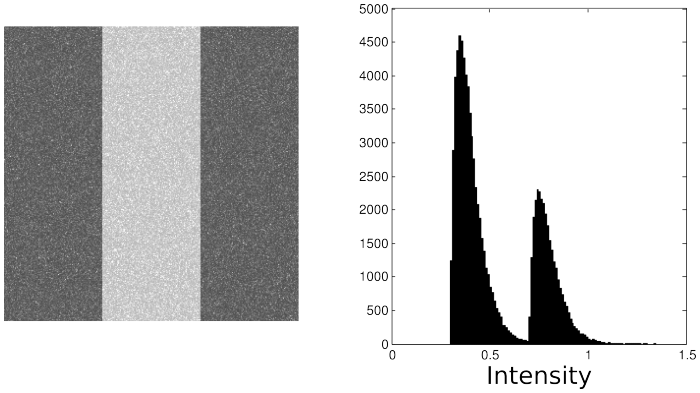

Figure 9.5: The test image corrupted with Gamma noise

Salt-and-Pepper (Impulse) Noise

This is one of the few types of noise that is not based on any of the regular probability distributions. It occurs during image transmission due to malfunctioning of pixel elements in sensors, faulty memory locations or errors in digitalization process. The true value of the pixel gets corrupted either to a high intensity (salt) with a fixed

probability or a low intensity (pepper) with another fixed probability, as seen in Figure 9.6.

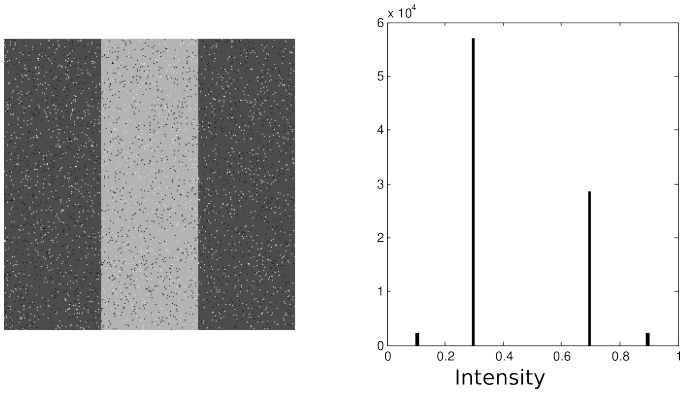

Figure 9.6: The test image corrupted with salt-and-pepper noise

Poisson Noise

Unlike most of the other types of noise, Poisson noise is based on a discrete probability distribution, the Poisson distribution. For $\lambda > 0$ the probability mass function for Poisson distribution is given by,

$$f(k) = \frac{\lambda^k e^{-\lambda}}{k!} \qquad k = 0, 1, 2 \ldots . \tag{9.5}$$

Poisson noise exists in situations where an image is created by the accumulation of photons over a detector. Typical examples are found in standard X-ray films, CCD cameras, and infrared photometers. An example on the test image is seen in Figure 9.7.

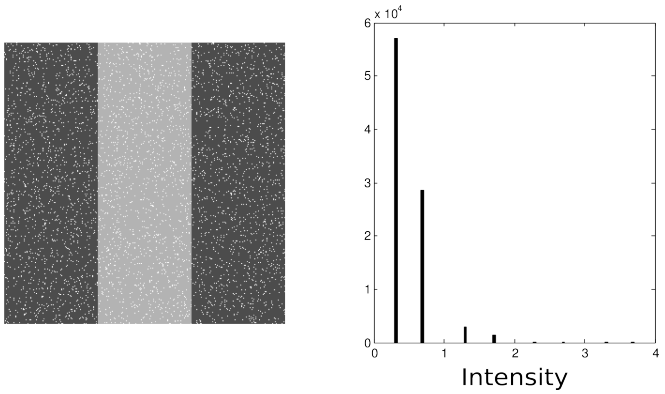

Figure 9.7: The test image corrupted with Poisson noise

Gaussian Noise

The Gaussian model based on the normal distribution is most often used for modeling natural noise processes. For $\mu \in \mathbb{R}$ and $\sigma^2 > 0$ the normal distribution is denoted by $N(\mu, \sigma^2)$ and its probability density function is,

$$f(x) = \frac{1}{\sigma\sqrt{2\pi}} e^{\frac{(x-\mu)^2}{2\sigma^2}}. \tag{9.6}$$

During the data acquisition of a CT scan process, the electronic noise is Gaussian distributed [95]. A special type of Gaussian noise is **Additive White Gaussian Noise**. This is a form of additive noise with zero mean and the noise at each voxel is independent of other voxels. Naturally, this type of noise occurs due to vibration of atoms due to heat (thermal noise), black body radiation etc. Some examples are CT scans (short range) and satellite or deep space links (very long range). Gaussian noise on the test image is seen in Figure 9.8.

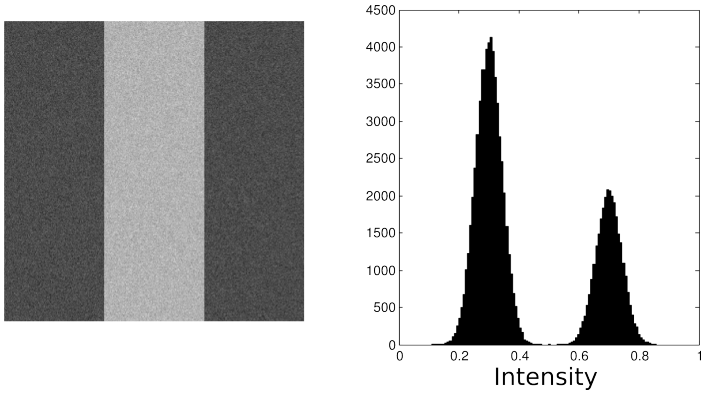

Figure 9.8: The test image corrupted with Gaussian noise

9.3 Effect of Noise on Searchlight CT

An important indicator for the performance of the Searchlight CT algorithm is its robustness when the data are corrupted by noise. To test our algorithm in this situation, we run several numerical experiments where additive white Gaussian noise was added to the data. Of course, not all noise found in practical applications is of this type, but this is a standard experiment which is indicative of the stability of the reconstruction algorithm.

We run our experiments in two cases. First we run Searchlight CT on noisy data to test its robustness of the algorithm to noisy data. Next we use a standard denoising technique to denoise the data and then we run Searchlight CT on the denoised data.

Thus, in our experiments, we manually modified the acquired X-ray data $X(w, \theta)$ by adding a noise term δ which is a normally distributed random variable with mean

Table 9.1: Performance of Noisy Reconstruction (Phantom)

Noise	Regularization Method	E_r	E_r^{LG}	E_r^{HG}
$\sigma = 0.05A$	Local Averaging	15.0 %	10.2 %	42.2 %
$\sigma = 0.05A$	Hard Thresholding	12.1 %	8.5 %	32.5 %
$\sigma = 0.05A$	Soft Thresholding	13.1 %	8.9 %	36.9 %
$\sigma = 0.01A$	Local Averaging	12.4 %	8.0 %	37.3 %
$\sigma = 0.01A$	Hard Thresholding	11.1 %	7.4 %	32.0 %
$\sigma = 0.01A$	Soft Thresholding	11.6 %	7.6 %	34.2 %

0 and standard deviation σ.

$$\bar{X}F(w,\theta) = XF(w,\theta) + \delta, \tag{9.7}$$

where $\delta \sim N(0,\sigma)$. In our our tests, σ was chosen in the range $[0.01A, 0.05A]$ where $A = \text{mean}(XF(w,\theta))$.

9.3.1 Searchlight CT with Noisy Data

We tested the performance of the reconstruction from noisy data using various types of regularization. For both hard and soft thresholding 91% of the coefficients were set to zero. The results for the Shepp-Logan phantom are given in Table 9.1.A comparison between the noisy reconstruction of a region C in the Shepp-Logan phantom and ground truth is shown in Figure 9.9, where $\sigma = 0.05A$ and regularization by hard thresholding was used.

A similar experiment was carried out for the mouse tissue data. The same set of parameters for the standard deviation of noise and wavelet thresholding were used. The corresponding results for the noisy mouse tissue data are reported in Table 9.2. A comparison between the noisy reconstruction of a region C in the mouse tissue

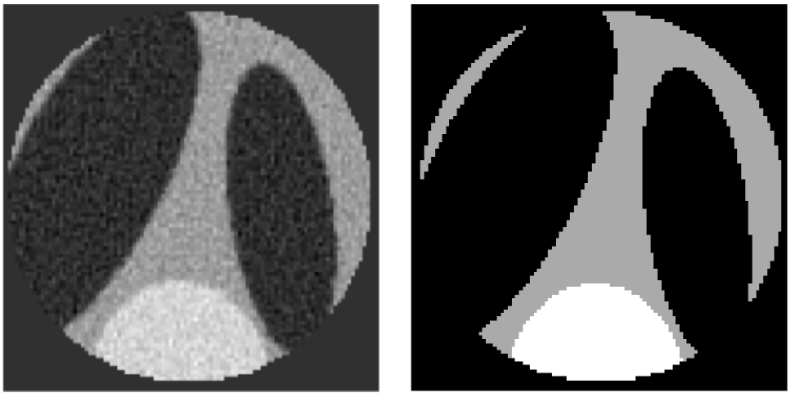

(a) Noisy Reconstruction by Searchlight CT

(b) Ground Truth

Figure 9.9: Comparison between (a) Noisy reconstruction by Searchlight CT (b) ground truth for a 2D representative slice of the 3D Shepp-Logan phantom

Table 9.2: Performance of Noisy Reconstruction (Mouse Tissue)

Noise	Regularization Method	E_r	E_r^{LG}	E_r^{HG}
$\sigma = 0.05A$	Local Averaging	15.7 %	10.8 %	43.4 %
$\sigma = 0.05A$	Hard Thresholding	12.6 %	9.0 %	33.0 %
$\sigma = 0.05A$	Soft Thresholding	13.8 %	9.6 %	37.6 %
$\sigma = 0.01A$	Local Averaging	13.0 %	8.5 %	38.5 %
$\sigma = 0.01A$	Hard Thresholding	11.9 %	8.1 %	33.4 %
$\sigma = 0.01A$	Soft Thresholding	12.4 %	8.2 %	36.2 %

data and ground truth is shown in Figure 9.10, where $\sigma = 0.05A$ and regularization by hard thresholding was used.

9.3.2 Searchlight CT on Denoised Data

We have examined the robustness of Searchlight CT to noisy data. As a final experiment we tested Searchlight CT on denoised data. As mentioned in Chapter 8 one of the most prominent denoising techniques is the wavelet thresholding. As stated

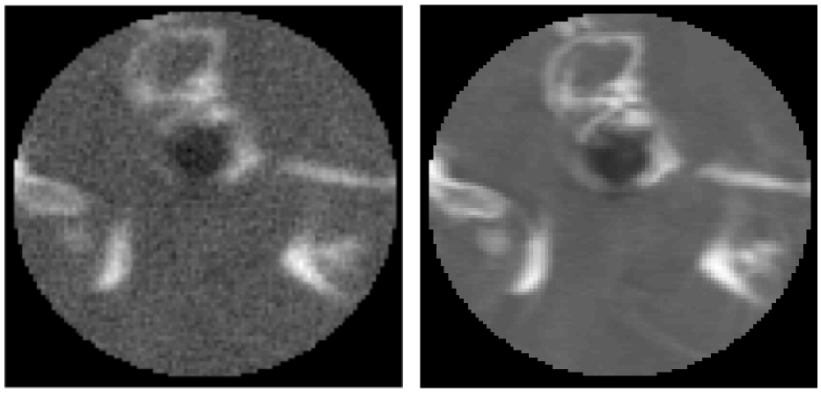

(a) Noisy Reconstruction by Searchlight CT

(b) Ground Truth

Figure 9.10: Comparison between (a) Noisy reconstruction by Searchlight CT (b) ground truth for a 2D representative slice of the mouse tissue data

before we simulate the noisy data by,

$$\bar{X}F(w,\theta) = XF(w,\theta) + \delta,$$

with $\delta \sim N(0,\sigma)$. With the same notation as Section 8.2, we write the wavelet expansion of $\bar{X}F$ as,

$$\bar{X}F = \sum_{j\in\mathbb{Z}}\sum_{k\in\mathbb{Z}}\sum_{\ell=1}^{L}\langle \bar{X}F, \psi_{j,k}^{\ell}\rangle\, \psi_{j,k}^{\ell}. \tag{9.8}$$

Table 9.3: Performance of Reconstruction from Denoised Data (Phantom)

Noise	Regularization Method	E_r	E_r^{LG}	E_r^{HG}
$\sigma = 0.05A$	Local Averaging	14.2 %	9.3 %	41.9 %
$\sigma = 0.05A$	Hard Thresholding	11.6 %	8.0 %	32.0 %
$\sigma = 0.01A$	Local Averaging	11.9 %	7.8 %	35.1 %
$\sigma = 0.01A$	Hard Thresholding	10.7 %	7.2 %	30.5 %

Using hard thresholding the denoised data $\check{X}F$ is given by,

$$\check{X}F = \sum_{j\in\mathbb{Z}}\sum_{k\in\mathbb{Z}}\sum_{\ell=1}^{L} c_{j,k,\ell}(\bar{X}F)\,\psi_{j,k}^{\ell},$$

where (9.9)

$$\begin{cases} c_{j,k,\ell}(\bar{X}F) = \langle \bar{X}F, \psi_{j,k}^{\ell}\rangle & \text{if } j \le j_0, \\ c_{j,k,\ell}(\bar{X}F) = \langle \bar{X}F, \psi_{j,k}^{\ell}\rangle & \text{if } j > j_0 \;\&\; |\langle \bar{X}F, \psi_{j,k}^{\ell}\rangle| \ge Th_j, \\ c_{j,k,\ell}(\bar{X}F) = 0 & \text{if } j > j_0 \;\&\; |\langle \bar{X}F, \psi_{j,k}^{\ell}\rangle| < Th_j. \end{cases}$$

The threshold Th_j for a scale level j is set to be the 91st quantile of the absolute wavelet coefficients. In our experiments we perform the initial denoising step by setting to zero, 91% of the lowest magnitude wavelet whose magnitude is below the threshold. The other parameters are the same as the previous section. Since hard thresholding gave a better performance than soft thresholding, we present the experiments only for hard thresholding. The performance of Searchlight CT on the denoised data for the Shepp-Logan phantom is detailed in Table 9.3 and a comparison of the reconstruction with ground truth is shown in Figure 9.11. Similarly for the mouse tissue data, the performance of Searchlight CT is detailed in Table 9.4 and a comparison of the reconstruction with ground truth is shown in Figure 9.12.

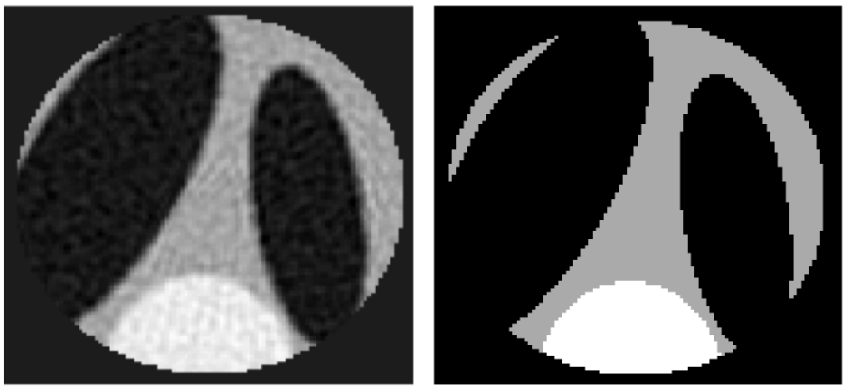

(a) Reconstruction from Denoised Data (b) Ground Truth

Figure 9.11: Comparison between (a) reconstruction by Searchlight CT on denoised data (b) ground truth for a 2D representative slice of the 3D Shepp-Logan phantom

Table 9.4: Performance of Reconstruction from Denoised Data (Mouse Tissue)

Noise	Regularization Method	E_r	E_r^{LG}	E_r^{HG}
$\sigma = 0.05A$	Local Averaging	14.8 %	10.0 %	42.0 %
$\sigma = 0.05A$	Hard Thresholding	11.9 %	8.4 %	31.7 %
$\sigma = 0.01A$	Local Averaging	12.0 %	8.1 %	34.1 %
$\sigma = 0.01A$	Hard Thresholding	11.2 %	7.2 %	33.8 %

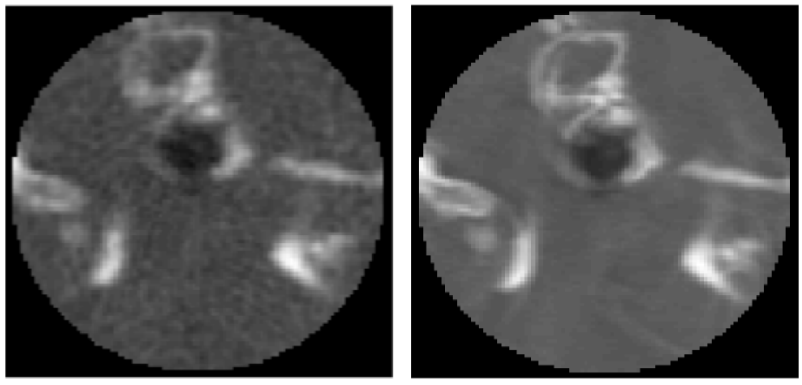

(a) Reconstruction from Denoised Data (b) Ground Truth

Figure 9.12: Comparison between (a) reconstruction by Searchlight CT on denoised data (b) ground truth for a 2D representative slice of the mouse tissue data

CHAPTER 10

Reconstruction of 3D Collimated Data with Spiral Acquisition

In Chapter 3 we have adapted a 3D collimated X-ray computed tomography setup when sources are placed in a sphere around the object Ω. Though the reconstruction accuracy is very satisfactory, one of the major shortcomings of this method is that it is practically infeasible. Also if a spherical CT scanner ever came into existence, the high number of projections would require a very high radiation dose and defeat the purpose of reducing the patient's exposure to harmful radiation. Spiral Tomography provides a very attractive alternative to such a problem. Instead of the source positions being required on a surface, it just requires them to lie on a curve, in particular a circular helix.

This chapter gives a brief explanation spiral tomography. The exact inversion formula for inversion proved by Alexander Katsevich in [45] is explained along with the required definitions and basic results. Finally we apply our algorithm to test for Collimated Reconstruction. Though notations used in this chapter are consistent withe previous ones, the introductory discussion follows [68].

10.1 Spiral Tomography

Let F be a 3D density function with support Ω. Ω is assumed to be contained in the vertical cylinder $x^2 + y^2 < R^2$, where $R < R_0$ and R_0 is the radius of the circular helix. The region $x^2 + y^2 < R^2$ is called the field of view.

As defined above the X-ray Transform of F is a set of line integrals of F on rays from a given source position. In this chapter the sources are placed on a circular helix, with axis as the z-axis, radius R_0 and pitch (distance between successive turns) P. This helix can be parametrically represented as,

$$s(\lambda) = \left[R_0 \cos(\lambda + \lambda_0), R_0 \sin(\lambda + \lambda_0), z_0 + P\frac{\lambda}{2\pi} \right]. \tag{10.1}$$

Often in experiments we assume $\lambda_0 = 0$. At $\lambda = 0$ the source position is on the plane $z = z_0$ at polar angle λ_0. For a given source position, $s(\lambda)$, the X-ray Transform is given by,

$$XF(\lambda, \theta) = \int_0^\infty F(s(\lambda) + t\theta)dt \qquad \theta \in S^2. \tag{10.2}$$

Note that instead of w as our previous notation, we now use s as the point determining the the ray, where s is also a source position. Since s is determined completely

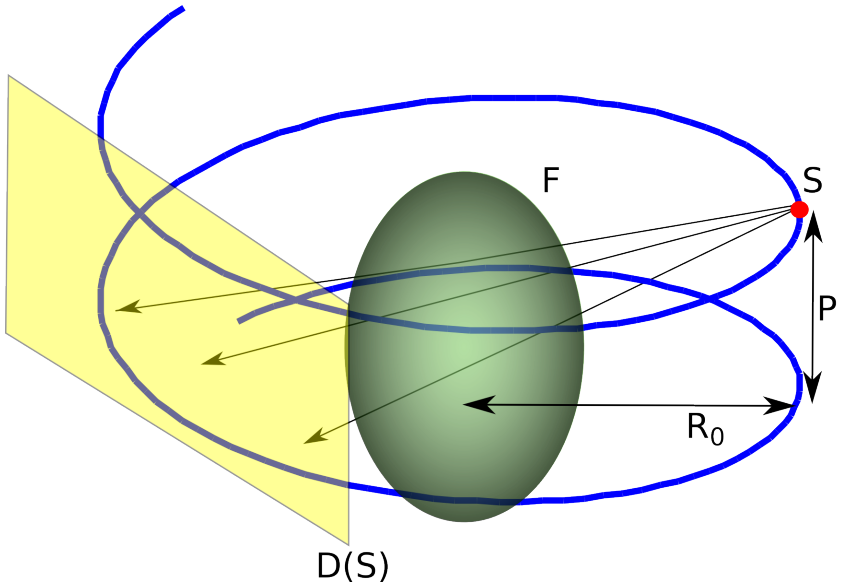

Figure 10.1: The physical setup for spiral acquisition

by λ, as seen in (10.1), we can use λ in (10.2) to define the X-ray Transform. The physical setup for spiral tomography is shown in Figure 10.1

10.2 Geometry of Data Acquisition on a Flat Detector

In a flat detector geometry, X-ray projections are measured using flat panel detectors which are placed beyond the object to be reconstructed and parallel to the z-axis. The detector rotates around the object along with the object along with the source, $s(\lambda)$ such that it is always perpendicular to the plain containing $s(\lambda)$ and the z-axis. To describe the data acquisition better, we introduce the rotated coordinates, with

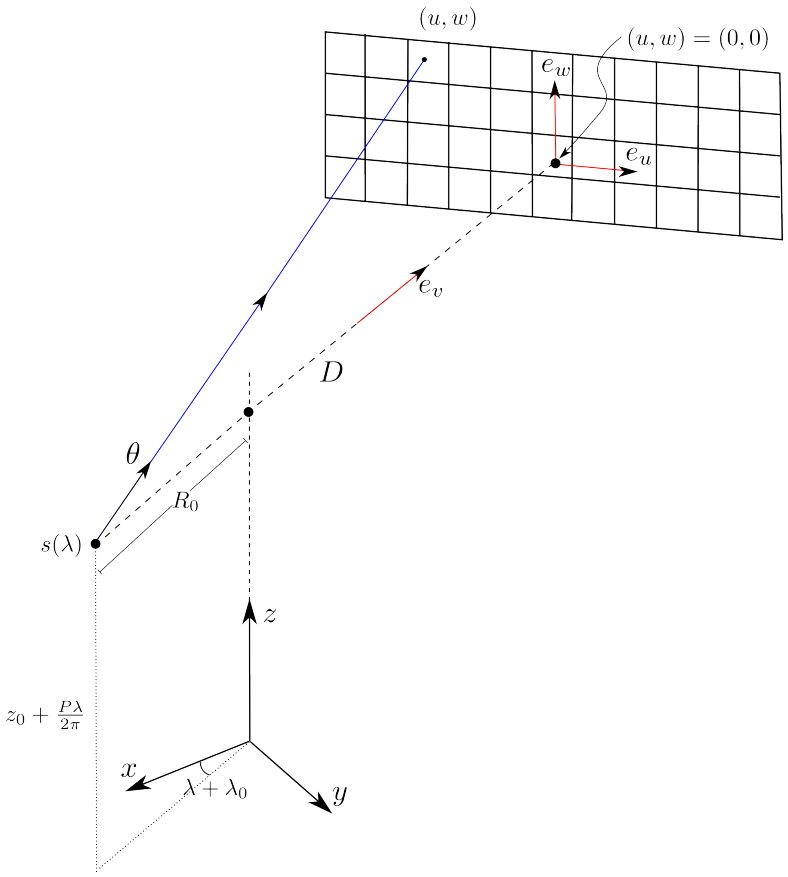

Figure 10.2: Geometry of data acquisition on a flat detector

unit vectors e_u, e_v and e_w defined as,

$$e_u(\lambda) = (-\sin(\lambda + \lambda_0), \cos(\lambda + \lambda_0), 0), \tag{10.3a}$$

$$e_v(\lambda) = (-\cos(\lambda + \lambda_0), -\sin(\lambda + \lambda_0), 0), \tag{10.3b}$$

$$e_w = (0, 0, 1). \tag{10.3c}$$

Thus the detector is perpendicular to e_v. It is assumed that the distance between the source and the detector always remains a constant D. The size of the detector is determined by the size of the object for the width (number of columns) and the

helical pitch P for the height (number of rows). A derivation for the minimum number of rows required for exact reconstruction for a given P can be found in [68]. The coordinate system on the detector is specified by two mutually orthogonal coordinates u and w along e_u and e_w respectively. The center $(u, w) = (0, 0)$ is at the orthogonal projection of $s(\lambda)$ on to the detector. To describe the data acquisition we require a transformation of coordinates between (λ, θ) and (λ, u, w). This is explained below. Denoting the projections obtained by flat panel detectors as $XF_f(\lambda, u, w)$, we have,

$$XF_f(\lambda, u, w) = XF(\lambda, \theta_f).$$

It can be geometrically seen from Figure 10.2 that,

$$\theta_f = \frac{1}{\sqrt{u^2 + D^2 + w^2}}(ue_u(\lambda) + De_v(\lambda) + we_w). \tag{10.4}$$

Conversely for a given direction θ such that,

$$XF(\lambda, \theta) = XF_f(\lambda, u_f, w_f),$$

it can easily shown by the triangle law of vector addition that,

$$u_f = D\frac{\theta.e_u(\lambda)}{\theta.e_v(\lambda)}, \tag{10.5a}$$

$$w_f = D\frac{\theta.e_w}{\theta.e_v(\lambda)}. \tag{10.5b}$$

There is another type of data acquisition which uses a curved detector instead of a flat. A brief description of this method is given in [68, 96].

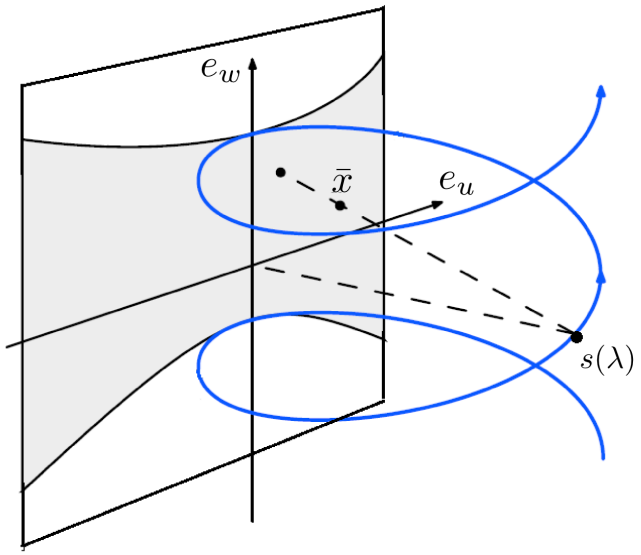

Figure 10.3: The Tam-Danielsson window

10.3 Katsevich Inversion Formula

The exact inversion formula for the X-ray Transform for spiral tomography was proved by Katsevich in [41, 43] and improved in [45]. Two key advantages of the formula are its computational efficiency as it is essentially a filtered back-projection and the truncation of projection in the z-direction. To have an idea of the truncation in the $z-$ direction, we define a Tam-Danielsson window.

Definition 10.3.1. *For a given source position $s(\lambda)$, the region on the detector plane bounded immediately above and below by the projections of the helix onto the detector plane when viewed from $s(\lambda)$ is called the Tam-Danielsson window.*

A visual representation of a Tam-Danielsson is shown in Figure 10.3. Before stating the formula, we need some definitions and observations.

10.3.1 Preliminaries

One of the basic notions in the Katsevich inversion formula is a $\pi-$line.

Definition 10.3.2. *Given a circular helix (as parameterized by* (10.1)*). A* $\pi-$ *line is any segment of a line that connects two points on the the helix,* $s(\lambda_i)$ *and* $s(\lambda_j)$ *such that* $|\lambda_i - \lambda_j| < 2\pi$.

Equivalently a $\pi-$line connects two points separated by less than one helical turn. $\pi-$ lines satisfy the following theorem whose proof can be found in [17, 16].

Theorem 10.3.3. *If* $\bar{x}$ *is in the field of view (or support* Ω *of the density function* F*), then there exists an unique* $\pi-$*line passing through* $\bar{x}$.

Since the extremities of the $\pi-$line geometrically define a 180°coverage around $\bar{x}$ the following conjecture regarding the exact reconstruction of F at $\bar{x}$ was made in [16] and later proved by Katsevich in [45].

Theorem 10.3.4. *Let* $\bar{x}$ *be in the field of view with* $s\lambda_i(\bar{x})$ *and* $s\lambda_j(\bar{x})$ *denoting the extremities of the unique* $\pi-$*line through* $\bar{x}$*. If the projection of* $\bar{x}$ *on to the detector lies in the Tam-Danielsson window, then* F *can be reconstructed exactly at* $\bar{x}$ *from the X-ray projection data for the source positions,* $s(\lambda),\ \lambda \in [\lambda_i(\bar{x}), \lambda_j(\bar{x})]$.

A portrayal of a $\pi-$line is shown in Figure 10.4. The segment of the helix between its end points (also called a $\pi-$segment) is highlighted. In view of the above theorem we can define the set of rays required to reconstruct F at $\bar{x}$. For source positions, $s(\lambda),\ \lambda \in [\lambda_i(\bar{x}), \lambda_j(\bar{x})]$ let the corresponding Tam-Denielsson window be denoted by $D(\lambda)$. For a fixed λ, its set of directions is given by,

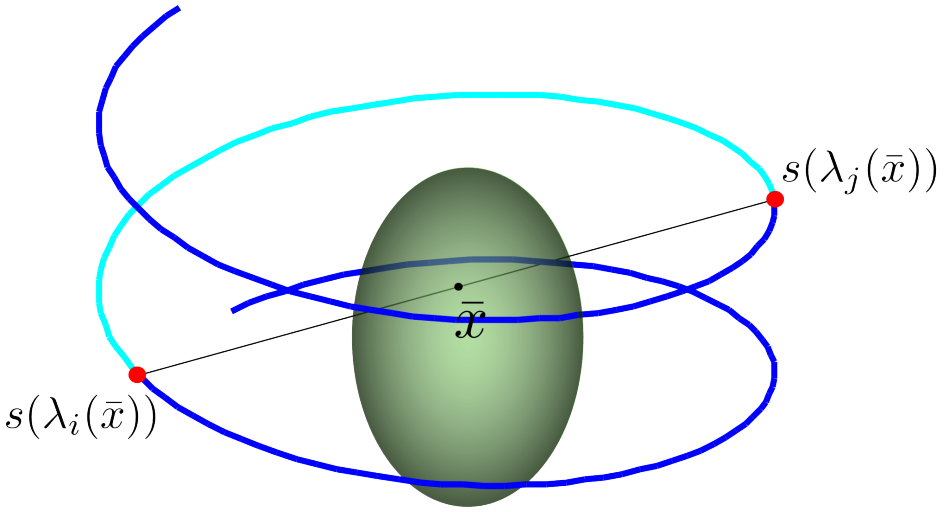

Figure 10.4: A π-line with the $\pi-$segment highlighted

$$\Theta_\lambda = \left\{ \frac{s(\lambda) - b}{\|s(\lambda) - b\|} : b \in D(\lambda) \right\}. \tag{10.6}$$

Provided the projection of $\bar{x}$ lies in the Tam-Danielsson window for every for every λ, i.e. for each $\lambda \in [\lambda_i(\bar{x}), \lambda_j(\bar{x})]$, $\exists b \in D(\lambda)$ such that for some $t \in \mathbb{R}$, $\bar{x} = s(\lambda) + t\frac{s(\lambda)-b}{\|s(\lambda)-b\|}$, the total set of rays needed for reconstruction at $\bar{x}$ is given by,

$$S = \{l(\lambda, \theta) : \lambda \in [\lambda_i(\bar{x}), \lambda_j(\bar{x})],\ \theta \in \Theta_\lambda\}. \tag{10.7}$$

Next we define a $\kappa-$plane.

Definition 10.3.5. *A $\kappa-$plane is any plane that has three intersections with the helix such that one of them is midway between the other two.*

$\kappa-$planes satisfy the following property,

Theorem 10.3.6. *If $\bar{x}$ lies in the field of view and its projection from $s(\lambda)$ on to the detector lies in the Tam-Danielsson window, then there is a unique $\kappa-$plane through $\bar{x}$ and $s(\lambda)$.*

The points of intersection of a $\kappa-$plane with the helix are generally denoted as $s(\lambda),\ s(\lambda+\psi)$ and $s(\lambda+2\psi)$ with $\psi \in [-\pi, \pi]$. So for the result stated above, ψ is uniquely determined. However we will see that for the Katsevich formula we require some data outside the Tam-Daniellson window. Hence the unicity of $\kappa-$planes is lost.

We are interested in a family of $\kappa-$planes for a given source position $s(\lambda)$. A $\kappa-$plane through $s(\lambda)$ determined by ψ is denoted as $\kappa(\lambda, \psi)$. Together $\pi-$lines and $\kappa-$planes obey the following important property [45].

Theorem 10.3.7. *For an $\bar{x}$ in the field of view, let $\lambda_i(\bar{x})$ and $\lambda_j(\bar{x})$ define the extremities of the $\pi-$line through $\bar{x}$ with $\lambda_i(\bar{x}) < \lambda_j(\bar{x})$. For any $\lambda \in [\lambda_i(\bar{x}), \lambda_j(\bar{x})]$ there exists a $\kappa-$plane $\kappa(\lambda, \psi)$ at $s(\lambda)$ that contains $\bar{x}$.*

Since unicity may not hold, there might exist more than one such $\kappa-$plane. However there will exist a $\kappa-$plane with the least value of $|\psi|$ and it will satisfy $\lambda_i(\bar{x}) \leq \lambda + 2\psi \leq \lambda_j(\bar{x})$. This plane is used in the Katsevich Formula.

Also note that the unit normal vector $m(\lambda, \psi)$ to the $\kappa-$plane $\kappa(\lambda, \psi)$ is given by,

$$m(\lambda, \psi) = \frac{(s(\lambda+\psi) - s(\lambda)) \times (s(\lambda+2\psi) - s(\lambda))}{\|(s(\lambda+\psi) - s(\lambda)) \times (s(\lambda+2\psi) - s(\lambda))\|}, \text{sign}(\psi) \tag{10.8}$$

keeping the angle between $m(\lambda, \psi)$ and the z-axis acute.

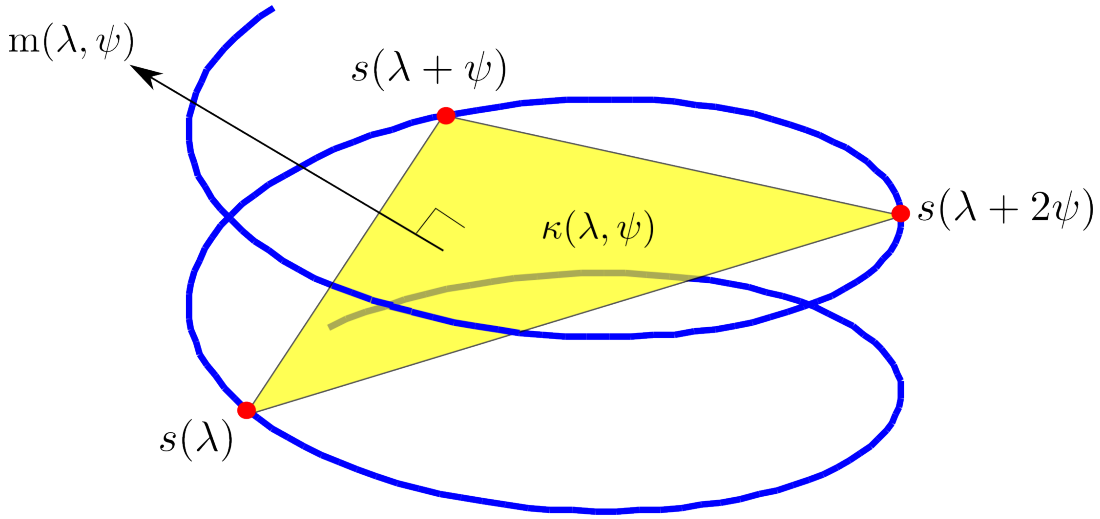

Figure 10.5: A portion of a $\kappa-$plane and its normal vector

A portion of a $\kappa-$plane with its normal vector is shown in Figure 10.5.

10.3.2 The Inversion Formula

Katsevich proved the inversion formula to reconstruct the density of $\bar{x}$ in the field of view by back-projecting the X-ray projections from source positions at the extremities of a $\pi-$line through $\bar{x}$. The back-projection step involves the filtered data $XF^{\ell}(\lambda, \theta)$.

$$F(\bar{x}) = X^{-1}(XF)(\bar{x}) = -\frac{1}{2\pi}\int_{\lambda_i(\bar{x})}^{\lambda_j(\bar{x})} \frac{1}{\|\bar{x} - s(\lambda)\|} XF^{\ell}\left(\lambda, \frac{\bar{x} - s(\lambda)}{\|\bar{x} - s(\lambda)\|}\right) d\lambda, \quad (10.9)$$

where $\lambda_i(\bar{x})$ and $\lambda_j(\bar{x})$ are the extremities of the $\pi-$line described above and $\lambda_i(\bar{x}) < \lambda_j(\bar{x})$.

To obtain the filtered data $XF^{\ell}(\lambda,\theta)$ we first require the derivative $XF'(\lambda,\theta)$ of $XF(\lambda,\theta)$ with respect to λ for a fixed θ. Then $XF^{\ell}(\lambda,\theta)$ can be calculated as,

$$XF^{\ell}(\lambda,\theta) = \int_0^{2\pi} h_H(\sin\gamma) XF'(\lambda, \cos\gamma\theta + \sin\gamma(\theta \times m(\lambda,\theta)))d\gamma. \tag{10.10}$$

In the above equation, $h_H(t)$ stands for the the Hilbert Transform kernel,

$$h_H(t) = -\int_{-\infty}^{\infty} i\text{sign}(\sigma) e^{2i\pi\sigma t} d\sigma = \frac{1}{\pi t}, \tag{10.11}$$

and $m(\lambda,\theta)$ is normal to the plane $\kappa(\lambda,\psi)$ of smallest $|\psi|$ that contains $\bar{x}$ and $s(\lambda)$. It must be noted that $m(\lambda,\theta)$ always exists. From (10.9) $XF^{\ell}(\lambda,\theta)$ needs to be known only for the directions θ specified a a source position $s(\lambda)$ towards the point $\bar{x}$. A discussed before for such θ there always exists a κ-plane st $s(\lambda)$ containing $\bar{x}$. The condition on $|\psi|$ to be minimum enforces such a plane to be unique.

10.4 A New Reconstruction Algorithm in Spiral Tomography

As we have the methods for data acquisition and inversion, we are in a position to apply our algorithm to test the reconstruction for collimated projections. Before we proceed, we need to describe how the various the steps are modified in case of spiral tomography.

Data Acquisition

We have already defined the X-ray Transform for spiral tomography in (10.2). However direct computation of this is time-consuming so we will carry out the data acquisition by the Fourier Slice Theorem as in Chapter 6. This will be described in the next Chapter.

Simulated Collimation

The collimated X-ray Transform is defined exactly as in Chapters 2 and 4. Let F be a Lebesgue integrable function with compact support Ω and $l(\lambda, \theta)$ the line through $s(\lambda) \in \mathbb{R}^3$ with direction $\theta \in S^2$. Let C be a spherical region within Ω. Then Collimated X-ray Transform of F (in this spiral setting) is defined as,

$$\tilde{X}(\lambda, \theta) = \begin{cases} XF(\lambda, \theta) & l(\lambda, \theta) \bigcap C \neq \emptyset \\ 0 & l(\lambda, \theta) \bigcap C = \emptyset \end{cases}. \tag{10.12}$$

In view of the definition (10.12), we denote the fully retained part of the X-ray Transform as T and $U = T^C$.

$$T = \{(\lambda, \theta) : l(\lambda, \theta) \bigcap C \neq \emptyset\}.$$

The collimation condition (5.9) derived in Chapter 5 was independent of the acquisition method. It was just a condition for a line $l(w, \theta)$ to intersect a sphere centered at (p, q, r) and with radius R. In the case of spiral tomography the only difference would be that the set of w's is given by the source positions (10.1). Using

this condition for all the source positions we can block the rays not passing through the region of interest. For a ray with direction $\theta = (\theta_1, \theta_2, \theta_3)$ and passing through $s(\lambda) = (s_1, s_2, s_3)$ and a spherical region C, centered at (p, q, r) of radius Q, the collimation condition (i.e the condition for the ray to pass through C), is given by:

$$\left[(s_1 - p)^2 + \frac{\theta_1^2}{\theta_3^2}s_3^2 - 2\frac{\theta_1}{\theta_3}s_3(s_1 - p) + (s_2 - q)^2 + \frac{\theta_2^2}{\theta_3^2}s_3^2 - 2\frac{\theta_2}{\theta_3}s_3(s_2 - q) + r^2 - Q^2\right] \geq 0.$$

Inversion

The reconstruction technique given in [68] reconstructs one horizontal slice at a time using the Katsevich inversion formula (10.9).

$$F(\bar{x}) = X^{-1}(XF)(\bar{x}) = -\frac{1}{2\pi}\int_{\lambda_i(\bar{x})}^{\lambda_j(\bar{x})} \frac{1}{\|\bar{x} - s(\lambda)\|} XF^{\ell}\left(\lambda, \frac{\bar{x} - s(\lambda)}{\|\bar{x} - s(\lambda)\|}\right) d\lambda.$$

For our algorithm to work, we require the reconstruction of the entire objective function F. Since the reconstruction on a single slice is computationally very efficient we repeat the step for all horizontal slices to obtain the complete reconstruction.

Regularization

Our regularized reconstruction from collimated X-ray data will follow essentially the same procedure as in Chapter 5. Since we have already verified that the wavelet-based based regularization method with hard wavelet thresholding of the wavelet coefficients, works the best, we will use only that technique for spiral tomography. With the same notation as Section 8.2, we write the wavelet expansion of F as,

$$F = \sum_{j\in\mathbb{Z}} \sum_{k\in\mathbb{Z}} \sum_{\ell=1}^{L} \langle F, \psi_{j,k}^{\ell} \rangle \, \psi_{j,k}^{\ell}.$$

Then the regularized version $\sigma_H F$ is given by,

$$\sigma_H F = \sum_{j\in\mathbb{Z}} \sum_{k\in\mathbb{Z}} \sum_{\ell=1}^{L} c_{j,k,\ell}(F) \, \psi_{j,k}^{\ell}, \tag{10.13}$$

where

$$\begin{cases} c_{j,k,\ell}(F) = \langle F, \psi_{j,k}^{\ell} \rangle & \text{if } j \le j_0, \\ c_{j,k,\ell}(F) = \langle F, \psi_{j,k}^{\ell} \rangle & \text{if } j > j_0 \ \& \ |\langle F, \psi_{j,k}^{\ell} \rangle| \ge T_j, \\ c_{j,k,\ell}(F) = 0 & \text{if } j > j_0 \ \& \ |\langle F, \psi_{j,k}^{\ell} \rangle| < T_j. \end{cases}$$

The Algorithm

As above, the algorithm is initialized by setting $G = \tilde{X}F = 1_T.XF$, and by computing the initial approximation of F as f_0 by applying (10.9) to G, i.e. $f_0 = X^{-1}G$. The subsequent approximations f_n, $n \ge 1$, of F are obtained through the following iterative procedure.

1. Compute $\sigma_H f_n$ as in (10.13).

2. Compute $X\sigma_H f_n$, the standard X-ray Transform of σf_n, using (10.2) (by the implementation technique described in Section 11.1). By projecting the data into the complementary sets T and U, write

$$X\sigma_H f_n = 1_T.X\sigma f_n + 1_U.X\sigma_H f_n.$$

3. Replace $1_T.X\sigma_H f_n$ by the known data $G = 1_T.XF$ in the preceding formula to define $Y_n = G + 1_U.X\sigma_H f_n$.

4. Compute f_{n+1} by applying the Katsevich inversion formula (10.9) to Y_n. Hence,

$$f_{n+1} = X^{-1}Y_n = X^{-1}[G + 1_U.X\sigma_H f_n]. \tag{10.14}$$

10.5 Numerical Analysis of Convergence through Spectral Radius

We repeat the same experiment as in the case of spherical acquisition case, Section 5.6. We use the same size of data (in a cubical voxel grid of size 32^3) and adjust the parameters accordingly.

Size of Data	=	32^3 voxels
Helical scanning radius	=	48 voxels
Source Detector distance	=	96 voxels
Helical Pitch	=	4 voxels
Number of detector rows, M	=	8
Sources per turn	=	$16M = 128$

The values of the spectral radius $\rho(M)$ of the operator $M = \sigma X^{-1}1_U X\sigma$ for various ROI-radii are given in Table 10.1.

Table 10.1: Spectral radius, $\rho(M)$ of M for ROI's of various ROI-radii (with 3D spiral acquisition and wavelet-based linear regularization)

ROI-radius	3 voxels	5 voxels	6 voxels	7 voxels	9 voxels	11 voxels
$\rho(\mathbf{M})$	14.57	7.31	4.11	0.95	0.80	0.73

Again a minimal radius of 5 voxels was required for convergence. The spectral radius is comparatively higher than the 3D spherical acquisition case.

The study of the spectral radius to ascertain convergence has a very important practical implication. We have seen another condition for convergence in Section 7.1, which requires the calculation of the Relative Density $D(C, F)$, for a region of interest C. However this value can only be estimated. The calculation of the spectral radius gives an apriori condition for convergence which is independent of the density function and depends only on its support size, the region C and the techniques for acquisition, inversion and regularization. With these we can compute the spectral radius and infer if convergence is possible.

We have verified this technique in three acquisition techniques: 2D cone-beam acquisition, 3D spherical acquisition and 3D spiral acquisition. In addition the technique works well with two types of regularization: local averaging and wavelet-based linear regularization. In actual practice the apriori simulated acquisition may not be exact but an educated guess can still be made about the possibility of convergence.

CHAPTER 11

Numerical Results for Reconstruction of 3D Collimated Data with Spiral Acquisition

We have described the procedure for spiral tomography along with the Katsevich inversion formula. The Searchlight CT algorithm for spiral tomography has also been described. This chapter deals with the implementation of the Searchlight CT algorithm in this setting and numerical results. The implementation of the Katsevich inversion was coded by Adam Wunderlich in [96]. We have used the same code. However for the data acquisition we will use our acquisition independent technique described in Chapter 6. We will also discuss the dependence of the Searchlight CT

algorithm on its various parameters.

11.1 Implementation of Data Acquisition

The data acquisition technique suggested in [68] and implemented in [96], is suitable for piece-wise polynomial objective functions in the most general setting. We will use the technique suggested in Section 5.2 to generalize data acquisition for any function.

Recall from Section 5.2, the data acquisition technique described was independent of the acquisition technique. With notations as before, for any ray of direction θ, emitted from a source position located at $s(\lambda)$ we have a plane $P(\phi, \psi)$, such that this ray is orthogonal to it. As in Section 6.1.3, we can compute the corresponding $w \in \mathbb{R}^3$ (and $\theta \in S^2$) which identify a ray. Note that we had assumed w to lie on the orthogonal plane $P(\phi, \psi)$, and hence we require to recalculate w satisfying this extra condition. Hence every ray required for spiral acquisition can be expressed in the form required in (10.9).

However due to the discretization in w and θ, interpolation is required. Let $l(w_i, \theta_i)$ be the rays for which the X-ray Transform is already known. For any ray $l(w, \theta)$ we locate its four nearest neighbors by minimizing the distance,

$$\eta_i = \|(w, \theta) - (w_i, \theta_i)\|. \tag{11.1}$$

For convenience let the four smallest distances be η_1, η_2, η_3, and η_4. Then $XF(w, \theta)$ is calculated by using weighted linear interpolation.

$$XF(w, \theta) = \frac{\eta_1 XF(w_1, \theta_1) + \eta_2 XF(w_2, \theta_2) + \eta_3 XF(w_3, \theta_3) + \eta_4 XF(w_4, \theta_4)}{\eta_1 + \eta_2 + \eta_3 + \eta_4}. \tag{11.2}$$

11.2 Performance of Searchlight CT with Spiral Tomography

In this section we will examine the performance of Searchlight CT with spiral tomography. We will first introduce a set of parameters which were used in the experiments for this section. In the next section we will vary some of these parameters to see how the performance varies with it.

Size of Data	=	256^3 voxels
Helical scanning radius	=	384 voxels
Source Detector distance	=	768 voxels
Helical Pitch	=	35 voxels
Number of detector rows, M	=	8
Sources per turn	=	$16M = 128$

As a first test, we vary the radius of the region C and evaluate the performance of the reconstruction algorithm. First the Shepp-Logan phantom is tested and then the real mouse data. We expect the accuracy of reconstruction to be slightly worse than the spherical acquisition as the number of source positions are significantly lower. The performance measures Relative Reconstruction Error Rel, Radiation Exposure E, Relative Density D and Peak Signal to Noise Ratio $PSNR$ will be used as above.

It must be noted that, for best results, approximately 50 iterations are required

Table 11.1: Performance of Searchlight CT with spiral tomography for various ROI-radii (Shepp-Logan phantom)

ROI-radius	D	E	Rel	$PSNR$
45 voxels	3.8 %	21%	10.9 %	56.5 dB
60 voxels	8.5 %	33%	9.1 %	59.3 dB
75 voxels	15.3 %	47%	8.3 %	62.3 dB
90 voxels	23.8 %	60%	8.0 %	62.7 dB

but that is computationally expensive. The computation time was approximately twelve hours as compared to eight hours for the spherical acquisition case. This is primarily due to the recalculation of w and interpolation carried out during the data acquisition which leads to slightly worse reconstruction. Within the iteration the acquisition takes about twice as long as the inversion. As a compromise it is possible to perform a lesser number of iterations. This is a trade off between performance and computational efficiency.

The performance for Searchlight CT using spiral tomography for radii of C between 45 and 90 voxels is tabulated in Table 11.1. A comparison between the standard reconstruction and the reconstruction through Searchlight CT is shown in Figure 11.1.

A fact about exposure must be noted. From Table 11.1 and Table 7.1 in Chapter 7 it might seem that in spiral tomography the patients will be exposed to a higher dosage of X-rays. However this is not true. Recall that exposure was defined relative to the mode of acquisition. In spherical tomography the number of source positions is much higher leading to a higher dosage of X-rays for the patient. In spiral tomography the comparatively high value of exposure is due to the smaller number of

(a) Standard Reconstruction (b) Searchlight CT (c) Ground Truth

Figure 11.1: Comparison of reconstruction methods on a 3D Shepp-Logan phantom with representative 2D slices are shown (a) Standard Reconstruction (b) Searchlight CT (c) Ground Truth

Table 11.2: Performance of Searchlight CT with spiral tomography for various ROI-radii (Mouse Tissue Data)

ROI-radius	D	E	Rel	$PSNR$
45 voxels	4.0 %	21%	11.4 %	52.8 dB
60 voxels	9.9 %	33%	9.7 %	56.9 dB
75 voxels	20.7 %	47%	8.8 %	58.6 dB
90 voxels	29.8 %	60%	8.4 %	60.1 dB

source positions.

Similar experiments were carried out for the mouse tissue data. The performance is tabulated in Table 11.2 and a comparison of reconstruction methods is shown in Figure 11.2.

Finally we compare the performance of Searchlight CT for the spherical and spiral acquisition methods. A difference between the two methods is that while the spherical case took 40 iterations to converge, the spiral took 50.The performance for Shepp-Logan phantoms are tabulated in Table 7.1 for the spherical case and Table

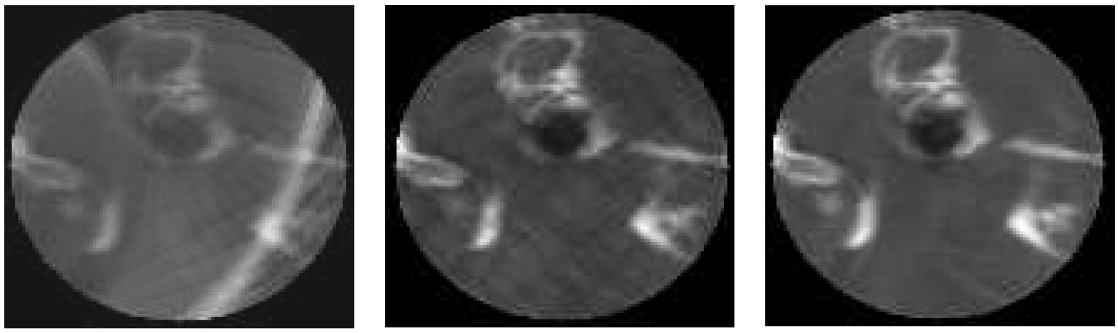

(a) Standard Reconstruction (b) Searchlight CT (c) Ground Truth

Figure 11.2: Comparison of reconstruction methods on the mouse tissue data with representative 2D slices are shown (a) Standard Reconstruction (b) Searchlight CT (c) Ground Truth

11.1 for the spiral case. The relative reconstruction error, as expected is slightly higher for the spiral case. For example when the radius of C is 60 pixels spherical acquisition has an error of 8.5% whereas the spiral acquisition had 9.1% error. For the mouse tissue data the corresponding errors are 8.8% for the spherical acquisition and 9.7% for the spiral acquisition. It must be noted that in the spiral case we have used a better technique of regularization so the difference seems smaller than it actually is.

11.3 Dependence of Searchlight CT on Parameters

As mentioned in the previous section, there are several parameters for spiral tomography. In this section we will observe the effect of these parameters on the quality of reconstruction when using Searchlight CT. We use the Shepp-Logan phantom and

for computational convenience we will keep the size of the phantom small at 64^3. The parameters used in the previous section are proportionally adjusted.

$$\begin{aligned}
\text{Size of Data} &= 64^3 \text{ voxels} \\
\text{Helical scanning radius} &= 96 \text{ voxels} \\
\text{Source Detector distance} &= 192 \text{ voxels} \\
\text{Helical Pitch} &= 9 \text{ voxels} \\
\text{Number of detector rows, } M &= 8 \\
\text{Sources per turn} &= 16M = 128
\end{aligned}$$

The Relative reconstruction error with 50 iterations *Rel* for this set of parameters is 10.7%. To study the effect of a particular parameter, we vary it while keeping the other parameters constant.

One important parameters is the number of detector rows, M, which in turn determines the number of sources per turn. Table 11.3 tabulates the relative error *Rel*, for various values of M. Number of row detector between 4 and 20 were considered.

Table 11.3: Relative Error, *Rel* for various number of detectors, M

Number of rows, M	4	8	12	16	20
Sources per Turn	64	128	192	256	320
Relative Error, Rel	15.3%	10.7%	9.8%	9.3%	8.6%

Obviously the higher the number of sources, the better will be the reconstruction. However we use just 8 detector rows (128 sources per turn) due to high computational

times. Searchlight CT requires the reconstruction of every slice and hence becomes computationally expensive if a higher number of detector rows is used. However if proper technology and resources are available, this parameter can be altered to improve performance. In the industrial applications typically 8 and 16 rows detectors are used while development of 32 and 32+ row detectors is in process [68].

Next we look at the effect of the pitch. As shown below, the pitch used in the previous section (which is 9 voxels for this smaller phantom) is the optimal pitch for best reconstruction. The performance of Searchlight CT for various helical pitches between 3 and 29 voxels is tabulated in Table 11.4.

Table 11.4: Relative Error, *Rel* for various values of helical pitches (in voxels)

Pitch	3	6	10	13	16	19	22	26	29
Rel	11.5%	11.0%	10.9%	16.7%	21.5%	20.7%	20.1%	20.6%	20.8%

As seen in Table 11.4 the optimal pitch is between 6 and 10 pixels. When the pitch is too small, the scanning tends to a 2D scan, hence the reconstruction accuracy is worse. On the other hand making the pitch too large leads to fewer source positions which negatively affects reconstruction. This implies that the performance doesn't have a direct correlation with the helical pitch which can further be seen in Figure 11.3. For the size of phantom we are considering, a realistic range of pitch would be between 7 and 13 voxels.

The effect of the helical scanning radius on the performance of Searchlight CT was found to be minimal. Though smaller radii lead to marginally better performance, medical reasons prevent it from being used in real life since a patient cannot

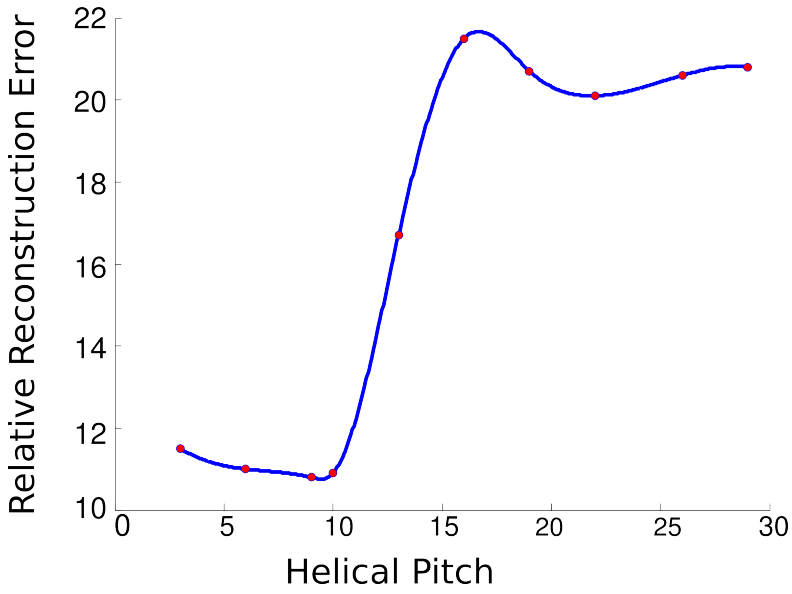

Figure 11.3: Plot of helical pitch against Relative Error for a Shepp-Logan phantom

be located too close to the emitting source. Table 11.5 shows the performance of Searchlight CT for various scanning radii between 64 and 160 voxels. The minimum distance by safety standards would be around 90 voxels.

Table 11.5: Relative Error, *Rel* for various values of helical scanning radii (in voxels)

Scanning Radius	64	80	96	112	128	144	160
Rel	10.2%	10.5%	10.7%	11.1%	11.3%	11.5%	11.6%

The last parameter is the source-detector distance. Usually this distance is greater than or equal to the helical scanning radius. Though greater distance leads to better performance, too high a distance may lead to loss of intensity in practice. For a phantom of size 64, the source-detector distance should not exceed 200 voxels. The performance for various source-detector distances is tabulated in Table 11.6.

We have examined the effect of the various parameters on the reconstruction

Table 11.6: Relative Error, *Rel* for various values of source-detector distance (in voxels)

Source-Detector Distance	96	128	160	192	224	256
Rel	12.0%	11.6%	11.1%	10.7%	10.7%	10.6%

accuracy. For the phantom of this size we have the inferred set of parameters for best reconstruction would be a large number of source positions, a pitch of about 9 voxels, a small scanning radius and a large source-detector distance. However there are realistic constraints of minimum scanning radius (of 90 voxels) and maximum source-detector distance (200 voxels). Hence we come to the conclusion that the set of parameters used initially is essentially optimal. The Searchlight CT algorithm is an effective algorithm for collimated reconstruction in case of spiral tomography.

CHAPTER 12

Related Research in Tomography

We have examined the problem of local reconstruction in Computed Tomography. Over the years there has been extensive research on the mathematics of tomography. *'The Mathematics of Computerized Tomography'* by Frank Natterer [65] was one of the first books to be published which dealt solely with this subject and is still considered to be 'Bible' for all in this area. *'Introduction to the Mathematics of Medical Imaging'* by Charles Epstein [22] covered a wider range of topics, it gave significant insight into the mathematics behind this real life problem. In this chapter we overview some of these attempts to study the underlying mathematical principles of tomography. The literature on 3D collimated reconstruction is very limited. Hence

we focus on the 2D collimated problem and the uncollimated 3D problem. For one particular attempt at the 2D collimated problem, comparison of results with Searchlight CT is provided. There are several research groups around the globe which are working in related areas. As per the chapters in this thesis we will classify the ongoing research into three categories: tomography in 2D, tomography in 3D and spiral tomography.

12.1 Computed Tomography in 2D

One of the well known algorithms for collimated reconstruction in 2D was proposed by Tim Olson and Joe Destefano first as a technical report in [71] and later on in [72, 70]. The algorithm suggested is briefly explained here. In its simplest form, all the rays passing through the region of interest C are allowed to pass while for the other rays, half of them are collimated. The missing values are approximated through interpolation in the wavelet transform. In a more general setting, the fraction of the other rays which are collimated increases as the distance from C increases. The X-ray Transform for the simple case is shown in Figure 12.1 and for the general case in Figure 12.2.

We compared the performance of Searchlight CT against to the one proposed in [71], using 2D Shepp-Logan phantoms. For this phantom, the Searchlight CT collimated reconstruction algorithm yields $Rel = 4.1\%$ while the algorithm proposed in [71] yields $Rel = 7.7\%$. However the major difference concerns the performance in terms of the exposure Ex. Using the method from [71], the radiation exposure

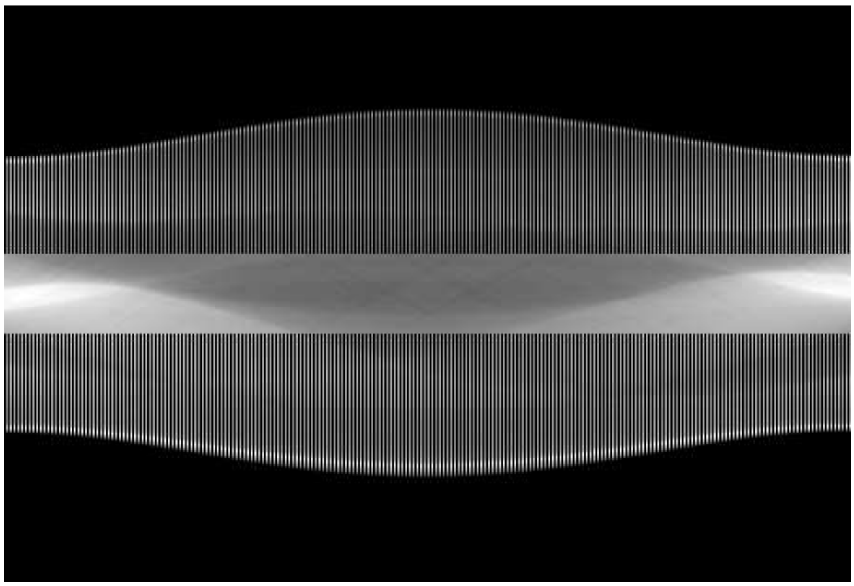

Figure 12.1: The X-ray Transform when half the rays not passing through the region C are collimated

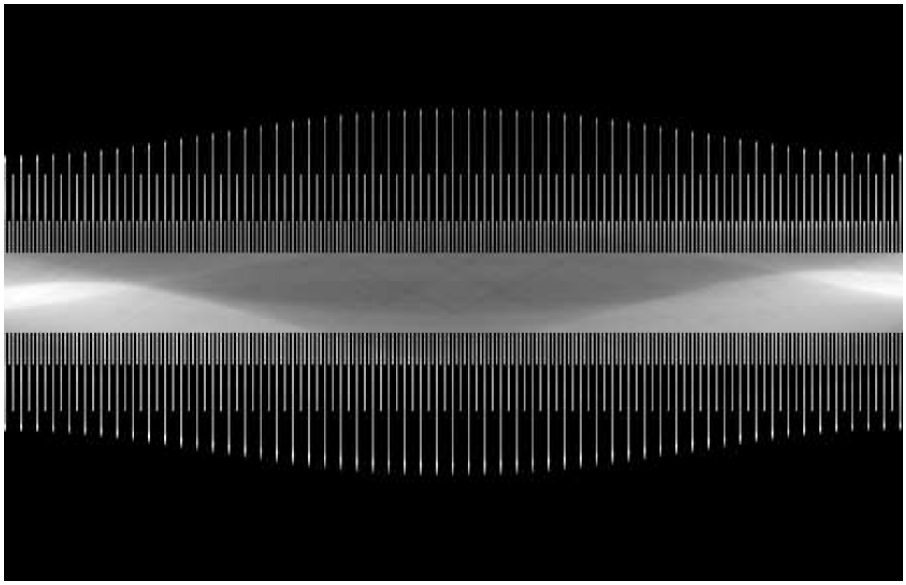

Figure 12.2: The X-ray Transform when a progressive fraction of the rays not passing through the region C are collimated

is 45%, while our Searchlight CT algorithm yields radiation exposure 27%, which is considerably smaller. Since our major objective was reducing exposure, the stated difference is very significant.

Another group which has recently worked on local tomography is led by Adel Faridani at the Oregon State University. Their approach to the problem is slightly different. Instead of reconstructing the density function F directly, they reconstruct a related function. In [24], Faridani et al. reconstructed ΛF where Λ is the square root of the positive Laplace operator, $-\Delta$. This function ΛF has the same boundaries and smooth regions as F. However, in the regions where F is constant, ΛF has a cupped shape. This cupping can partially be neutralized by the addition of the operator $\mu\Lambda^{-1}$. Hence in the sequel paper [23] the function to be reconstructed locally was chosen to be $\alpha(\Lambda + \mu\Lambda^{-1})F$.

A similar method called *pseudo-local tomography* was explored by Katsevich and Ramm in [49]. Rather than reconstructing F directly, an auxiliary function F_d with local reconstruction properties was reconstructed. This function preserves the location and sizes of the discontinuities of F as well as its derivative. In a previous paper [48] the authors had discusses the general problem of finding the discontinuities of a function from its tomographic data. However the major contribution of Katsevich was in the development of exact inversion formulae for spiral tomography.

In [7] Walnut et al. have used the theory of continuous wavelet transforms to derive the reconstruction formula for the Radon Transform. However the major disadvantage here is that it is applicable only in even dimensions, where the reconstruction formulae turn out to be local. Hence the formulae are not applicable in the

realistic 3D setting. The method suggested in [78] suffers from the same shortcomings though it performs well in terms of exposure.

Recently this problem has been tackled by Zeng et al. at University of Utah. An algorithm using the maximum likelihood expectation method was proposed is [103]. Another approach was presented in [102] specifically for convex regions of interest.

Some other results on 2D collimated tomography include [84, 97, 74, 47]. As stated above, most of these focus on extracting the singular component (edges) through a related function or can be applied only in even dimensions. Even in such cases, the performance is not fully satisfactory.

12.2 Computed Tomography in 3D

We have used spherical acquisition as an initial mode of acquisition in 3D. This mode of acquisition is highly redundant on source positions and can be restricted to curves in 3D. Early studies considered source positions on a circular trajectory, with conical-beam X-rays emitting from them. This case is very close to the 2D acquisition. Even presently this technique is used at certain medical research centers, for example at the Methodist Hospital, Houston. Part of the data for this research was provided by them, and it was scanned on a machine as shown in Figure 12.3.

One of the earliest and most famous reconstruction method was devised by Feldkamp, Davis, and Kress in [25] and named after them as FDK. This method assumes circular acquisition and ignores the divergence of beams. The FDK algorithm has

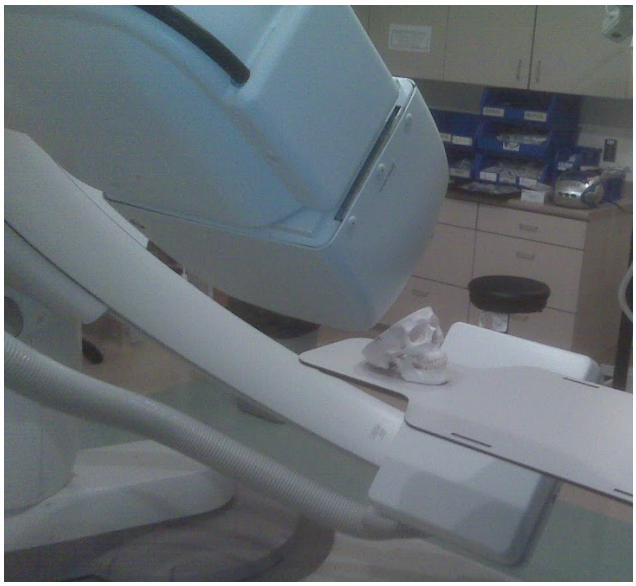

Figure 12.3: A CT scan machine with the source positions on a circular path (at Methodist Hospital, Houston)

several variants for modern applications. Its application to spiral CT will be seen in the next section. Reconstruction from circular acquisition is also discussed in [58, 93, 11]. Finch extended circular acquisition to general planar curves in [26]. Despite the simplicity of its nature, the major disadvantage here is the limited number of source positions.

As a next step, to increase the number of source positions, Zhuang et al. suggested an acquisition technique in [105] which had two concentric circles lying on orthogonal planes. A similar technique was described in [13]. Katsevich generalized this algorithm where it was enough to use incomplete circles [46]. Finally instead of using a circle or circles (which lie on a finite number of planes), a new approach suggested acquisition on a saddle trajectory. This is examined and validated in [73, 9].

In an effort to generalize the 3D reconstruction, attempts were made to adapt the acquisition for any bounded curve. Initially these attempts were purely theoretical. One successful approach was given by Tuy in [94]. This was extended by Grangeat in [31]. Finch gave another approach to this problem in [28]. Recently a team led by Ge Wang has made further progress in this direction [104, 99].

Most of the attempts at 3D reconstruction study the uncollimated case. Hence health hazards due to high radiation dose still remained a problem. A review of developments on the collimated X-ray Transform is given in [27]. Due to its non-locality there were efforts to reduce the dosage by sparsifying the source positions [101, 35]. However the fewer the source positions the less accurate is the reconstruction.

Another possible approach is to use compressed sensing [12, 4] to avoid high radiation dose. Recall that compressed sensing exploits the fact that many types of data can be represented using only a few terms in a suitable representation. Hence, nonlinear optimization methods such as ℓ_1 minimization can be employed to recover such data using very few measurements. However, such measurements have to be highly decorrelated with respect to the data and this implies that the radiations sources have to be placed at specific locations, typically on a highly irregular grid. As a result, the application of this type of approach requires to radically redesign the acquisition process in CT devices.

A very recent development which used circular acquisition (C-arm tomography) is the ATRACT algorithm. This algorithm is amongst the first designed for 3D collimated X-ray tomography. It was developed by Dennerlein and results are presented for angiographic data in [18].

12.3 Spiral Tomography

Initial attempts at reconstruction from spiral tomographic data ignored the divergence of the X-ray beams as only four detector rows were used. Such reconstruction algorithms were explored in [87, 80]. However machines with higher number of detector rows soon appeared in the market. CT scanners with 16 detector rows were introduced in 2001. So the divergence could no longer be neglected and new algorithms were introduced keeping this in account. Spiral tomography reconstruction algorithms can be divided into two categories, exact and approximate which has three further subcategories, a brief description of which are given below following [68, 44].

1. Approximate Algorithms
   (a) Rebinning Algorithms
   (b) FDK-like Algorithms
   (c) Quasi-exact Algorithms
2. Theoretically Exact Algorithms

The rebinning algorithms estimate the 2D X-ray Transforms on oblique slices. The oblique slices can then be computed by any 2D reconstruction technique. The reconstruction is completed by interpolating between these oblique slices. The quality of reconstruction depends mainly on the initial estimate of the 2D X-ray Transforms. There are several algorithms to estimate the 2D X-ray Transforms, for example the

oblique surface reconstruction algorithm [37, 14], the nutating slice algorithm [55], the ASSR method [40], etc. An exact formula was given in [81] but is computationally very expensive.

As mentioned previously, in 1984 Feldkamp, Davis, and Kress (FDK) designed an algorithm for reconstruction from circular scans [25]. These were later extended for application to spiral tomography. The algorithm had three major steps: 1D ramp filtering, data weighting and cone beam back-projection. The data weighting is introduced to smooth out the discontinuities in the reconstruction of a slice. One of the first adaptations to spiral CT was made in [15]. As in the original FDK algorithm in [25], this paper too ignored the divergence of beams. This was countered with time and good algorithms for a large number of detector rows were introduced in [93, 85]. The major drawback of FDK-like algorithms it that it fails to predict the presence of artifacts in the reconstruction. This is primarily due to the lack of theoretical support for the approximations involved in the algorithm.

The analytical formulae for reconstruction can be discretized for applications. This constitutes the quasi-exact class of reconstruction formulae. A majority of these are developed from Grangeat's theory for cone-beam reconstruction using the 3D Radon Transform. These methods are not exact because some of the Radon samples are processed incorrectly. More details regarding this can be found in [89]. Some of the major quasi-exact algorithms are the zero boundary method [17], the virtual circle method [53] and the local-ROI method using Hilbert filtering [88]. The quasi-exact algorithms are less computationally efficient than the rebining and FDK algorithms and may suffer from discretization errors.

We have already mentioned an exact reconstruction method in [81] in the description of rebining algorithms. A filtered back-projection formulation of this was given in [56]. A four step local-ROI method was described in[88]. Exact reconstructions can also be achieved by adding a correction image to quasi-exact algorithms [89]. Another class of exact reconstruction methods use the relationship between the first derivative of the Radon Transform and the cone-beam transform [31, 75, 64].

The major difference between exact and approximate methods is that while exact methods are more accurate they are computationally very intensive and require a huge amount of memory to store the cone-beam projections. This gap was bridged by Katsevich, who provided a first theoretically exact inversion formula using the filtered back-projection [41, 43] (after deriving an approximate formula in[42]). The formula was later implemented in an efficient way. The major advantage of the Katsevich inversion formula is that it is proved in the most general setting and is independent of acquisition method. As described in Chapter 10, the formula has two steps, filtering of the derivative followed by back-projection. The drawbacks however is the requirement of a detector array larger than the theoretically minimum and the support of the object being smaller than the realistic case of a patient.

These drawbacks were addressed by Katsevich himself in [45] where he proposed an improved version of the algorithm. In this variant there was no longer a restriction on the support of the object and the detector array is much smaller than the previous one. As an added advantage this algorithm is twice as fast. Further analysis of this formula is given in [44]. It was shown for a phantom constant along the z-direction, the formula was equivalent to the 2D inversion of the X-ray Transform. The formula

remained exact as the helical pitch tended to zero and the limit was again the 2D X-ray inversion.

The Katsevich inversion formula was tested initially on simulated phantoms in [45]. There have been several attempts on better implementation of this formula. One of these was discussed in detail in Chapter 10 which was based on [68]. A different approach is given in [100].

CHAPTER 13

Conclusion and Future Research

Over the course of the thesis, we have presented an algorithm which can reconstruct a small region within the support of an objective function, F from the X-ray Transform of F. This is especially useful for cases which require several follow up scans, for example scans to monitor the progress of a tumor. If only a specific region of interest C needs to be monitored, Searchlight CT can be used to reconstruct this region. This method greatly reduces the radiation exposure of a patient to harmful X-rays.

Another advantage of the Searchlight CT algorithm is that it requires minimal alteration to acquisition devices. Though we have described various variants of collimation the simplest one involving strict cutoffs was seen to be good enough for the

convergence of the algorithm. This mode of collimation is the simplest to manufacture in the industry. We have consulted doctors and technicians at the Methodist Hospital, Houston, who have confirmed the viability of such collimators which are made of aluminum.

However the current algorithm needs several improvements to be useful in practical situations.

13.1 Current Enhancements of Searchlight CT

Elimination of Redundancies

The acquisition and inversion techniques have redundancies. Removing these redundancies is beneficial in more than one way. Our original objective was to reduce radiation exposure. Reduction of redundancies will go a long way in reducing radiation exposure during the initial scan. Also this will lead to a major improvement in computational efficiency.

Computational Efficiency

The programs written for Searchlight CT have not been coded by professional programmers. By implementing better programming techniques like parallel computing, we can significantly improve the computing time. Parallel computing requires extensive computing resources and additional licenses. Hence availability might be an

issue. However it might be very useful especially in the implementation of the Katsevich inversion formula. Here each slice is reconstructed individually so parallel cores would speed up algorithm.

Rigorous Analytical Proof

No mathematical algorithm is complete without an analytical proof. Presently we have provided a detailed validation through eigenvalues and eigenvectors. We have also provided an outline for the analytical proof in which we intend to relax the assumptions of starting with a regularized objective function and regularizing the replacement operator. An analytical proof in the most general setting is one of our present targets.

Dependence on Parameters

Currently our algorithm is very dependent on parameters. Sometimes parameters may not be exact. Minor variations in parameters lead to significant changes in performance. We consider the following example to emphasize this problem.

We were provided collimated X-ray data from the Methodist Hospital to test our algorithm. The 3D acquisition was on a circle. A 2D section of the data was chosen to apply our version of the 2D algorithm. The data were incomplete and needed to be completed by the method in Section 2.2. Data were available for projection angles between 70 and 290 as shown in Figure 13.1.

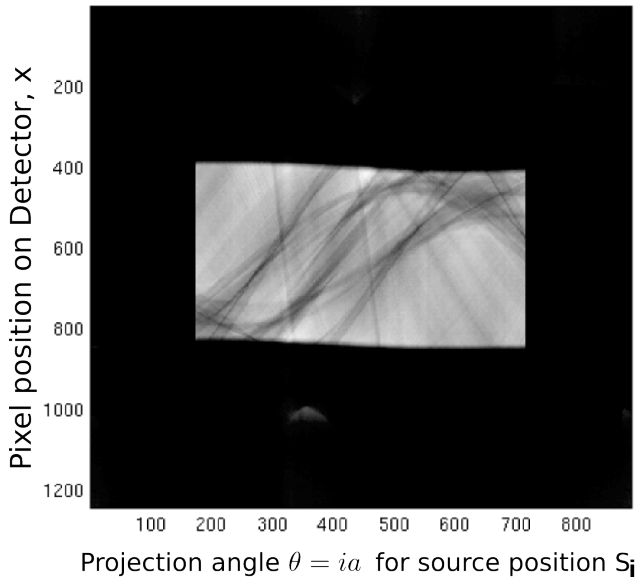

Figure 13.1: Incomplete X-ray data as provided by Methodist Hospital

The data were then completed using Section 2.2. However the parameters provided to us were inaccurate and hence the completion was not exact, as seen in Figure 13.2. This made this data set unusable for Searchlight CT.

In view of such situations (which sometimes cannot be avoided as will be seen in the next section) we need to modify the Searchlight CT algorithm so that it can handle approximate parameters.

13.2 Future Research

The major long term goal is to make Searchlight CT a medically viable technique which can be used on human patients. To get to that stage we need to address several sources of errors. We have already seen the problems caused by the over

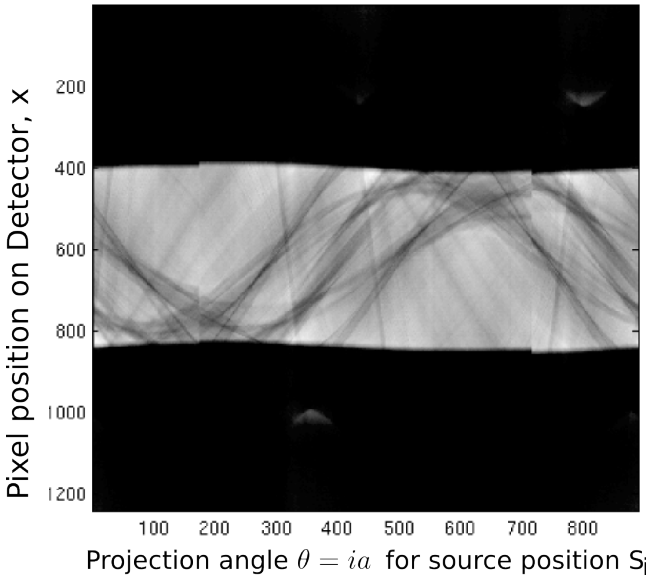

Figure 13.2: Completed X-ray data from Figure 13.1

dependence on parameters. Practically parameters like distances and sizes will only be approximate. Some other factors are mentioned below.

Naturally Occurring Noise

Though we have checked for robustness to Gaussian noise most of the noise that occur naturally is not of this kind. Noise may occur in many other ways which may not be suitable for Searchlight CT. We have interacted with doctors at the Methodist Hospital who have enlightened us on some of the ways noise may occur. The source and detectors are not fully stable during rotation which causes noisy data acquisition. Slight malfunctions in acquisition devices can also cause noisy acquisition.

Fixed Density Function

We have assumed the density function to be fixed. This might not always be the case. Due to internal or external movements of a patient the function might change with time. A classic example of this is the beating of a heart. This will complicate the reconstruction process. Searchlight CT needs to be improved to handle such cases. Also when the density function changes with time the parameters may also change. This makes the problem of handling approximate parameters all the more important. There have been some initial attempts in this direction, which is now called 4D CT. A team [29] has been working on 4D CT in relation to blood and air flow in the lungs.

Industrial Partnership

We have a very good understanding of the mathematical models and algorithmics required for Searchlight CT. However viability of acquisition and collimation techniques in real life is something which can best be explained by industrial scientists and technicians. To make Searchlight CT applicable on human patients we aim to tie up with an industrial partner.

An industrial input on Searchlight CT can go a long way in overcoming the obstacles currently faced. With a better understanding of the acquisition devices we can create more suitable mathematical models. Quantities like Radiation Exposure and Relative Density will be defined slightly differently to ensure that the practical situation is properly modeled. For example, an X-ray beam not only affects a single

point through which it passes but also a small neighborhood around it.

We have seen the good performance of Searchlight CT for the simulations we have tried with both simulated and real data. We expect that with proper development this can become a medically viable diagnostic tool.

Bibliography

[1] C. Albert, J.R. Moore, and S.D. Glaser. Wavelet denoising techniques with applications to experimental geophysical data. *Signal Processing*, 89(2):144–160, 2009.

[2] A. Averbuch and Y. Shkolnisky. 3D Fourier-based discrete Radon transform. *Applied and Computational Harmonic Analysis*, 15:33–69, 2003.

[3] A. Averbuch and Y. Shkolnisky. 3D discrete X-Ray transform. *Applied and Computational Harmonic Analysis*, 17:259–276, 2004.

[4] N.S. Aybat and A. Chakraborty. Reconstruction of CT images from parsimonious angular measurements via compressed sensing. Technical report, 2009.

[5] R. Azencott, B. Bodmann, D. Labate, A. Sen, K. Li, and X. Zhou. Searchlight CT: A new reconstruction method for collimated X-ray tomography. *Proceedings NCMIP*, 2011.

[6] M.A. Bean. *Probability: The Science of Uncertainty with Applications to Investments, Insurance and Engineering*. American Mathematical Society, 2001.

[7] C. Berenstein and D. Walnut. Local inversion of the Radon transform in even dimensions using wavelets. In P. Michor and S. Gindikin, editors, *In 75 Years of Radon Transform*, pages 45–69. International Press, 1992.

[8] D. Bharkhada, H.Y. Yu, R. Dixon, Y.C. Wei, J.J. Carr, D. Bourland, R. Hogan, and G. Wang. Demonstration of dose and scatter reduction for interior tomography. *Computer Assisted Tomography*, 33(6):967–72, 2009.

[9] C. Bontus, R. Proksa, and T. Kohler. New saddle trajectories for CT. *Nuclear Science Symposium Conference Record, IEEE*, 49:2309–2310, 2006.

[10] D. Brenner and E. J. Hall. Computed tomography. an increasing source of radiation exposure. *The New England Journal of Medicine*, 357:2277–2284, 1997.

[11] A.V. Bronnikov. Cone-beam reconstruction by back-projection and filtering. *Optical Society of America A*, 17(11):1993–2000, 2000.

[12] G. H. Chen, J. Tang, and S. Leng. Prior image constrained compressed sensing (piccs): a method to accurately reconstruct dynamic CT images from highly undersampled projection data sets. *Medical Physics*, 35(2):660–663, 2008.

[13] G.H. Chen, C.A. Mistretta, H. Rowley, and M. Van Lysel. X-ray system for use in image guided procedures, 2005.

[14] L. Chen, D.J. Heuscher, and Y. Liang. Oblique surface reconstruction to approximate cone beam spiral data in multiscale CT. *Proceedings SPIE*, 4123:204–207, 2000.

[15] C.R. Crawford and K.F. King. Computed tomography scanning with simultaneous patient translation. *Medical Physics*, 17(6):967–982, 1990.

[16] P.E. Danielsson, P. Edholm, J. Eriksson, and S.M. Magnusson. Towards exact reconstruction for helical cone-beam scanning of long objects. a new detedtor arrangement and a new completeness condition. In D.W. Townsend and P.E. Kinahan, editors, *Proceedings 1997 Meeting on Fully 3D Image Reconstruction in Radiology and Nuclear Medicine*, pages 141–144, 1997.

[17] M. Defrise, F. Noo, and H. Kudo. A solution to the long object problem in helical cone-beam tomography. *Physics in Medicine and Biology*, 45:623–643, 2000.

[18] F. Dennerlein and A. Maier. Region of interest reconstruction on medical c-arms with ATRACT algorithm. In N. J. Pelc, R. M. Nishikawa, and R. Whiting, editors, *Medical Imaging 2012: Physics of Medical Imaging*, 2012.

[19] D.L. Donoho. Denoising by soft-thresholding. *IEEE Ttranscations on Information Theory*, 41(3):613–627, 1995.

[20] G. R. Easley, F. Colonna, K. Guo, and D. Labate. Radon transform inversion using shearlet representation. *International Journal of Magnetic Resonance Imaging*, 29:232–250, 2010.

[21] G. R. Easley, F. Colonna, and D. Labate. Improved Radon bases imaging using the shearlet transform. *Procedings SPIE, Defense Security and Sensing*, 2009.

[22] C. Epstein. *Introduction to the Mathematics of Medical Imaging, Second Edition*. SIAM: Society for Industrial and Applied Mathematics, 2007.

[23] A. Faridani, D.V. Finch, E.L. Ritman, and K.T. Smith. Local tomography II. *SIAM Journal of Applied Mathematics*, 57(4):1095–1127, 1997.

[24] A. Faridani, E.L. Ritman, and K.T. Smith. Local tomography. *SIAM Journal of Applied Mathematics*, 51:459–484, 1193–1198, 1992.

[25] L. Feldkamp, L.C. Davis, and J.W. Kress. Practical cone-beam algorithm. *Journal of Optical Society of America A*, 1(6):612–619, 1984.

[26] D.V. Finch. Approximate reconstruction formulae for the cone beam transform I. 1987.

[27] D.V. Finch. The attenuated X-ray transform: recent developements. In G. Uhlmann, editor, *Inside Out: Inverse Problems and Applications*, pages 47–66. Cambridge University Press, 2003.

[28] D.V. Finch, I.R. Lan, and G. Uhlmann. Microlocal analysis of the X-ray transform with sources on a curve. In G. Uhlmann, editor, *Inside Out: Inverse Problems and Applications*, pages 193–218. Cambridge University Press, 2003.

[29] R. Fowler, J. Warren, Y. Zhang, T. Guerrero, and B. Broom. Processing 4D CT scans of the lungs. Proposal submitted to 2005 GC4R program for Collaborative Advances in Biomedical Computing (C-ABC).

[30] L. Gagnon and F.D. Smaili. Speckle noise reduction of airborne SAR images with symmetric Daubechies wavelets. *Proceedings SPIE*, 2759:14–24, 1996.

[31] P. Grangeat. Mathematical framework of cone-beam 3d reconstruction via the first derevative of the Radon transform. In G.T. Herman, M.K. Lewis, and F. Natterer, editors, *Mathematical methods in tomography (Lecture Notes in Mathematics vol 1497)*, pages 66–97. Springer, Berlin, 1991.

[32] H. Guo, J.E. Odegard, M. Lang, R.A. Gopinath, I.W. Selesnick, and C.S. Burrus. Wavelet based speckle reduction with application to SAR based ATD/R. *First International Conference on image processing*, 1:75–79, 1994.

[33] J. Hadamard. Sur les problèmes aux dérivés partielles et leur signification physique. *Princeton University Bulletin*, 1:49–52, 1902.

[34] R.C. Hardie and C.G. Boncelet. Gradient-based edge detection using nonlinear edge enhancing prefilters. *IEEE Transcations on Medical Imaging*, 4(11):1572–1577, 1995.

[35] G. T. Herman and R Davidi. Image reconstruction from a small number of projections. *Inverse Problems*, 24(4), 2008.

[36] C. Herzog, P. L. Zwerner, J. R. Doll, C.D. Nielsen, S.A. Nguyen, G. Savino, T.J. Vogl, P. Costello, and U.J. Schoepf. Significant coronary artery stenosis: comparison on per-patient and per-vessel or per-segment basis at 64-section CT angiography. *Radiology*, 244(1):112–120, 2007.

[37] D.J. Heuscher. Spiral cone beam scans using 2d surface reconstructions. *International Meeting on Fully 3D Image Reconstruction*, pages 204–207, 1999.

[38] S. Holm, P. Toft, and M. Jensen. Estimation of the noise contributions from blank, transmission and emission scans in PET. *IEEE Transactions on Nuclear Science*, 43(4):2285–2291, 1996.

[39] W. Huda, W. Randazzo, S. Tipnis, G.D. Frey, and E. Mah. Embryo dose estimates in body CT. *American Journal of Roentgenology*, 194(4):874–880, 2010.

[40] M. Kachelriess, S. Schaller, and W.A. Kalender. Advanced single-slice rebining in cone-beam spiral CT. *Medical Physics*, 27:754–772, 2000.

[41] A.I. Katsevich. An inversion algorithm for spiral CT. In A.I. Zayed, editor, *International Conference on Sampling Theory and Applications*, pages 261–265, 2001.

[42] A.I. Katsevich. Microlocal analysis of FBP algorithm for trucated spiral cone-beam data. *Journal of Fourier Analysis and Applications*, 8(5):407–425, 2002.

[43] A.I. Katsevich. Theoretically exact FBP-type inversion algorithm for spiral CT. *SIAM Journal of Applied Mathematics*, 62:2012–2026, 2002.

[44] A.I. Katsevich. Analysis of an exact inversion algorithm for spiral cone-beam CT. *Physics in Medicine and Biology*, 32:681–697, 2003.

[45] A.I. Katsevich. An improved filtered back-projection algorithm for spiral computed tomography. *Advances in Applied Mathematics*, 32:681–697, 2003.

[46] A.I. Katsevich. Image reconstruction for the circle-and-arc trajectory. *Physics in Medicine and Biology*, 50:2249–2265, 2005.

[47] A.I. Katsevich. Improved cone beam local tomography. *Inverse Problems*, 22:627–643, 2006.

[48] A.I. Katsevich and A.G. Ramm. A method for finding discontinuities from the tomographic data. In M. Cheney, P. Kuchment, and E.T. Quinto, editors, *1993 AMS-SIAM Summer Seminar on the mathematics of tomography, impedance imaging and integral geometry*, 1994.

[49] A.I. Katsevich and A.G. Ramm. Pseudolocal tomography. *SIAM Journal of Applied Mathematics*, 56(1):167–191, 1996.

[50] N.C. Kingsbury. Image processing with complex wavelets. *Philosophical Transactions of the Royal Society, London*, 1999.

[51] N.C. Kingsbury. Complex wavelets for shift invariant analysis and filtering of signals. *Applied and Computational Harmonic Analysis*, 10(3):234 – 253, 2001.

[52] I. Krzysztof. *Medical Imaging: Principles, Detectors, and Electronics*. Wiley-Interscience, 2009.

[53] H. Kudo, M. Defrise, and F. Noo. Quasi-exact filtered back-projection algorithm for ong object problem in helical cone-beam tomography. *IEEE Transactions on Medical Imaging*, 19:902–921, 2000.

[54] J. L. Lancaster. Physics of Medical X-Ray Imaging. Course Notes, Research Imaging Center, UTHSCSA, 2011.

[55] G.L. Larsson, C.C. Ruth, and C.R. Crawford. Nutating slice CT image reconstruction: apparatus and method, 1998.

[56] G. Lauritsch, K.C. Tam, K. Sourbelle, and S. Schaller. Exact local region of interest reconstruction in spiral cone-beam filtered back-projection CT: numerical implementation and first image results. *Proceedings SPIE*, 3079:91–94, 2000.

[57] C. I. Lee, A. H. Haims, E. P. Monico, J.A. Brink, and H.P. Forman. Diagnostic CT scans: assessment of patient, physician, and radiologist awareness of radiation dose and possible risks. *Radiology*, 231(2):393–398, 2004.

[58] A.K. Lewis, T. Weber, and D. Theis. Computing reconstruction kernels for circular 3D cone beam tomography. *IEEE Transactions on Medical Imaging*, 27(7):880–886, 2008.

[59] J.M. Lina. Image processing with complex Daubechies wavelets. *Journal Mathamatical Imaging and Vision*, 7(3):211–223, 1997.

[60] J.M. Lina and L. Gagnon. Image enhancement with symmetric Daubechies wavelets. *Wavelet Applications in Signal Processing III, Procedings SPIE*, pages 196–207, 1995.

[61] S. Mallat. *A Wavelet Tour of Signal Processing*. Academy Press, 1998.

[62] C.E. Metz and R.N. Beck. Quantitative effects of stationary linear image processing on noise and resolution of structure in radio-nuclide images. *Journal of Nuclear Medicine*, 15(3):164–170, 1974.

[63] J.M. Miller, M. Dewey, A.L. Vavere, C.E. Rochitte, H. Niinuma, A. Arbab-Zadeh, N. Paul, J. Hoe, A. de Roos, K. Yoshioka, P.A. Lemos, D.E. Bush, A.C. Lardo, J. Texter, J. Brinker, C. Cox, M.E. Clouse, and J.A. Lima. Coronary CT angiography using 64 detector rows: methods and design of the multi-centre trial core-64. *European Radiology*, 19(4):816–828, 2009.

[64] F. Natterer. Recent developements in X-ray tomography. *Lectures in Applied Mathematics*, 30:177–198, 1994.

[65] F. Natterer. *The Mathematics of Computerized Tomography*. SIAM: Society for Industrial and Applied Mathematics, 2001.

[66] F. Natterer and F. Wubbeling. *Mathematical Methods in Image Reconstruction*. SIAM: Society for Industrial and Applied Mathematics, 2001.

[67] M.N. Nobi and M.A. Yousuf. A new method to remove noise in magnetic resonance and ultrasound images. *Journal of Scientific Research*, 3(1):81–89, 2011.

[68] F. Noo, J. Peck, and D. Heuscher. Exact helical reconstruction using native cone-beam geometries. *Physics in Medicine and Biology*, 48:3787–3818, 2003.

[69] J. Ojanen and J. Heikkonen. MDL and wavelet denoising with soft thresholding. In *Proceedings of the 1st Workshop on Information Theoretic Methods in Science and Engineering*, pages 1–6. Tampere International Center for Signal Processing, 2008.

[70] T. Olson and J. Destefano. Wavelet localization of Radon transform in even dimension. *Procedings IEEE International Symposium on Time-frequency and Time-scale Analysis*, pages 219–222, 1992.

[71] T. Olson and J. Destefano. Wavelet localization of the Radon transform. Technical Report PCS-TR93-196, Dartmouth College, Computer Science, Hanover, NH, 1993.

[72] T. Olson and J. Destefano. Wavelet localization of Radon transform. *IEEE Transactions on Signal Processing*, 42(8):2055–2067, 1994.

[73] J.D. Pack, F. Noo, and H. Kudo. Investigation of saddle trajectories for cardiac CT imaging in cone-beam geometry. *Physics in Medicine and Biology*, 49:2317–2336, 2004.

[74] E.T. Quinto. Singularities of the X-ray transform and limited data tomography in R^2. *SIAM Journal of Mathematical Analysis*, 24:1215–1225, 1993.

[75] A.G. Ramm and A.I. Zaslavsky. Inversion of incomplete cone-beam data. *Applied Mathematics Letters*, 5:91–94, 1992.

[76] M. V. Gopala Rao, E. M. L. Tanuja, and S. Vathsal. Wavelet-based local tomography. *Proceedings National Seminar on Non Destructive Evaluation*, 2006.

[77] M.V.G. Rao and S. Vathsal. Regularized computed tomography using complex wavelets. *AIP Conference Procedings*, 1050:194–204, 2007.

[78] F. Rashid Farrokhi, K.J. Ray Liu, C. Berenstein, and D. Walnut. Wavelet-based multiresolution local tomography. *IEEE Transactions on Image Processing*, 6(10):1412–1429, 1997.

[79] P. Razifar, M. Sandstrom, H. Schnieder, B. Langstrom, E. Maripuu, E. Bengtsson, and M. Bergstrom. Quantitative effects of stationary linear image processing on noise and resolution of structure in radio-nuclide images. *BioMed Central, Medical Imaging*, 5(5), 2005.

[80] S. Schaller, T. Flohr, K. Klingenbeck, T. Fuchs, K. Kraus, and W.A. Kalender. Algorithm for image reconstruction in multi-scale helical CT. *IEEE Transcations on Medical Imaging*, 19(9):822–834, 2000.

[81] S. Schaller, F. Noo, K.C. Tam, G. Lauritsch, and T. Flohr. Exact Radon rebining algorithm for the long object problem in helical cone beam CT. *IEEE Transcations on Medical Imaging*, 19(5):361–375, 2000.

[82] I.W. Selesnick, R.G. Baraniuk, and N.C. Kingsbury. The dual-tree complex wavelet transform. *Signal Processing Magazine, IEEE*, 22(6):123–151, 2005.

[83] J. Sijbers, A.J. den Dekker, J. Van Audekerke, M. Verhoye, and D. Van Dyck. Estimation of the noise in magnitude MR images. *Magnetic Resonance Imaging*, 16(1):87–90, 1998.

[84] R. Smith-Bindman, J. Lipson, R. Marcus, K. Kim, M. Mahesh, R. Gould, A. B. de Gonzlez, and D. Miglioretti. Radiation dose associated with common computed tomography examinations and the associated lifetime attributable risk of cancer. *Archives of Internal Medicine*, 169(22):2078–2086, 2009.

[85] K. Sourbelle. *Performance Evaluation of Exact and Approximate Cone-beam Algorithms in Spiral Computed Tomography*. PhD thesis, Erlangen University, Germany, 2002.

[86] W. Su and R.K. Ward. An edge-based image interpolation approach using symmetric biorthogonal wavelet transform. *Multimedia Signal Processing, 2006 IEEE 8th Workshop*, pages 355–359, 2006.

[87] K. Taguchi and H. Aradate. Algorithm for image reconstruction in multi-scale helical CT. *Medical Physics*, 25(4):550–561, 1998.

[88] K.C. Tam. Exact local region-of-interest reconstruction in spiral cone-beam filtered back-projection CT. *Proceedings SPIE*, 3979:506–519, 2000.

[89] K.C. Tam, G. Lauritsch, and K. Sourbelle. Filtering point spread function in back-projection cone-beam CT and its application in long object imaging. *Physics in Medicine and Biology*, 47:2685–2703, 2002.

[90] V. Thavavel and R. Murugesan. Regularized computed tomography using complex wavelets. *International Journal of Magnetic Resonance Imaging*, 1(1):27–32, 2007.

[91] V. Thavavel, R. Murugesan, and M. Sundaram. Dual tree complex wavelet regularized deconvolution in computed tomography. *GVIP Journal*, 7(1):1–5, 2007.

[92] B.M.W. Tsui. *Effects of the Recorder System on Spatial Resolution and Noise in the Nuclear Medicine*. PhD thesis, University of Chicago, USA, 1977.

[93] H. Turbell. *Three Dimensional Image Reconstruction in Circular and Helical Computed Tomography*. PhD thesis, Linkoping University, Sweeden, 1999.

[94] H.K. Tuy. An inversion formula for cone-beam reconstruction. *SIAM Journal of Applied Mathematics*, 43(3):546–552, 1983.

[95] S.E. Umbaugh. *Computer Imaging: Digital Image Analysis and Processing*. CRC Press, 2005.

[96] A. Wunderlich. *The Katsevich Inversion Formula for Cone-beam Computed Tomography*. Master's thesis, Oregon State University, 2006.

[97] J.S. Yang, H.Y. Yu, M. Jiang, and G. Wang. High-order total variation minimization for interior tomography. *Inverse Problems*, 26:1–29, 2010.

[98] J.S. Yang, H.Y. Yu, M. Jiang, and G. Wang. High-order total variation minimization for interior tomography. *Inverse Problems*, 26:1–29, 2010.

[99] Y. Ye and G. Wang. Filtered back-projection formula for exact image reconstruction from cone-beam data along a general scanning curve. *Medical Physics*, 32:42–48, 2005.

[100] H. Yu and G. Wang. Studies on implementation of Katsevich algorithm for spiral cone beam CT. *Journal of X-Ray Science and Technology*, 12(2/2004):97–116, 2004.

[101] H. Yu and G. Wang. SART-type image reconstruction from a limited number of projections with the sparsity constraint. *International Journal of Biomedical Imaging*, 10, 2010.

[102] G.L. Zeng and G.T. Gullberg. Exact iterative reconstruction for interior problem. *Physics of Medical Biology*, 54(19):5805–5814, 2009.

[103] B. Zhang and G.L. Zeng. Two dimensional iterative region of iterest reconstruction from truncated projection data. *Medical Physics*, 34(3):935–944, 2007.

[104] S. Zhao, H. Yu, and G. Wang. A unified framework for exact cone-beam reconstruction formulas. *Medical Physics*, 32(6):1712–1721, 2005.

[105] T. Zhuang, B.E. Nett, S.I. Leng, and G. Chen. A shift-invariant filtered back-projection (FBP) cone-beam reconstruction algorithm for the source trajectory of two concentric circles using an equal weighting scheme. *Physics in Medicine and Biology*, 51:3189–3210, 2006.